Characterizing Noise and Expanding Calibration of Current Transformers for High-Frequency Applications
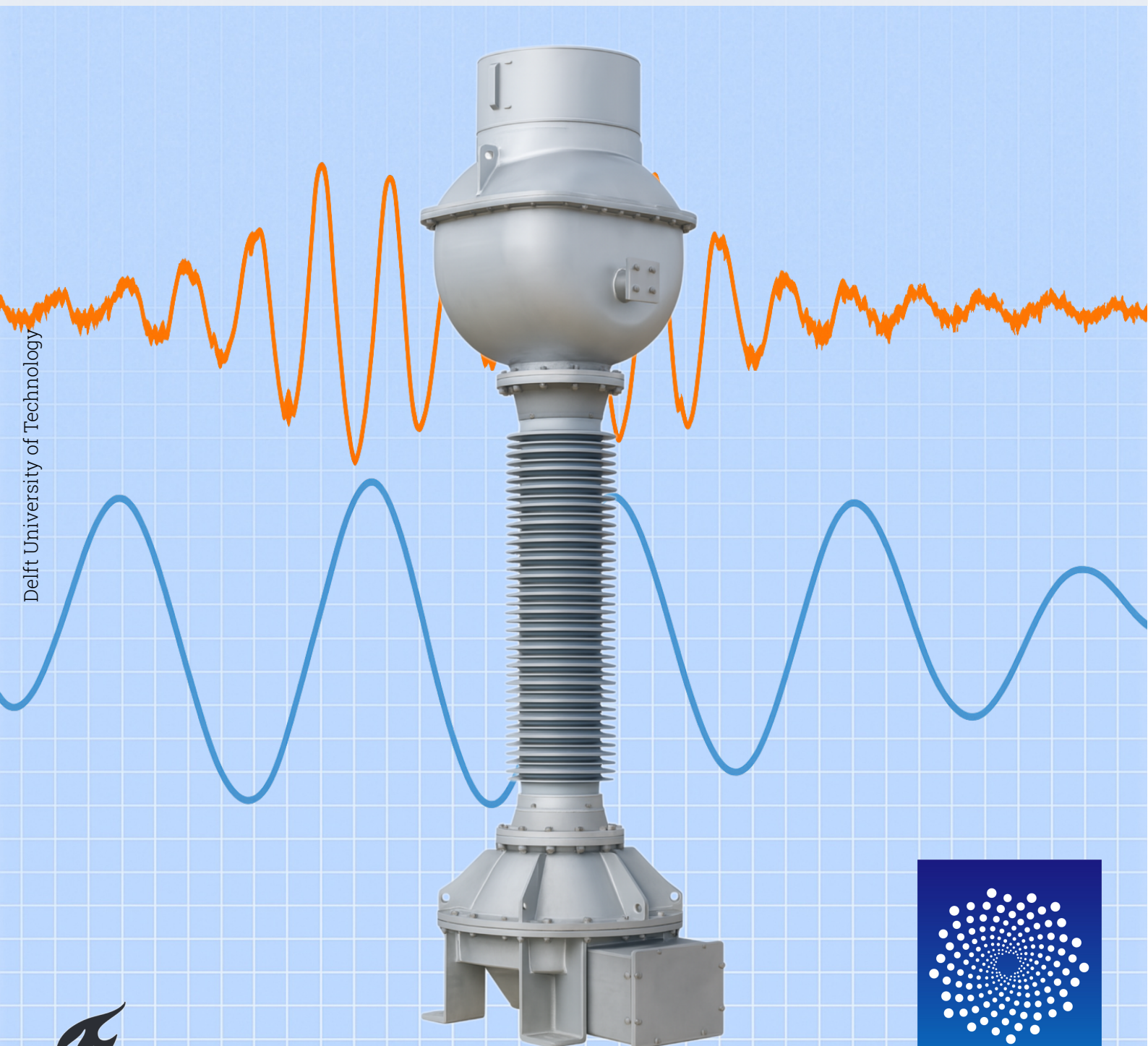
Mano Rom

Delft University of Technology

TUDelft

VSL

Characterizing Noise and Expanding Calibration of Current Transformers for High-Frequency Applications

by

Mano Rom

to obtain the degree of Master of Science

at the Delft University of Technology,

to be defended publicly on Friday July 11, 2025 at 13:00.

An electronic version of this thesis is available at `http://repository.tudelft.nl/`.

TUDelft

Abstract

The increasing integration of renewable energy sources and power electronic devices is changing the electricity grid, leading to widespread harmonic and suprarmonic distortions. Accurate measurement and calibration of current transformers (CTs) up to the 150 kHz range are essential for reliable power quality assessment and grid monitoring. However, traditional calibration approaches are limited in both bandwidth and practicality, particularly for high-current and high-frequency conditions.

This thesis develops and validates a broadband calibration methodology for CTs, enabling ratio and phase error characterization from 50 Hz to 150 kHz using a high-precision digital sampling ammeter (from a power analyser) as the core measurement instrument. The proposed system eliminates the need for auxiliary equipment and thus reduces component count, ultimately allowing for simplified broadband calibrations. An uncertainty budget is established with combined expanded uncertainties (k = 2) for the measurement system of less than 10 ppm up to 10 kHz, and less than 100 ppm at 150 kHz for the secondary-to-secondary comparison method. This is an improvement over the previous state of the art for this setup, which had an uncertainty of 50 ppm and a maximum frequency of 10 kHz. For primary-to-secondary calibration, uncertainties remain below 110 ppm at the highest frequency, allowing for the further development of a reference current transformer.

The thesis systematically examines the influence of critical experimental factors, such as grounding configuration, shunt selection, conductor positioning, cabling, and measurement duration, on overall calibration accuracy and repeatability. Key findings include the importance of instrument warm-up, the impact of earth-loop currents, and practical considerations for shunt and cable selection for high-frequency application. The demonstrated approach provides a metrological foundation for future implementation of wideband CT accuracy classes and supports ongoing international efforts to establish traceable measurement infrastructure for power quality applications.

This work, carried out at the Dutch national metrology institute (VSL), aims to contribute to the goals of the European ADMIT project.

Acronyms

AA-filter anti-aliasing-filter.

AC alternating current.

ADC Analogue to Digital Converter.

ADMIT AC and DC Medium-Voltage Instrument Transformers.

BIPM Bureau International des Poids et Mesures.

CIPM MRA CIPM Mutual Recognition Arrangement.

CT current transformer.

DC direct current.

DFT Discrete Fourier Transform.

DUT Device Under Test.

EU European Union.

EURAMET European Association of National Metrology Institutes.

FFT Fast Fourier Transform.

GUM Guide to the Expression of Uncertainty in Measurement.

HFD high-frequency distortion.

IEC International Electrotechnical Commission.

IEEE Institute of Electrical and Electronics Engineers.

IT instrument transformer.

IT4PQ Instrument Transformer for Power Quality.

Mtoe million tonnes oil equivalent.

MV medium-voltage.

NMI National Metrology Institutes.

PA power analyser.

PQ power quality.

PV photovoltaic.

SDT Step-Down Transformer.

VT voltage transformer.

WB wideband.

Contents

<div style="text-align: right; font-size: 3em;">1</div>

<div style="text-align: right;">

Introduction

</div>

1.1. Background and Context – The Green Transition

1.1.1. The European Commission's Ambitious 2030 Energy Goals

With a strong commitment to sustainability and climate change mitigation, the European Commission has set ambitious targets for the integration of renewable energy sources into the electricity grid [1]. Initial plans called for a 20 % share of renewable energy by 2020, a milestone achieved by late 2019; by 2020, 22 % of all energy originated from sustainable sources [2].

In 2018, the European Green Deal was introduced, accelerating these goals by requiring all European Union (EU) member states to reach 32 % renewable energy. However, the 2021 energy crisis, along with growing protests, the electoral success of green parties, and the urgent need to reduce dependence on Russian gas, prompted the Commission to further increase the European wide target to 42.5 %, with a goal of 45 % by 2030. Due to the varying circumstances and capabilities across member states, no country-specific targets were imposed.

According to Eurostat [3], 2023 saw the largest annual increase to date, with a 1.5 % rise to 24.5 % renewable energy—equivalent to an additional 5 million tonnes oil equivalent (Mtoe). This growth was primarily driven by a 28 % increase in solar power and a 6.6 % increase in wind power. Meanwhile, non-renewable energy sources declined by 2.9 %, largely due to higher gas prices and nuclear plant closures. Although more projects are coming online each year, the overall growth rate has slowed since 2020. To achieve the 2030 target, the rate of new project development will need to double [3].

1.1.2. The Changing Grid

The drive for a greener economy is fundamentally transforming three key aspects of the electricity grid, as described in [4], [5]:

First, the energy landscape is shifting from large, centralized power plants towards smaller, decentralized production facilities. For instance, in the Netherlands, nearly 18 % of total net electricity production in 2023 came from solar panels [6], [7]. The total installed capacity in 2023 was spread over 2.8 million installations, with 2.5 million of those on homes. The average power of residential systems was around 4 kW. Businesses had an average capacity per installation of around 60 kW. These photovoltaic (PV) installations make heavy use of direct current (DC) to alternating current (AC) power converters.

Secondly, demand patterns are changing. Electric vehicles are a prominent example, but the shift from gas heating to electric (including heat pumps) could have an even bigger impact on the grid. By December 2024, there were about 560 000 battery electric vehicles and 370 000 hybrids in the Netherlands [8], all requiring charging infrastructure. Rapid "super chargers" also convert AC to DC to power vehicle batteries. At the end of 2024, the Netherlands had over 150 000 public chargers, and 5000 super chargers [9], [10]. This gives them the highest density of chargers of any European Country, and thus a high density of AC to DC converters.

Power electronics, particularly inverters, are used to convert DC to AC and vice versa [11]. Inverters rapidly switch DC input signals, generating AC outputs. However, this rapid switching inherently produces non-sinusoidal ("chopped") waveforms. These distortions negatively affect power quality on the nearby grid [12], as illustrated in Figure 1.1.

(a) Example Output from an Inverter   **(b)** Grid Without and With Inverter
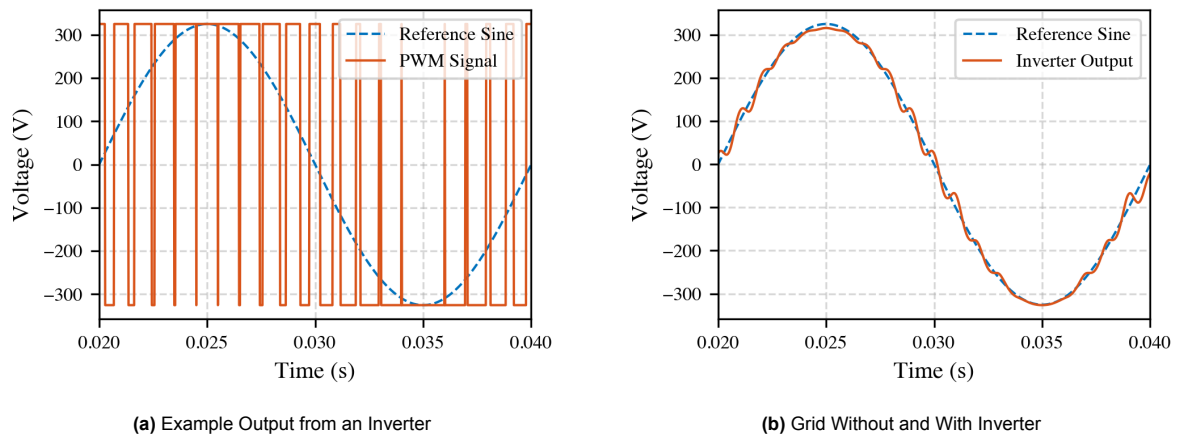
Figure 1.1: Scenario where high penetration of power inverters alters the grid voltage and current waveform. This example is at the household level, however, distortions can propagate to other parts of the networks.

Because many new sources generate DC power, an equivalent number of inverters is required. With 2.8 million solar installations across the Netherlands, this means at least 2.8 million inverters must be connected to the grid. Each of these inverters injects some harmonic distortion.

Thirdly, more of the grid's power lines are going underground to reduce visual impact, lower maintenance costs, and improve reliability under adverse weather conditions. In the Netherlands, around 100 % of the low-voltage distribution network and > 95 % of the medium-voltage network is laid underground [13]–[15]. Burying lines alters the network capacitance and can shift resonant frequencies, potentially amplifying certain harmonics and distortion phenomena. Hence, underground cables can intensify the effects of frequency-dependent disturbances.

The combined impact of increased renewable integration, widespread use of power electronics, and the physical changes in the grid infrastructure has led to new and complex power quality challenges, most notably in the form of harmonic and supraharmonic emissions. Understanding and quantifying these disturbances has become an area of research and engineering practice.

1.1.3. Harmonic Emission Measurement and Effects
Recent studies have highlighted the substantial presence of high-frequency disturbances in power distribution networks, particularly those with a high penetration of renewable energy sources. For example, [12] reported pronounced disturbances at 16.1 kHz, along with a primary emission at 2.5 kHz, both traced to photovoltaic installations connected to the grid. Similarly, [16] identified a dominant emission at 10 kHz originating from the switching frequencies of wind turbine converters. Their frequencies shift in response to the turbine's operational speed, especially during periods of low wind, when converter switching frequencies ranged from 7 kHz to 10 kHz.

Further investigations [17], [18] have revealed high-frequency disturbances in both voltage and current, with spectral components spanning 2 kHz to 50 kHz, with peaks at 12.5 kHz, 16.1 kHz, and 34.1 kHz. The amplitudes of these supraharmonic emissions are reported at approximately 0.1 % for voltage and 0.25 % for current. In scenarios with high levels of PV integration, distinct frequency components at 10 kHz, 26 kHz, and 36 kHz have been observed [18]. The same study documented an emission at 126 kHz with an amplitude of 0.15 V, likely linked to resonances in inverter filter networks and their interaction with the grid.

These supraharmonic distortions in medium-voltage distribution grids are recognized as damaging for several reasons. First, fast voltage transitions (high dV/dt exceeding 100 kV/μs) can reduce the par-

tial discharge inception voltage, accelerating insulation ageing and potentially shortening insulation lifetimes by an order of magnitude [19]–[21]. Second, as frequency increases, eddy current and proximity losses within transformer windings grow exponentially, resulting in elevated hotspot temperatures (sometimes by as much as 10–15,°C) imposing additional thermal stress on critical components [22]. Supraharmonic currents can also unintentionally trigger protective devices or generate audible noise in low-voltage switchgear, with sound levels reported above 50 dB(A) [21]. Finally, these disturbances can propagate through transformer windings from the medium-voltage grid into low-voltage circuits, contributing to flicker in LED lighting, interfering with power line communication systems, and ultimately causing malfunction or failure of sensitive domestic appliances and IT equipment [20], [23].

The economic impact of poor power quality (PQ), including the effects of harmonics and supraharmonics, is significant. Across the EU, the cost to industry is estimated at around €150 billion annually [24]. Faced with these high costs, governments and grid operators have become increasingly interested in quantifying the level of distortion present in their networks. To support this, manufacturers must develop measurement equipment capable of detecting and quantifying these disturbances, while purchasers demand assurance that the instruments they acquire are both accurate and reliable.

In addition to these measurement challenges, a question for grid operators is whether existing, preinstalled metering and protection instrument transformers can be effectively used to monitor supraharmonic currents and voltages. Since these harmonics are likely to propagate through instrument transformers, their secondary outputs could potentially be used for power quality monitoring. However, to ensure meaningful results, it is important to characterize and quantify how input signals are transferred through instrument transformers at higher frequencies. For this application, a measurement accuracy of around 1-5 % is probably considered sufficient for grid monitoring purposes.

These evolving power quality challenges, driven by the proliferation of supraharmonics and the need for practical, network-wide monitoring, directly expose gaps in current metrology and standardization practices.

1.2. Problem Statement—Power Quality and Metrology

To address these measurement needs, several initiatives within Europe are now focused on bridging gaps in standards and improving methodologies for power quality assessment, particularly at frequencies above 2 kHz. Notably, the European Association of National Metrology Institutes (EURAMET) project ADMIT, an international collaboration among European National Metrology Institutess (NMIs), is dedicated to developing traceable calibration methods and comprehensive standards for power quality measurements up to 150 kHz [25]. This work is being carried out at VSL, the Dutch National Metrology Institute, they have an operational 50 Hz CT calibration laboratory, giving them both the equipment and expertise to expand calibration capabilities up to 150 kHz.

At the international level, standards organizations, including the Institute of Electrical and Electronics Engineers (IEEE) and International Electrotechnical Commission (IEC), have recognized similar measurement challenges. Both IEEE Std 519 and the IEC 61000-series standards are undergoing active revision to better address high-frequency power quality phenomena that arise from the growing use of inverter-based resources [26]–[28].

Despite this progress, a gap remains when measuring power quality on high-voltage and medium-voltage grids, where primary currents can reach 10 kA, far exceeding the input range of conventional power quality measurement equipment (typically limited to 30 A and 230 V). The solution in practice is to utilize existing grid instrument transformers (ITs), which step down the primary current to a manageable secondary value. While these ITs are well-characterized at the fundamental frequency (50 Hz), with, for example, a 1000:1 ratio and 0.5 % uncertainty, existing international standards (such as the IEC 61000 series) focus mainly on disturbances measured at the instrument level and do not address errors introduced by ITs themselves.
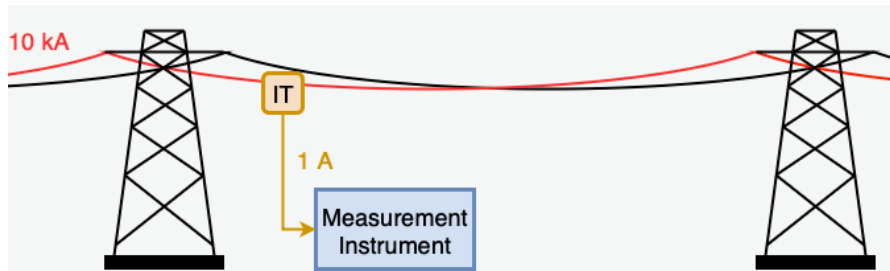
Figure 1.2: A high-voltage transmission line carrying 10 kA primary current, with an instrument transformer reducing it to 1 A for the measurement instrument.

Establishing a robust metrological framework for these ITs is therefore essential for effective power quality monitoring. Traceability to national or international standards ensures that grid operators and regulatory bodies can compare and validate data with confidence, and that calibration of measurement instruments is consistent across different countries and manufacturers.

However, despite the central role of ITs in delivering accurate grid voltage and current signals, no dedicated standards currently exist for their characterization in power quality applications at frequencies above 2 kHz. This is a critical shortcoming, as ITs can introduce amplitude and phase errors, compromising overall measurement accuracy [24]. At present, to the best of the authors knowledge, no NMI declares calibration capabilities for current transformers (CTs) up to 150 kHz, creating a gap for grid operators, manufacturers, and calibration laboratories seeking reliable and traceable power quality measurements across this extended frequency range.

Nonetheless, it is important to note that calibration laboratories still maintain traceability to national metrology institutes for current transformer calibrations up to 10 kHz. Several laboratories across Europe and beyond can achieve calibrations in this frequency range. For example, the comparator system described in [29] achieved expanded uncertainties (k = 2) of several hundred parts per million for ratio error and a few microradians for phase error up to 9 kHz. Similarly, the reference setup presented in [30] reached uncertainties of ± 20 ppm and ± 20 µrad at the fundamental frequency, increasing to ± 400 ppm and ± 800 µrad at 9 kHz.

1.3. Project Objectives

Although recent advances have expanded CT calibration capabilities, key gaps remain. Most existing measurement systems and calibration techniques are only validated up to 10 kHz, leaving the supraharmonic frequency range (10 kHz to 150 kHz) largely unaddressed [30]. Furthermore, many calibration setups depend on auxiliary equipment—such as current transducers and reference shunts—whose own frequency responses must be characterized, complicating traceability at higher frequencies [31]. Even recent digital comparator methods, while reducing operational complexity, have not been thoroughly validated above 10 kHz, and lack a comprehensive uncertainty assessment that includes the influence of practical setup choices and measurement chain components [32].

Consequently, despite the introduction of wideband accuracy classes (WB0–WB4) up to 500 kHz in IEC 61869-2 [33], the metrological infrastructure to support reliable wideband CT calibration is not yet fully established.

This work contributes to a larger project called ADMIT [25], currently being carried out by several European NMIs. ADMIT's goal is to develop traceable measurement methods and procedures for characterizing AC and DC medium voltage instrument transformers up to 150 kHz. Ultimately, the ADMIT project supports the revision of international standards and enhances the reliability of power quality measurements. ADMIT stands for "AC and DC medium-voltage (MV) Instrument Transformers".

1.4. Thesis Organization

This thesis is organized into four main parts, each building upon the previous to provide a thorough investigation of wideband current transformer characterization.

Part I: Foundations introduces the theoretical background and essential terminology for readers of all experience levels. Chapter 2 provides a foundational literature review, covering the core concepts and language necessary for understanding power quality measurement and instrument transformers. Readers new to these subjects are encouraged to read this chapter in detail, while those already familiar may wish to use it as a reference. Chapter 3 presents a more topic specific literature review, examining the latest advancements, state-of-the-art methodologies, and identifying key gaps in the fields of power quality and instrument transformer characterization as they relate to this research.

Part II: Experimental Methodology details the measurement setup and analytical approaches developed for this thesis. Chapter 4 outlines the design, construction, and operation of the experimental setup, including all relevant methods and equipment. Chapter 5 explains the algorithms employed for accurate current amplitude estimation and compares the selected method's performance with alternatives.

Part III: Experimental Results presents the findings from the measurement campaigns and justifies the chosen experimental design. Chapter 6 reports the results obtained using the reference setup as described in the previous chapters, and establishing a baseline for subsequent comparisons. Chapter 7 investigates the system's measurement behaviour, focusing on noise and repeatability. Chapter 8 analyses the impact of various alternative configurations and design decisions, with the goal of identifying sources of measurement error and optimizing accuracy. It will also try to answer some common industrial calibration laboratories questions about current transformer calibration.

Part IV: Interpretation and Conclusions Chapter 9 summarizes the quantified uncertainties associated with each experimental factor, providing a consolidated uncertainty budget for the final measurement setup. Chapter 10 interprets the results, placing them in the context of existing literature and current industry needs and assesses the broader impact of the research, acknowledges its limitations, and offers recommendations for future work.

Part I
Foundations

2

Background

In this chapter, the fundamental concepts are introduced related to power quality (PQ), harmonic distortions (including supra-harmonics), and the role of instrument transformer (IT) in measurement systems. Additionally, an overview of metrological principles is provided, outlining standards and practices. This background aims to equip readers with the necessary context for understanding the challenges and objectives of this thesis. In the next chapter, a more subject specific literature survey is performed.

2.1. Power Quality

PQ describes how closely the voltage, current, and frequency in an electrical power system conform to their ideal (typically sinusoidal) values [34]. Deviation from these ideals can arise from both generation (e.g., photovoltaic inverters) and loads (e.g., induction motors), introducing a variety of disturbances. Some of these, such as grid frequency changes, evolve slowly, while others, like switching transients, appear suddenly and can be highly dynamic.

Common power quality phenomena include voltage sags, swells, frequency deviations, and spectral distortions such as harmonics and supraharmonics [35]. While traditional PQ analysis often focuses on harmonics (integer multiples of the fundamental frequency), this thesis centres around the growing interest in high-frequency distortion—components well above the nominal 50 Hz or 60 Hz, including what is often termed supraharmonic distortion (distortions over 10 kHz).

2.1.1. Sources of Power Quality Disturbances

A wide variety of industrial and residential sources contribute to power quality disturbances. In industrial environments, equipment such as variable frequency drives, electric motors, and welding machines inject non-linear currents that distort the voltage and current waveforms [34], [35]. The rapid rise of renewable energy installations, particularly solar inverters, has further increased the prevalence of non-sinusoidal and high-frequency phenomena, producing not just harmonics but also significant interharmonic and supraharmonic distortion [5], [36].

2.2. Harmonic and High-Frequency Distortion

The voltage or current in a power system can be mathematically described as a sum of a fundamental component (50 Hz or 60 Hz) and additional frequency components:

$$f(t) = \sum_n A \cos\left(n \times 2\pi f_0 t + \theta\right). \tag{2.1}$$

These additional components are broadly termed harmonic distortion. However, real-world distortion also includes interharmonics and, of relevance to this thesis, high-frequency and supraharmonic components [5], [37]. DC components, which pose their own risk, require different techniques and considerations, are excluded from the present scope.

High-frequency distortion is characterized by significant spectral content above the traditional harmonic range, extending from 10 kHz up to 150 kHz or beyond [38], [39]. These supraharmonic frequencies are an increasing concern in both MV and LV grids as more power electronic devices are connected. By contrast, the HV transmission system is not covered in this thesis. Because HV feeders are long and exhibit a high characteristic impedance, supraharmonic currents injected at one substation are heavily damped and believed not to propagate beyond the immediate neighbourhood of their source. Field measurements confirm that voltages and currents in the 2 kHz to 150 kHz range "are generally assumed to have a short distance of propagation" and are quickly attenuated along the line [40], [41]. Consequently, supraharmonics originating in HV networks are unlikely to reach the MV/LV interface where they could endanger customer equipment, allowing this work to focus on MV and LV grids where the impact is presumably highest.

2.3. Instrument Transformers

ITs are critical components in modern power systems, providing a means to scale high voltages and currents in transmission and distribution networks down to levels suitable for measurement instruments, protective relays, and monitoring equipment. In addition to enabling safe and accurate metering, ITs provide galvanic isolation, protecting low-voltage instrumentation and personnel from hazardous grid voltages and currents. The design, testing, and performance of instrument transformers are governed internationally by the IEC 61869 series of standards.

Part 1 (IEC 61869-1 [42]) outlines general requirements such as terminology, rated values, insulation coordination, and essential test procedures applicable to all types of instrument transformers. Subsequent sections, including IEC 61869-2 [43] (current transformers) and IEC 61869-3 [44] (inductive voltage transformers), expand these requirements with type-specific criteria, focused on the conventional power frequency range (typically 10 Hz–100 Hz), with some consideration for frequencies up to 2 kHz.

2.3.1. Fundamentals of Instrument Transformers

Instrument transformers operate by electromagnetic induction (for current and inductive voltage transformers) or capacitive voltage division (for capacitive voltage transformers). Their primary function is to provide an accurate and stable scaling—or ratio—between the primary and secondary quantities (current or voltage).

The accuracy of instrument transformers is classified according to standardized accuracy classes (e.g., 0.2, 0.5, 1, 3), which specify the permissible error in both magnitude and phase (as a percentage) under nominal conditions. While these classes are well established for conventional power system operation at 50/60 Hz, they provide limited guidance for performance at higher frequencies. To address this gap, IEC 61869 has introduced optional wideband (WB) accuracy classes (WB0 to WB4), extending standardized performance definitions up to 500 kHz. Of direct relevance to this work is the WB3 class, which covers the 50 Hz to 150 kHz range, encompassing the supraharmonic emissions produced by modern power electronic converters (see also the Introduction). Although these new classes provide a framework for assessing high-frequency behaviour, many practical manufacturing and testing details remain under development, and compliance is not yet mandatory.

2.3.2. Current Transformers

CTs, defined in IEC 61869-2 [43], are used to replicate primary currents, often hundreds or thousands of amperes, at a reduced level (commonly 1 A or 5 A) suitable for regular measurement instruments. The standard CT design consists of a toroidal iron core with secondary windings, optimized for accuracy, linearity, and thermal stability. CTs are deployed both for measurement and for protection applications. Key performance parameters include the accuracy class, rated burden (specified in ohms or volt-amperes), and permissible thermal limits.

Figure 2.1: 110 kV Current transformer [45]

Operating Principle of Current Transformers

A current transformer functions by electromagnetic induction: the primary conductor (carrying the high grid current) passes through the CT core and produces a time-varying magnetic flux, which in turn induces a proportional current in the secondary winding. For an ideal CT, this relationship is given by:

$$I_s = I_p \times \frac{N_p}{N_s},$$

(2.2)

where I_p is the primary current, I_s is the secondary current, and N_p/N_s is the ratio of primary to secondary turns [46]. In practice, the actual transformation ratio can be affected by non-idealities such as core losses, stray capacitance, and magnetization current, especially at higher frequencies.

Equivalent Circuit of Current Transformers

To analyse and predict the behaviour of a CT across a broad frequency range, it is useful to consider its equivalent circuit model [47].
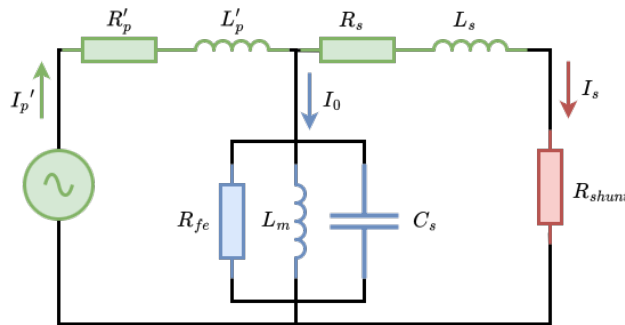
Figure 2.2: Equivalent circuit (T-model) of a current transformer.

As shown in Fig. 2.2, the equivalent circuit includes: the primary impedance (referred to the secondary, R_p', L_p'), magnetizing branch (R_{Fe}, L_m), secondary impedance (R_s, L_s, C_s), and the connected load or burden (R_{shunt}). The total primary current I_p' splits into a magnetizing current I_0 (which establishes the magnetic flux in the core) and the secondary current I_s delivered to the burden [46]. At higher frequencies, parasitic capacitances, increase core losses, which can significantly influence CT accuracy, reinforcing the importance of careful characterization and calibration in the supraharmonic range.

As industry demand grows for reliable, traceable measurement at high frequencies, it is essential that all manufacturers and users evaluate their devices against common reference standards. In most countries, national metrology institutes maintain these standards and provide reference values that enable

harmonization and comparability between different laboratories, manufacturers, and grid operators. The next section discusses the organization and role of the metrological infrastructure that supports such traceable measurements.

2.4. Introduction to Metrology and Measurement Accuracy

Modern power quality measurements, require not only advanced instrumentation, but also a robust framework for ensuring that measurement results are reliable, comparable, and internationally accepted. This framework is provided by metrology, the science of measurement. Metrology establishes the theoretical and practical foundation for achieving consistency, reliability, and traceability in all quantitative assessments, from basic laboratory research to industrial power system diagnostics.

A few fundamental metrology concepts are essential for power quality measurement and, by extension, for this thesis:

- *Traceability*: The property of a measurement result whereby it can be related to a reference (usually an international or SI standard) through an unbroken chain of calibrations, each contributing to the overall uncertainty.

- *Measurement Uncertainty*: A quantified estimate of the doubt about a measurement, typically expressed as a range within which the true value is believed to lie with a specified level of confidence [48], [49].

- *Calibration*: The process of comparing a measurement instrument or standard with a reference of known accuracy, thereby quantifying and, if necessary, correcting systematic deviations. You can never get a more accurate reading than the reference's accuracy. This is the reason NMIs put such effort into high-quality results, because if the reference is inaccurate, the measurements that follow will only be worse. On the other hand, a highly accurate reference simplifies calibrations as less care can be taken at the calibration laboratories, and still achieve a desired uncertainty.

2.4.1. National Metrology Institutes and the Metrology Infrastructure

To enable such traceability, every country maintains an NMI, which is responsible for developing, maintaining, and disseminating primary measurement standards. NMIs such as VSL (Netherlands), PTB (Germany), NPL (UK), and LNE (France) provide the highest reference for quantities like voltage, current, and resistance. Their role is foundational: they ensure that all calibrations performed within their national borders, and by extension all measurements that rely on them, are tied to internationally recognized standards.

NMIs work together through organizations like EURAMET (Europe) and Bureau International des Poids et Mesures (BIPM) (globally). The CIPM Mutual Recognition Arrangement (CIPM MRA) underpins this cooperation, guaranteeing that calibration certificates from any signatory NMI are accepted internationally. This is crucial for global industry and scientific research, facilitating trust, trade, and regulatory compliance [50].

Within this landscape, VSL—the Dutch NMI and the host institute for this research—develops and maintains the primary electrical standards relevant to this work, including those for resistance, voltage, and current. VSL also participates in collaborative European research projects (such as IT4PQ and ADMIT) aimed at developing new calibration methods and reference setups for emerging PQ challenges, particularly in the area of high-frequency distortion.

2.4.2. Uncertainty Evaluation in Electrical Measurements

A core objective in metrology is not only to report measurement results, but also to quantify the associated uncertainty. The internationally recognized framework for uncertainty evaluation is the Guide to the Expression of Uncertainty in Measurement [51], which underpins both laboratory practice and standardization in electrical engineering.

Measurement uncertainty represents the range within which the true value of the measurand is estimated to lie, with a specified level of confidence. The process of uncertainty evaluation in the GUM framework is structured as:

- **Type A evaluation** refers to uncertainties evaluated by statistical analysis of a series of repeated measurements. For example, the standard deviation of the mean from repeated ratio measurements or phase measurements falls into this category.

- **Type B evaluation** encompasses all other sources of uncertainty that are not evaluated statistically, but are instead based on scientific judgment using all available information. This may include calibration certificates, instrument specifications, manufacturer data, or previous experience.

After identifying all significant sources of uncertainty—both Type A and Type B—they are combined, by root-sum-square, to obtain the combined standard uncertainty (u_c). To provide a meaningful confidence interval, this is then multiplied by a coverage factor (k). For a normal (Gaussian) distribution, k = 2 corresponds to an approximate 95 % confidence interval, which is the convention adopted in most calibration and research laboratories.

2.4.3. The Traceability Pyramid

The process by which measurement accuracy and traceability propagate through the measurement community is often illustrated by the traceability pyramid (see Fig. 2.3). At the apex are the SI units and international standards. These are disseminated to NMIs, then to accredited calibration laboratories, and finally to industry and end users. At each stage, the uncertainty typically increases, but so does accessibility and applicability.
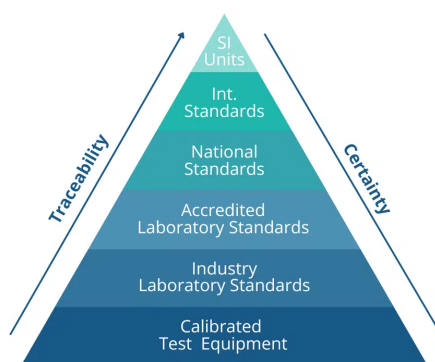
Figure 2.3: Illustration of the Metrology Traceability Pyramid (by AST [52]).

The Role of Metrology in Power Quality Research

While primary standards (such as those based on the quantum Hall effect for resistance) are highly stable and accurate, they are not directly applicable to field measurements or PQ instrumentation. The challenge, and the focus of initiatives like ADMIT and IT4PQ, is to translate these fundamental standards into practical calibration tools for industry.

This research, directly supports this effort. By improving calibration techniques for high-frequency measurements and quantifying their uncertainties, the work contributes to the broader goal of making high-frequency PQ assessment traceable, reliable, and internationally accepted.

Literature Review

3.1. The ADMIT Project

The developments in this thesis aim to contribute to a project called ADMIT. The ADMIT project [25], builds upon the foundations established by Instrument Transformer for Power Quality (IT4PQ).

Key objectives of ADMIT include:

- **Defining Accuracy Parameters:** Establishing performance indices and accuracy limits for CTs operating up to 150 kHz, ensuring precise PQ measurements in the presence of high-frequency distortions (HFDs).
- **Developing Reference Systems:** Creating measurement systems and testing conditions that accurately characterize CTs under various scenarios.
- **Evaluating Influence Quantities:** Investigating the impact of factors such as temperature, humidity, vibrations, and proximity effects on CT performance across the extended frequency spectrum.
- **Contributing to Standardization:** Providing empirical data to influence the development and revision of international standards related to ITs and PQ measurements in modern power systems.

3.2. Complex Ratio Error of a Current Transformer

In an ideal scenario, a CT would reproduce the primary current waveform at its secondary winding exactly, scaled by a constant transformation ratio $n = I_p/I_s$. This means both the amplitude and phase of the primary current would be perfectly preserved after scaling.

However, in practice, CTs exhibit both amplitude and phase errors. These errors are frequency-dependent and arise due to a combination of core magnetization effects, leakage reactance, and winding capacitances. To quantitatively describe the deviation of a CT from ideal behaviour, the concept of complex ratio error is used [53].

The complex ratio error, as a function of frequency f, is defined as:

$$\epsilon(f) = n \times \frac{I_s(f)}{I_p(f)} - 1,$$

(3.1)

where:

- n is the nominal transformation ratio of the CT,
- $I_p(f)$ is the primary current at frequency f,
- $I_s(f)$ is the measured secondary current at frequency f.

Here, $\epsilon(f)$ is a complex quantity whose magnitude gives the amplitude error (relative scaling error), and whose argument (angle) gives the phase error (phase displacement) introduced by the CT at frequency

f. Accurate knowledge of this complex error is essential for power quality monitoring. Small deviations in phase measurements, can have a big impact on how much power is effectively flowing.

3.3. Ratio-Based Approach for CT Characterization

Traditionally, characterizing CT performance over a wide frequency range would require direct measurement of the primary current, ideally using a wideband, high-current shunt resistor. However, commercial shunt solutions that operate linearly from 50 Hz up to 150 kHz and at the required current levels (up to several kiloamperes) are not available or are prohibitively complex.

To overcome this limitation, a ratio-based method is employed. In this approach, the device-under-test CT (subscript X) is connected in series with a well-characterized reference CT (subscript R), such that both CTs experience the exact same primary current. This setup offers several advantages:

- **Elimination of direct primary current measurement**: Since the primary current is common to both CTs, it can be algebraically eliminated from the analysis, removing the need to measure it.
- **Simplified time synchronisation**: Both secondary currents can be measured simultaneously by the same acquisition system, reducing errors related to timing or phase alignment between measurement channels.
- **Common-mode rejection**: Any slow drift, noise, or ripple in the primary current source is experienced identically by both CTs and thus cancels out when their ratio is computed.

The current measured on each CT secondary is given by:

$$I_{sX} = \frac{I_p}{n_X}\left[1 + \epsilon_X(f)\right], \qquad I_{sR} = \frac{I_p}{n_R}\left[1 + \epsilon_R(f)\right], \tag{3.2}$$

where n_X and n_R are the nominal ratios for the DUT and reference CTs, respectively, and $\epsilon_X(f)$ and $\epsilon_R(f)$ are their respective complex ratio errors.

Taking the ratio of these two measurements yields:

$$\frac{I_{sX}}{I_{sR}} = \frac{n_R}{n_X}\frac{1 + \epsilon_X(f)}{1 + \epsilon_R(f)} \tag{3.3}$$

This relationship can be rearranged to solve for the unknown complex error of the DUT CT:

$$\epsilon_X(f) = \frac{n_X}{n_R}\frac{I_{sX}}{I_{sR}}\left[1 + \epsilon_R(f)\right] - 1 \tag{3.4}$$

Thus, provided the complex ratio error of the reference CT $\epsilon_R(f)$ is well-characterized, the error of the DUT can be determined over the frequency range of interest.

3.4. Overview of CT Calibration Methods

3.4.1. Classical 50 Hz Calibration Techniques

Early instrument-transformer calibration was performed exclusively at power frequency (50 Hz/60 Hz) using bridge or comparator arrangements [31], [54]. In a typical setup, a test CT and a multi-winding reference comparator share the same primary conductor, while their secondaries are connected in opposition so that any residual current directly represents the CT error [54]. A null detector and adjustable burden then drive this residual to zero, yielding the ratio and phase error of the device under test. While these classical methods can achieve ppm-level uncertainty, they provide no information beyond the fundamental frequency.

3.4.2. From Single-Frequency to Wideband Calibration

Modern grids contain harmonics, interharmonics, and suraharmonics extending beyond a couple kHz. Consequently, instrument transformers intended for 50 Hz service must also be characterised under wideband, non-sinusoidal conditions [55]. Several complementary approaches have been developed.

Calibration using a Shunt

One approach to CT calibration employs wideband shunts for direct primary current measurement. In [55], a composite current, consisting of a 50 Hz fundamental plus harmonics up to 5 kHz, is injected into the CT primary. A transconductance amplifier generates the test waveform, while two wideband coaxial shunts synchronously measure the primary and secondary currents [56]–[58]. Frequency-domain analysis is then used to determine the ratio and phase error at each spectral component.

Despite the conceptual simplicity of shunt-based calibration, substantial practical limitations emerge at high currents and high frequencies. In [59], coaxial manganin shunts capable of up to 10 kA are demonstrated with DC reproducibility at the 10 ppm level; however, their frequency response is limited to "tens of kHz." [60] reports the results of an NMI round-robin up to 100 kHz and 100 A, achieving phase uncertainties below 0.05 mrad and amplitude uncertainties in the 200 to 500 ppm range. Below the current rating needed for CT calibration, and above the uncertainty what is required for our application. There is still active research and development in this domain, so it is possible that in the coming years this equipment will be available [58].

Across decades of research, it is evident that no shunt currently exists which combines high current capacity (≥1 kA), wide bandwidth (up to 150 kHz), and accuracy (≤10 ppm) in a single package. This is precisely the motivation for the use of CTs in this research because they can operate at the kA current level and, when properly calibrated, maintain high linearity with increasing current.

Auxiliary equipment

An alternative approach is to directly compare a CT to reference CT, as shown in [53], [61], uses current transducers and current buffers, an approach that allows for high accuracy, but because of all this auxiliary equipment, each part requires calibration. It can achieve ppm-level uncertainty, but needs calibration of each component at every frequency. Making it unsuitable for wideband application. Moreover, the set-up in [53] relies on sampling voltmeters (e.g., HP 3458A with an effective 10 kHz bandwidth). A simplified set-up is thus desirable, allowing easier scaling to higher frequencies.
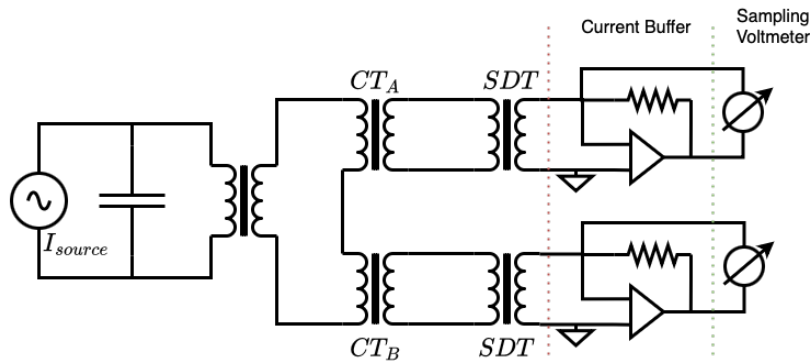
Figure 3.1: Schematic of a CT sampling current ratio measurement system. High primary currents are generated using a power amplifier and a step-up transformer. The CT under test is measured against a reference CT where both secondary currents are scaled down using Step-Down Transformers (SDTs). Operational amplifiers with precision AC resistors act as current buffers that convert current to voltage, while digital sampling voltmeters record the buffer voltage signals. [53]

Wideband Voltage Transformer Calibration

For voltage transformers (VTs) recent research is enabling wideband calibration, but this method is not suitable for CTs. [62] demonstrates a two-source technique for medium-voltage VTs: a 50 kV fundamental is generated by a step-up transformer, while low-amplitude harmonics (5 V) are injected through a capacitive network. A precision resistive–capacitive divider measures the primary voltage, and the VT secondary is digitised. Expanded uncertainties of 0.01 % at 50 Hz and 0.2 % to 1 % up to 150 kHz were achieved.

Digital Sampling Comparator Methods

To address these challenges and reduce system complexity, in [32] a two-channel, high-resolution power analyser (sampling ammeter) that functions as a digital comparator is introduced. In this setup,

the analyser simultaneously measures the secondary currents from both the reference and DUT CTs. Through coherent sampling and FFT processing, the system achieves an uncertainty of less than 35 ppm up to the 50th harmonic (2 kHz), and was shown to be able to measure up to 10 kHz. This approach significantly reduces the number of required components, while providing enhanced frequency coverage and streamlined procedures for wideband CT calibration.

Building upon this foundation, the present thesis adopts and extends this sampling ammeter methodology. In contrast to [32], which did not comprehensively assess the influence of system variations, or calibration performance above 10 kHz, this work expands the calibration range to 150 kHz, provides a full uncertainty budget, and systematically investigates the impact of grounding, cabling, primary conductor positioning, and other practical factors possibly affecting wideband CT calibration.

While digital sampling comparator methods represent a significant step forward in simplifying and extending wideband CT calibration, their effectiveness ultimately depends on the stability and accuracy of the reference CT used in the setup. To achieve ppm-level performance across a broad frequency range, modern reference CTs employ electronic compensation techniques. Which have been proven to lead to sub-ppm level ratio accuracy at the fundamental 50 Hz. The aim of these compensation mechanisms is to minimize any residual error. The next section provides a technical overview of the operating principle and compensation electronics used in the reference CTs used for this work.

3.5. Operating Principle of Electronically Compensated Current Transformers
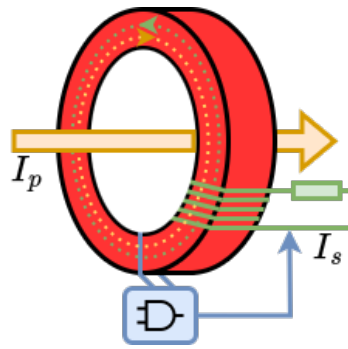
Figure 3.2: Operating Principle of a Current Transformer With Electronic Compensation [63], [64]

The CT consists of a magnetic core (red ring) with a primary conductor passing through its centre. The primary winding is typically just a single conductor, while the secondary winding consists of many turns of wire wound around the magnetic core. The direction of primary current flow (I_p) is indicated by the yellow arrow.

When current flows through the primary conductor, it generates a magnetic field within the core. According to Faraday's law of electromagnetic induction, this changing magnetic field induces a current in the secondary winding (I_s). The secondary winding is connected to a measurement circuit, usually with a known load or burden resistor. The current in the secondary winding ideally generates an equal but opposite magnetic field. However, because of factors explained in the previous chapter, this is impossible.

Therefore, to maintain accuracy, the CTs used in this experiment have compensation electronics (illustrated by the small circuit block in the image) [64], [65]. These electronics sense any remaining magnetic flux in the CT's core, which is an indication that too little current is flowing in the secondary to fully cancel out the magnetic flux, and inject a correction current into the secondary winding, driving the core flux to zero, minimizing the effects of core nonlinearity, leakage, and other sources of error. This allows the CTs used in this experiment, to achieve 1 ppm accuracy at 50 Hz, meaning that for a 1 kA primary current with a 400:1 ratio, the secondary current is accurate to 5 µA. One limitation, however, is the bandwidth of the amplifiers within these electronics, possibly not allowing them to compensate for high-frequency errors.

Part II
Experimental Methodology

4

Measurement Setup and Methodology

The primary objective of this research is to develop a simplified measurement set-up for characterizing the performance of an unknown current transformer over the frequency range from 50 Hz to 150 kHz.

A current transformer typically features a defined transformation ratio, such as 100:1. Under ideal conditions, applying a current of 10 A to its primary winding results in a secondary current of 100 mA. At the standard grid frequency of 50 Hz, this ratio is well-defined and can be made highly accurate. However, as frequency increases into the tens or even hundreds of kilohertz, standard CTs can exhibit deviations from their nominal amplitude ratio. Quantifying these deviations is therefore crucial, and one of the many services NMIs try to provide traceability for, so CT manufacturers can compare equipment, industry, and grid operators can trust the equipment they use, and regulators have a framework for standardization.

Ideally, one would measure the primary and secondary currents directly and determine the CT's ratio across this extended frequency range. However, as discussed in the previous chapter, measuring kiloampere-level currents directly at high frequencies poses significant practical challenges.

To overcome these limitations, this research uses an indirect measurement approach: instead of measuring absolute primary current, the technique involves comparing the unknown CT Device Under Test (DUT) against a well-characterized reference CT measuring the same current. For example, if both the DUT and a reference CT with a nominal ratio of 100:1 have a primary current of 1 kA, both should ideally produce a secondary current of 10 A. If the DUT produces only 9 A, it indicates a 10% error in its transformation ratio.

The core of this thesis thus centres around developing a measurement setup capable of accurately comparing secondary currents from two CTs simultaneously, under varying conditions and frequencies. The focus is not on creating the reference CT itself, but rather on the measurement setup and the methods necessary for achieving accurate, repeatable, and reliable measurements.

This chapter describes the experimental setup and procedures developed to characterize CTs across the frequency range of 50 Hz to 150 kHz. The core of the experimental approach is the relative comparison of secondary currents between the device under test CT and a reference CT. By placing both CTs in series and subjecting them to identical primary currents, the setup enables a direct ratio measurement of the secondary outputs. This ratio-based approach (see Section 3.3) isolates the influence of configuration changes and DUT variations, as any deviation in the measured ratio directly reflects the impact of the test condition or modification. A sampling ammeter channel interchanging technique, described in Section 4.2, is applied to further minimize systematic gain differences between measurement channels.

To validate and supplement the secondary-to-secondary current comparison, a direct primary-to-secondary current measurement is also conducted. In this method, the primary current (I_p) is measured simultaneously with the CT's secondary current (I_s) using a the same calibrated sampling ammeter (for ammeter calibration details see Appendix A). While this approach directly indicates the CT's absolute ratio error,

its accuracy is limited by the calibration of the ammeter and shunt resistor, especially at higher frequencies and elevated current levels. For this reason, the practical current range for direct measurements is typically limited to approximately 20 A, and uncertainties increase above 100 kHz due to the incomplete characterization of available shunts.

Overall, the measurement strategy prioritizes the reliability and repeatability of the secondary-to-secondary comparison as the principal means of CT characterization. The primary-to-secondary ratio measurement is employed primarily as a supporting method to validate findings and quantify the true absolute error under controlled conditions. This dual-method approach ensures that, once a fully characterized reference CT is available, the system can provide high-accuracy (with a known uncertainty) calibrations across the intended frequency range.

The remainder of this chapter outlines the measurement setup. The next chapter goes into detail about the algorithms used to determine the amplitude of the sampled current.

4.1. Standard Measurement System Description
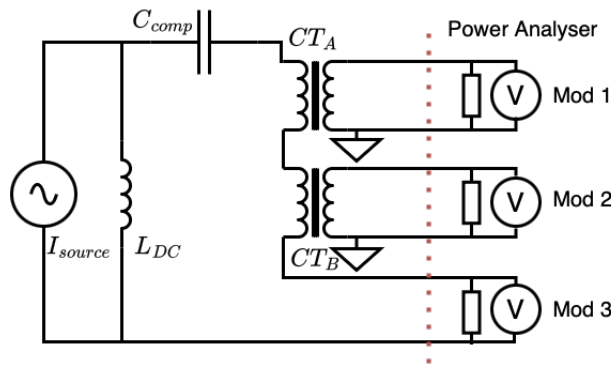
Figure 4.1: Schematic representation of the measurement setup where a high-current source feeds both the DUT CT and the Ref. CT. The secondary outputs are recorded for ratio comparison.

Figure 4.1 provides a schematic overview of the measurement setup employed for simultaneous characterization of the DUT and reference CT. A high-current source provides the necessary primary excitation current (I_p) at 10 A at one frequency from 50 Hz up to 150 kHz through both transformers connected in series. The power analyser current channels (sampling ammeter) measure the secondary currents using internal coaxial shunts. A compensation capacitor and inductor are incorporated into the current generation circuit of the setup to prevent DC magnetization of the CT cores and to provide series compensation for the circuit impedance.

4.1.1. Detailed Component Overview
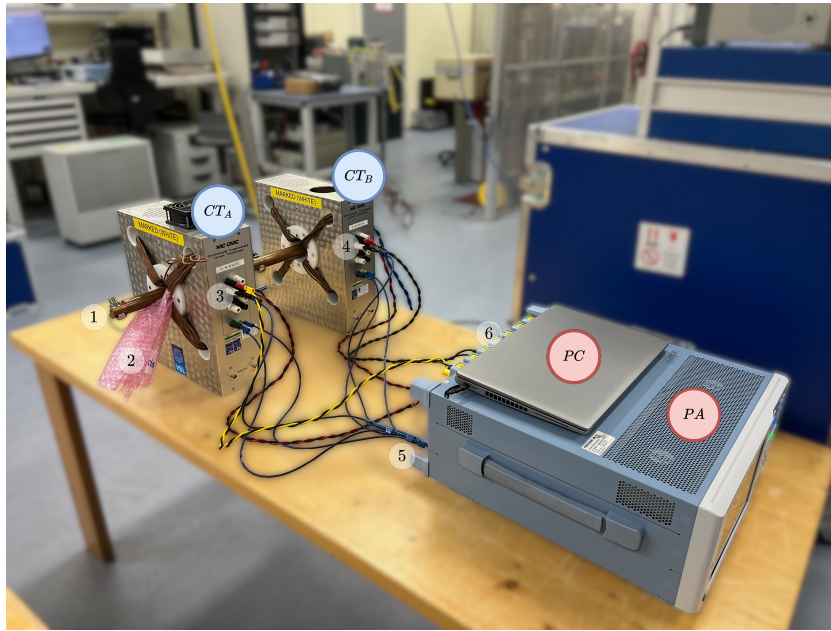
Figure 4.2: Photographic overview of the laboratory measurement setup.

The measurement campaign was carried out in a controlled laboratory environment, maintained at 22 °C ($\pm$0.5 °C) and 45 % ($\pm$5 %) relative humidity, enclosed within a Faraday cage to minimize electromagnetic interference. All measurement equipment is powered from a 58 Hz source, decreasing the power grid's 50 Hz interference. Key setup components include:

- **CTA and CTB**: Two nearly identical electronically compensated NRC current transformers [64], each serving as a primary standard for both current ratio and phase, were used as the DUT and reference in this study. These CTs offer accredited uncertainties better than 1 ppm in ratio and 1 µrad in phase at 50 Hz. As primary standards at 50 Hz, they provide a stable and traceable reference for both amplitude and phase calibration. Throughout this work, to study the effects of various experimental parameters, changes were typically introduced to CT A (DUT), and the resulting impact was evaluated by comparing the secondary-to-secondary current and phase ratio before and after each modification.

- **PA**: The Precision Power Analyser (YOKOGAWA WT5000) was utilised for voltage and current measurements, capable of sampling up to 2 MS/s. The analyser has interchangeable modules **(6)** with internal shunts of 6.5 mΩ (up to 30 A), 110 mΩ (up to 5 A), and 500 mΩ (up to 500 mA). The appropriate shunt selection and its impact on measurement uncertainty are detailed in Section 8.3. Throughout this work, the term "sampling ammeter" or "power analyser (PA)" refers to this instrument. The calibration and characterization of this instrument are detailed in Appendix A.

- **PC**: A laptop PC is used as Data Acquisition System connected via high-speed USB to the PA, which records and stores raw measurement data for subsequent analysis and processing.

- **1**: A copper bus-bar delivered the primary excitation current through both CTs simultaneously.

- **2**: Non-conductive, magnetically neutral plastic is used to centre the primary conductor within the CT's core to ensure consistent geometric conditions and reduce possible position-dependent variability. Although subsequent tests revealed minimal sensitivity to conductor position (see Subsection 8.5), this arrangement allows for separation of variables.

- **3 and 4**: Twisted-pair cables connect the secondary outputs of both CTs to the ammeter, minimizing induced interference. Additional cables measured the secondary voltage directly at the CT terminals for diagnostic and performance assessment purposes.

- **5**: A single-point grounding configuration was implemented to prevent ground loops and minimize electrical noise. In this setup, the star point was established at the ammeter. All components, including the CT secondary windings, CT compensation electronics, CT housings, and the high-current generation equipment were referenced to this common grounding point on the ammeter.

4.1.2. High-Bandwidth Power Amplifier System

To generate the required primary current of 10 A in the frequency range of 50 Hz to 150 kHz, a high-bandwidth power amplifier system was constructed, as illustrated in Figure 4.3. This system is designed to maintain stable, safe, and accurate current injection into the primary circuit under varying frequency-dependent load conditions. Because of the DUT and reference CT system are simultaneously measured, a small deviation/drift of a couple of percent deviation from the ideal current is not an issue.
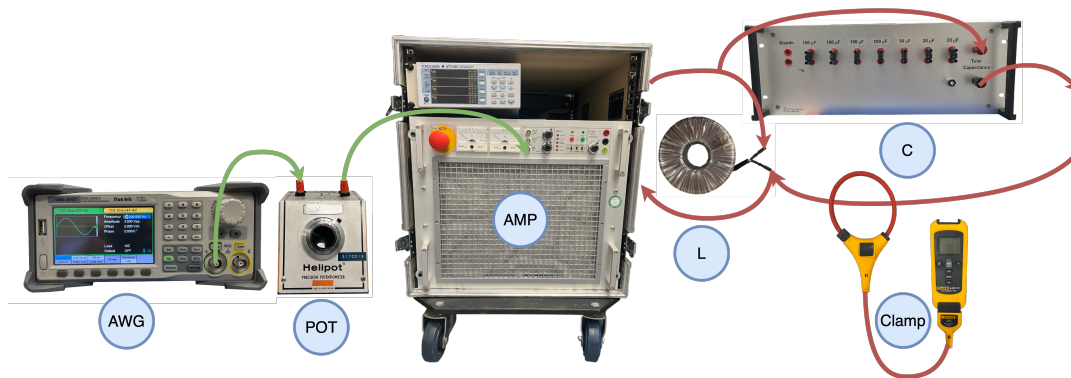
Figure 4.3: High-bandwidth power amplifier system. Capable of generating 10 A of primary current at 150 kHz.

The components and their functions are as follows:

- **Arbitrary Waveform Generator (AWG):** Provides a sinusoidal voltage output with programmable amplitude and frequency (50 Hz to 150 kHz).
- **Variable Potentiometer (POT):** Allows gradual adjustment of the input voltage to the power amplifier. As the impedance of the primary circuit changes with frequency, the potentiometer is used to fine-tune the output and achieve the target 10 A current, as verified by the clamp metre. This allows for a gradual and safe ramp-up of the primary current.
- **Amplifier (AMP):** Provides sufficient gain and drive capability to overcome the inductive and capacitive reactance of the primary circuit at high frequencies.
- **Inductor (L):** Connected in parallel with the CTs to divert any DC components originating from the amplifier. This is to prevent core magnetisation in the CTs, which could lead to measurement errors.
- **Compensation Capacitor (C):** Placed in series with the CTs, this capacitor helps to block DC and further ensures that only AC current is present in the measurement circuit. It also helps with series compensation of the long cable connected that loops through the CTs.
- **Current Clamp (Clamp):** Provides a convenient means for real-time monitoring and adjustment of the primary current during ramp-up and operation. Accurate measurement of the primary current is done using the sampling ammeter, not the current clamp.

To ensure standardized and consistent characterization, the regular setup applies a primary current of 10 A to the CTs, each configured with a 100:1 turns ratio. The primary current is tested at a series of discrete frequencies: 50 Hz, 100 Hz, 200 Hz, 500 Hz, 1 kHz, 2 kHz, 5 kHz, 10 kHz, 20 kHz, 50 kHz, 75 kHz, 100 kHz, 125 kHz, and 150 kHz (a total of 14 points). These frequency points were selected

to provide approximately three measurement samples per decade (with some extra points at higher frequencies, as this is most crucial for this research).

4.2. Ammeter Module Interchanging for CT Characterization

In order to characterise and calibrate a DUT CT, it is measured against a reference CT. If they are measuring the same primary current, their secondary currents can be compared, resulting in a ratio between the DUT and reference CT secondary current. Assuming the reference is well known, the error or the CT under test can be determined by this relative ratio (more details on this in Section 3.3). This work did not contain a formal 'reference' CT, rather two identical CTs are used, to help characterize the system set-up. In order to not give the impression of a reference CT, CTA and CTB are used to name, the two CTs.

Let the nominal step-down ratios of CTA and CTB be denoted as n_{CTA} and n_{CTB}, respectively. The *relative CT ratio* is define as

$$n_{CTA/B} = \frac{n_{CTA}}{n_{CTB}}. \tag{4.1}$$

4.2.1. Measurement Challenge Due to Module Gains

A problem however arises when trying to measure and calibrate the ammeter at the ppm level. When the first time, the primary current I_1 is applied simultaneously to both CTs, the measured secondary currents depend not only on the CT ratios but also on the gains of the measurement modules. If we denote the gains of the two ammeter channels (or modules) as g_{mod1} and g_{mod2}, then the measured secondary currents are given by

$$I_{CTA,1} = I_1 \cdot n_{CTA} \cdot g_{mod1}, \tag{4.2}$$

$$I_{CTB,1} = I_1 \cdot n_{CTB} \cdot g_{mod2}. \tag{4.3}$$

Thus, when measured the first time, the ratio is

$$n_{CTA/B,1} = \frac{I_{CTA,1}}{I_{CTB,1}} = \frac{n_{CTA} \cdot g_{mod1}}{n_{CTB} \cdot g_{mod2}}. \tag{4.4}$$

Since g_{mod1} and g_{mod2} are unknown and non-unity gains (as demonstrated in Section A.4), one cannot directly extract $n_{CTA/B}$ from $n_{CTA/B,1}$ without extra effort, such as very precisely determining the gains of the modules at every frequency, temperature, current, and other unknown factors.

4.2.2. Module Interchanging Approach

An alternative method to eliminate the effect of the unknown module gains is to interchange the connections between the CTs and the measurement modules after the first measurement. After interchanging, CTA is connected to module 2 and CTB to module 1. The second time, a primary current I_2 is applied (which is approximately equal to I_1; any discrepancy of only a few percent is acceptable due to the high linearity and time consistency of the system as demonstrated in Section A.9), the measured currents become

$$I_{CTA,2} = I_2 \cdot n_{CTA} \cdot g_{mod2}, \tag{4.5}$$

$$I_{CTB,2} = I_2 \cdot n_{CTB} \cdot g_{mod1}. \tag{4.6}$$

Hence, the second measured ratio after interchanging is

$$n_{CTA/B,2} = \frac{I_{CTA,2}}{I_{CTB,2}} = \frac{n_{CTA} \cdot g_{mod2}}{n_{CTB} \cdot g_{mod1}}. \tag{4.7}$$

4.2.3. Determination of the Relative CT Ratio

The two measured ratios $n_{CTA/B,1}$ and $n_{CTA/B,2}$ include the unknown module gains in reciprocal form. By taking the geometric mean of these two measurements, the influence of the module gains cancels out:

$$n_{CTA/B} = \sqrt{n_{CTA/B,1} \cdot n_{CTA/B,2}} = \sqrt{\frac{n_{CTA} \cdot g_{mod1}}{n_{CTB} \cdot g_{mod2}} \cdot \frac{n_{CTA} \cdot g_{mod2}}{n_{CTB} \cdot g_{mod1}}} = \frac{n_{CTA}}{n_{CTB}}. \tag{4.8}$$

In practice, this approach simplifies the calibration procedure significantly: the relative CT ratio $n_{CTA/B}$ can be obtained directly from the measured ratios before and after interchanging, without needing to characterize the individual module gains.

Sampled-Signal Parameter Estimation Algorithm

Accurate estimation of amplitude and phase for sampled sinusoidal signals is fundamental to CT ratio measurements. Achieving this requires careful measurement practices, including the use of a sampling frequency that is an integer multiple of the test signal frequency, removal of DC offsets, and acquisition of sufficiently long data samples to maximize frequency resolution.

The most straightforward method is to compute the Fast Fourier Transform (FFT) of the sampled data and extract the amplitude from the frequency bin with the largest magnitude. However, this approach is only accurate when the signal frequency aligns exactly with a discrete FFT bin. In practical scenarios, this is seldom the case, resulting in spectral leakage, where signal energy spreads into adjacent bins, thereby distorting amplitude and phase estimates.

While it is true that for ratio measurements between two nearly identical signals, certain systematic amplitude errors may partially cancel, the basic FFT approach does not provide reliable absolute amplitude information. As a result, this method is insufficient for high-accuracy applications and does not allow for rigorous verification of the measurement system's performance.

To address spectral leakage, signal resampling can be applied to realign the frequency content to discrete FFT bins. However, resampling algorithms are computationally demanding, and can thus not be applied in real time. An investigation on resampling algorithms and their performance for this application was done in Appendix B. Instead, this thesis employs the interpolated Discrete Fourier Transform technique, specifically the three-point interpolated Hanning-window DFT method (`idft3phann`), following the approach described in [66] and adapted from [67]. This method allows for the accurate estimation of frequency, amplitude, and phase even when the signal frequency does not coincide with an integer FFT bin, while being at least 2 orders of magnitude more computationally efficient than the resampling method.

5.1. Implementation Procedure

The estimation and ratio calculation procedure comprises the following steps:

1. Each channel's time-series data is segmented into fixed-duration windows (0.04 s); for a 1 s acquisition, this results in 25 segments per channel.

2. A Hanning window (in Figure 5.1b) is applied to each segment to reduce spectral leakage. The Hanning window is selected for its favourable balance between main-lobe width and side-lobe attenuation (approximately -31.5 dB). The first half of the windowed signal is shown in Figure 5.1a.

3. The FFT is computed for each windowed segment, and the frequency bin with the highest magnitude (peak bin) is identified.

4. The magnitudes of bins directly adjacent to the peak bin are used to estimate the frequency offset from the centre of the peak bin, based on the side-bin amplitudes. This parameter is essentially estimating how far left or right from the peak bin the true fundamental frequency is.

5. Using the estimated offset and side-bin values, a three-point interpolation method is applied to estimate the true signal parameters: frequency, amplitude, phase, and DC offset.

6. For each segment, the amplitude and phase ratio between the two channels is calculated, following the procedure in Subsection 4.2.

7. The resulting ratios are averaged across all segments to yield the mean and standard deviation for the measurement.

(a) Ramp-up part of the windowed vs. raw waveform

(b) Hanning window shape

(c) Amplitude spectrum without window

(d) Amplitude spectrum with Hanning window
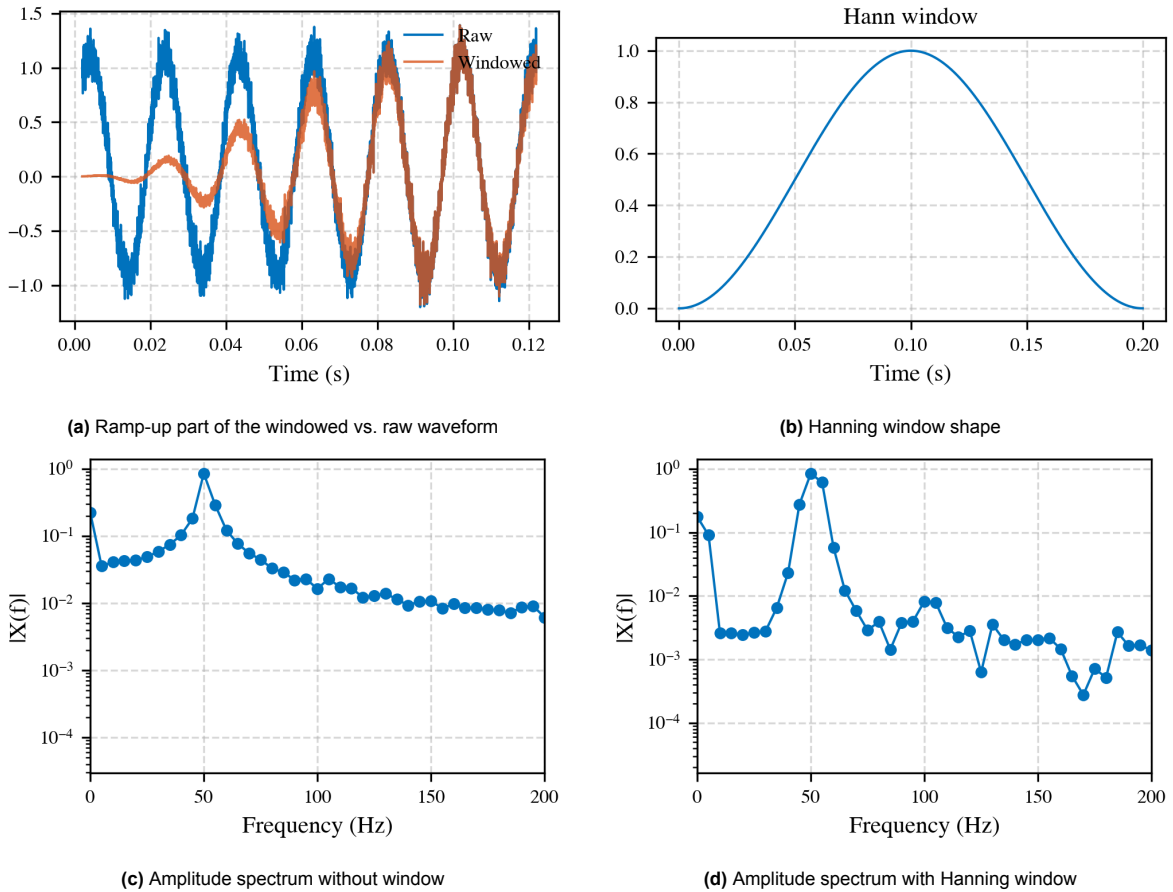
Figure 5.1: Time- and frequency-domain effects of windowing. Figures 5.1a and 5.1b show the tapered record and it's window; Figures 5.1c and 5.1d illustrate the decreased spectral leakage (how high the signal peak is compared to the rest of spectrum), but also illustrate main-lobe broadening (how wide the peak is), thus the need to interpolate the side-lobe energy to recover an accurate amplitude estimation.

The procedure adds only a few arithmetic operations to the FFT yet improves frequency resolution by two orders of magnitude.

5.2. Simulation Study

A numerical simulation was performed to demonstrate the advantage of the `idft3phann` algorithm for parameter estimation in noisy environments. In this simulation, a cosine signal with frequency f = 51.3 Hz, amplitude = 1, phase = 0.2 rad, and DC offset = 0.1 was sampled at F_s = 8 kHz for 1 s. Significant noise was intentionally added: both 50 Hz and 100 Hz harmonic noise at 5% of the signal amplitude, and Gaussian noise at 10%.

Figure 5.2 (left) compares the original and noisy signals, as well as the reconstructed signals from both

the traditional FFT and the proposed `idft3phann` method. The results show the `idft3phann` method accurately recovers the signal parameters even under heavy noise, whereas the FFT approach suffers from significant leakage and inaccuracy.

Table 5.1 summarizes the parameter-estimation accuracy for each method.
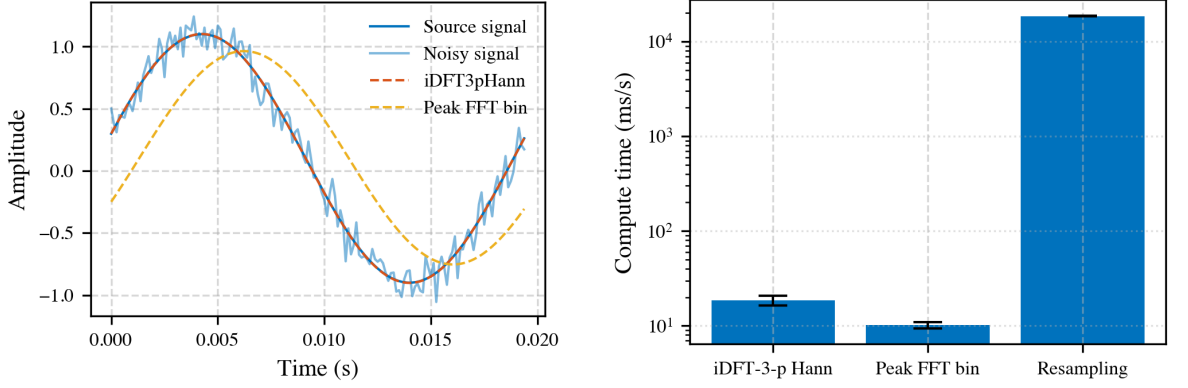
(a) Parameter estimation performance: original, noisy, FFT, and `idft3phann` reconstructed signals.

(b) Computation time per algorithm for processing 1 s of 1 MHz data. The resampling method is about 1000 times slower than `idft3phann` [1].

Figure 5.2: Left: Signal parameter recovery in noise (see Table 5.1 for quantitative results). Right: Relative computation time for common amplitude estimation algorithms.

Table 5.1: Parameter estimation results for the simulated test signal using different algorithms.

Method	$\hat{f}$ (Hz)	$\hat{A}$	$\hat{\phi}$ (rad)	$\hat{DC}$
True value	51.3000	1.0000	0.2000	0.1000
Peak FFT bin	51.0000	0.8617	-0.4240	0.1054
iDFT3pHann (proposed)	51.3001	1.0003	0.1981	0.1002

The interpolated method (`idft3phann`) recovers parameters with errors less than 1×10^{-4} Hz in frequency, 0.03% in amplitude, and 0.002 rad in phase, significantly outperforming the FFT method under noisy conditions. In addition, while the commonly used resampling algorithm requires about 18 s per 1 s of measurement data on the used computer, the `idft3phann` method processes the same data in approximately 17 ms; fast enough for real-time use. The FFT method is fastest, at 10 ms, but does not deliver the same estimation accuracy in non-ideal conditions. It should be noted that this comparison reflects a conservative scenario; noise levels encountered in practical measurements are expected to be substantially lower, potentially reducing the performance gap between these algorithms.

---

[1]Average of 10 runs. Benchmarked on Apple M1 MacBook Pro. While computation times will vary with hardware, the relative differences between algorithms should remain similar.

Part III
Experimental Results

6

Baseline Set-up Measurement Results

This chapter presents the results obtained with the baseline measurement setup, which serves as a reference for all subsequent analyses in this thesis. The aim is to establish a robust and repeatable foundation for evaluating the performance of current transformers across the 50 Hz to 150 kHz frequency range.

6.1. Secondary-to-Secondary Current Ratio: Baseline Results

The reference measurement for this research is the direct comparison of the secondary currents of the device under test (CT A) and the reference CT (CT B). This measurement reveals how similarly two almost identical, electronically compensated CTs behave when subjected to the same primary current. Such a comparison is particularly important for detecting frequency-dependent differences and for quantifying the influence of any introduced experimental effects in later chapters.

Figure 6.1 summarizes the amplitude ratio (left) and the same data on a symmetric logarithmic (symlog) scale (right) between $I_{s,CTA}$ and $I_{s,CTB}$ across the frequency range of interest. [1] The plot demonstrates the near-perfect agreement of both CTs at frequencies below 5 kHz, within the stated measurement uncertainty limits.
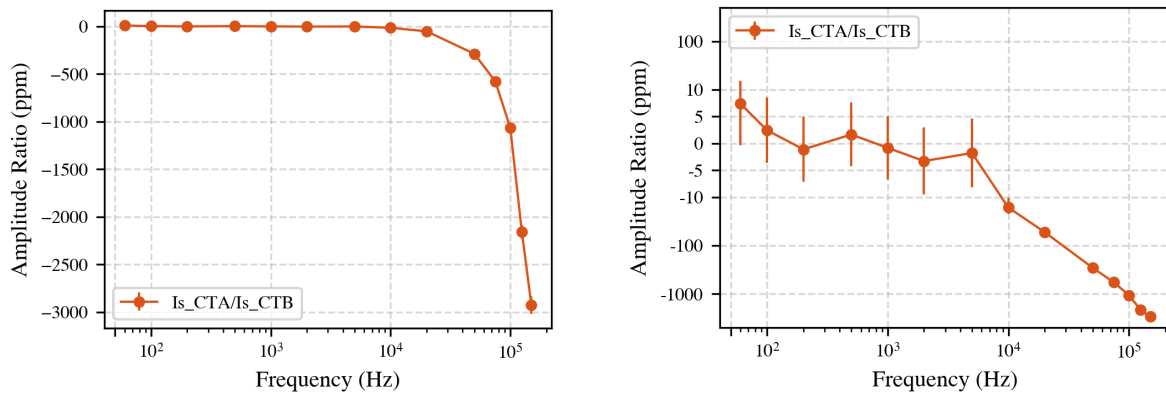
Figure 6.1: Left: Relative ratio between secondary currents of CT A and CT B. Deviations increase above 5 kHz, up to approximately 3000 ppm at 150 kHz. Right: The same data plotted on a symlog scale highlights the near-identical performance below 5 kHz (within measurement uncertainty).

At frequencies below 5 kHz, the difference between the two CTs is negligible, remaining well within the measurement uncertainty. However, at higher frequencies, especially above 20 kHz, differences

---

[1]A symlog scale combines linear scaling from –10 to 10 with logarithmic scaling for the rest. This approach allows visualization of data spanning multiple orders of magnitude while clearly displaying small deviations around zero.

become increasingly pronounced. These deviations, reaching up to 3000 ppm at 150 kHz.

The phase relationship between the two CTs' secondary currents is shown in Figure 6.2, confirming that the phase error also grows with frequency.

Figure 6.2: Measured phase difference between secondary currents of CT A and CT B, demonstrating near-0 phase error at low frequencies and increasing deviations above 10 kHz.

These secondary-to-secondary measurements form the essential baseline for this thesis. In subsequent chapters, various controlled changes will be introduced to CT A—such as modifications to cabling, grounding, or external influences. The impact of these changes will be assessed by comparing the altered se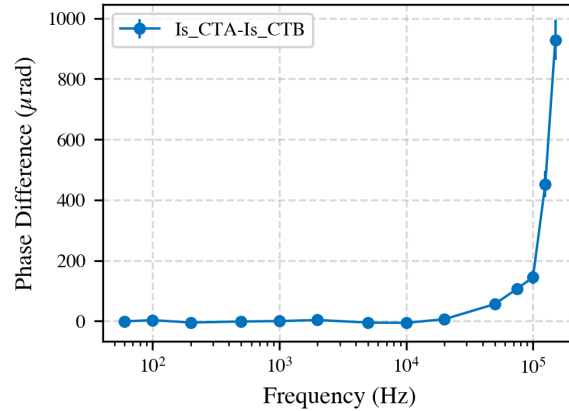condary-to-secondary ratios to the baseline results presented here. This methodology enables sensitive detection of small influences on CT performance, without requiring absolute primary current measurements.

6.2. Primary-to-Secondary Current Ratio: Absolute Reference

For completeness, the direct ratio between the measured primary current I_p and the secondary currents $I_{s,CTA}$ and $I_{s,CTB}$ was also evaluated. This primary-to-secondary comparison provides an absolute reference for CT ratio performance and is important for quantifying any systematic errors that might be missed by relative measurements.
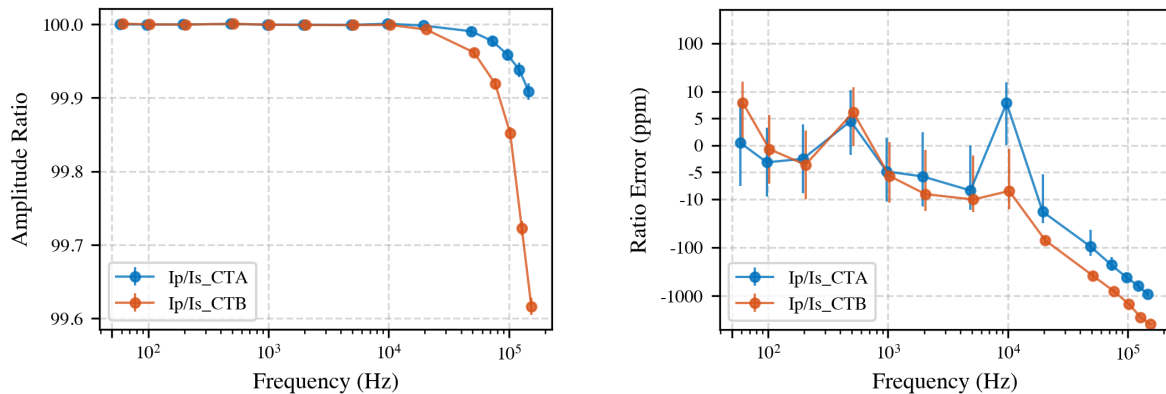
Figure 6.3: Left: Measured primary-to-secondary current ratios for CT A and CT B across the full frequency range. Right: The same data plotted on a symlog scale.

Both CTs ratio is near 100:1 below 10 kHz, with deviations increasing at higher frequencies.

Phase differences between the primary and secondary currents are presented in Figure 6.4, which provides additional context for understanding the CTs' frequency-dependent behaviour.
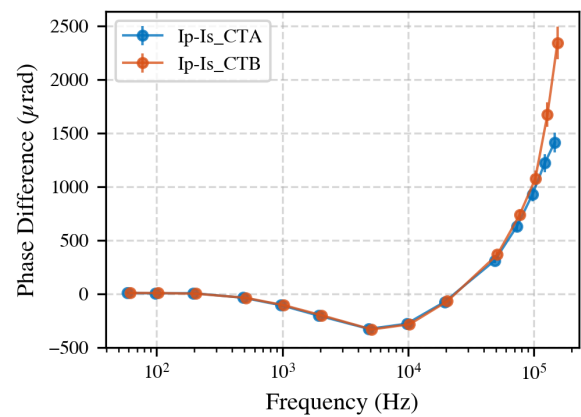
Figure 6.4: Measured phase difference between primary current I_p and secondary currents $I_{s,CTA}$ and $I_{s,CTB}$. Smaller phase differences correspond to more ideal frequency responses.

7

Time-Dependent Behaviour Characterisation

Current transformer ratio measurements in this set-up require management of three key time-dependent factors:

1. Thermal Stabilisation: Primarily concerning the sampling ammeter current measurement modules. Adequate warm-up is necessary to minimise drift in the measurement electronics.

2. Statistical Convergence: The exposure (sampling) time needed for the measurement standard deviation to decrease below a defined parts-per-million (ppm) target.

3. Intra-day Stability: Even with a daily reference measurement, factors such as powering down the system, reconnecting cables, or slight repositioning of the CTs, and other unknown factors, can introduce additional variability. By fully disassembling and reassembling the setup five consecutive times and recording the measurements, the repeatability and short-term stability of the system can be quantified.

This chapter addresses these topics.

7.1. Sampling ammeter Warm-Up

During measurement campaigns, a 10 A primary current is applied to the CTs, resulting in a secondary current of approximately 100 mA (for a 100 : 1 ratio). As described in Chapter 4, both CTs are measured in parallel, and their ratio is used as the primary evaluation metric. To ensure that time-dependent errors are minimised, the ammeter itself must be thermally stable. Any temporal drift in the ammeter, particularly between current channels, undermines the effectiveness of error-cancellation methods such as the channel-swapping technique outlined in Section 4.2.

To assess ammeter stability, the instrument was operated continuously with a fixed current for 60 min, while monitoring the measured current ratios at 150 kHz. Since it is impossible to know which shunt is drifting and which one is stable, and thus what the true current is, the focus is placed on the stability of ratios between shunts, which directly affects measurement repeatability.

The time-evolution of the ratio can be described by a first-order exponential model:

$$R(t) = R_{final} + \Delta R \left(1 - e^{-t/\tau}\right) \qquad (7.1)$$

where:

- $R(t)$ is the measured ratio at time t,
- R_{final} is the final, steady-state ratio,

- ΔR is the total drift amplitude (in ppm),
- τ is the thermal time constant (in seconds),
- t is the elapsed time since power-on.

At 150 kHz, fitted values were ΔR = –10.2 ppm and τ = 763 s, meaning that after approximately 27 min, the residual drift (future expected drift) is less than 1 ppm. Figure 7.1 displays this model fit overlaid on the observed ratio drift.
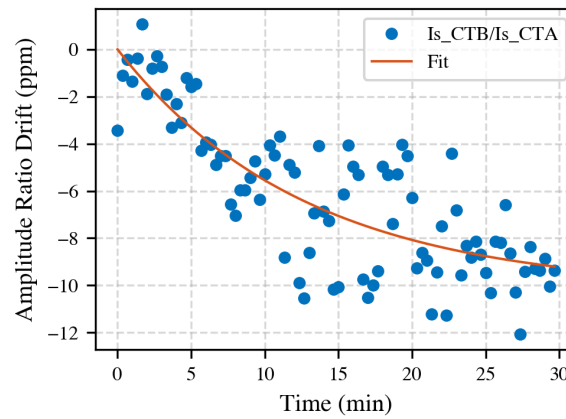
Figure 7.1: Measured residual[1] drift (blue) and fitted heating model (orange) for the CTB:I_p ratio at 150 kHz, with drift amplitude of 10.2 ppm and a thermal time constant of 763 s.

This warm-up experiment was repeated at 50 Hz and 50 kHz, and the resulting drift amplitudes and time constants are compared in Figure 7.2. The results show that higher frequencies lead to greater temperature-induced drift.
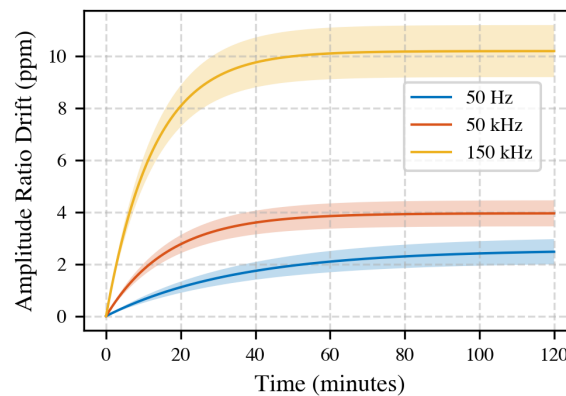
Figure 7.2: Comparison of measured thermal drift curves for the ammeter at three different frequencies. Drift amplitude increases with frequency, requiring longer warm-up for high-frequency measurements.

For all subsequent testing, a standard 30 min warm-up period was adopted, limiting the drift between the two identical type secondary side current measurement shunts inside the ammeter to less than 1 ppm.

7.2. Averaging Time for Target Measurement Standard Deviation

When measuring the ratio between the two CTs, there is some inherent fluctuations and noise. By increasing the sampling duration, the measurement standard deviation can be reduced.

The required number of samples n for a target accuracy can be calculated as:

$$n = \left(\frac{z \cdot \sigma}{E}\right)^2 \qquad (7.2)$$

where:

- n = required number of samples,
- z = standard normal value for the confidence level (2 for 95%),
- σ = standard deviation of the ratio,
- E = desired error bound (in ppm or absolute units).

Figure 7.3 summarizes the required measurement duration (in minutes) to achieve a 1 ppm standard deviation across frequencies. The time required increases with frequency, limiting the achievable uncertainty at higher frequencies for practical measurement durations.
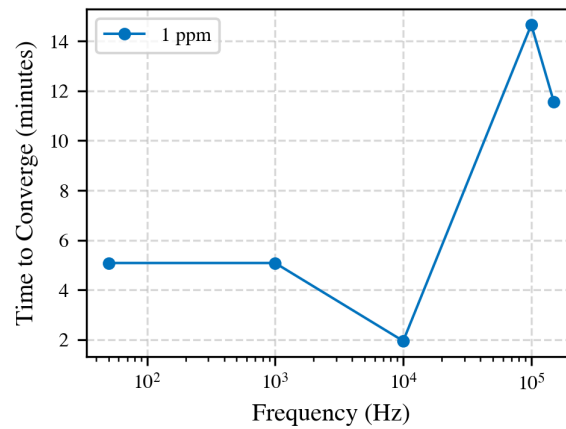
Figure 7.3: Measurement duration (minutes) required to reach 1 ppm standard deviation as a function of fundamental frequency.

To confirm the statistical nature of the noise, the Allan deviation $\sigma_A(\tau)$ is computed as a function of averaging time τ. As shown in Figure 7.4, the observed $\tau^{-1/2}$ trend demonstrates white (memoryless) noise, confirming that uncertainty decreases with longer measurement times.
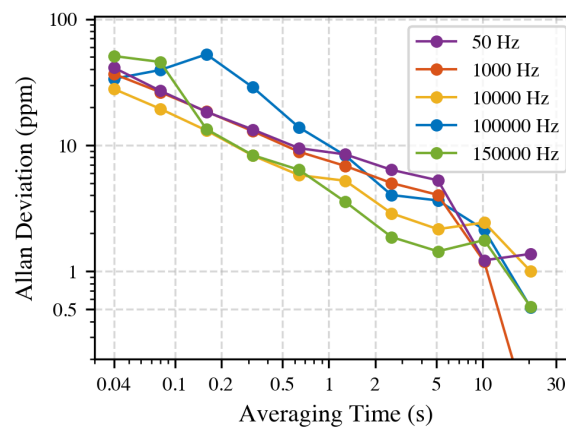
Figure 7.4: Allan deviation of the CT ratio as a function of averaging time for three different frequencies. The $\tau^{-1/2}$ slope confirms white noise dominance, justifying simple time averaging.

7.3. Repeatability of the Complete Test Cycle

Daily reference measurements are essential for verifying that the measurement system remains stable and free from long-term drift. However, for practical purposes, it is also important to quantify short-term (within-day) repeatability. To this end, the full test procedure: including cable reconnections, power cycling, 30 min warm-up, and 10 s data acquisition at the 14 predefined frequencies with 10 A primary current, was performed five times. Each cycle was separated by a 20 min pause, simulating typical reconfiguration scenarios. After each run, the residual ratio (the deviation from the mean across runs) was computed, and the standard deviation across runs was used to quantify repeatability.

Residual Ratio Across Test Cycles

Figure 7.5 displays the residual ratio, defined as:

$$\Delta R(f) = \left. \frac{I_{CTA}}{I_{CTB}} \right|_{run} \left\langle \frac{I_{CTA}}{I_{CTB}} \right\rangle_{all\ runs} \tag{7.3}$$

For frequencies up to 20 kHz, the spread remains within a few ppm; above this, the variation increases.
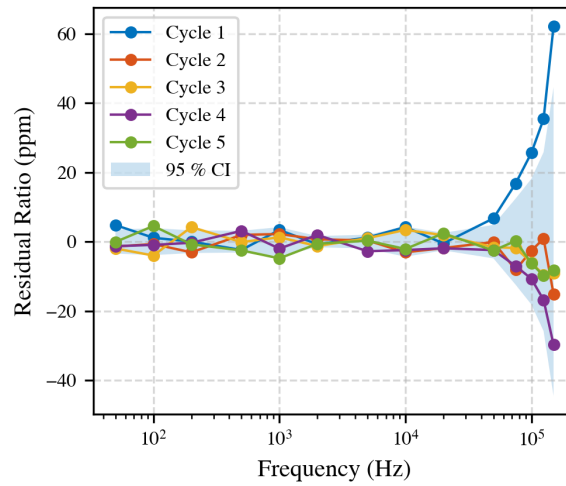
Figure 7.5: Residual CT ratio across five independent runs. Repeatability is better than ± 5 ppm below 20 kHz, and degrades at higher frequencies.

7.3.1. Relationship Between Ratio Magnitude and Standard Deviation

The relationship between the observed ratio and its standard deviation is shown in Figure 7.6. Here, the standard deviation σ (for each 10 s measurement) is plotted against the ratio amplitude. A possible trend emerges: as the CT ratio deviates more from unity, the random variation increases.

A linear fit to the data yields:

$$\hat{\sigma}_{10s}\ [ppm] = (1.91 \pm 0.06) + (1.03 \pm 0.04) \times 10^{-2} A_{ratio}, \qquad R^2 = 0.974, \tag{7.4}$$

where A_{ratio} is the secondary-to-secondary amplitude ratio deviation in ppm. The intercept represents the minimum uncertainty limit set by the 10 s acquisition, while the slope captures the additional variability induced by larger ratio deviations.
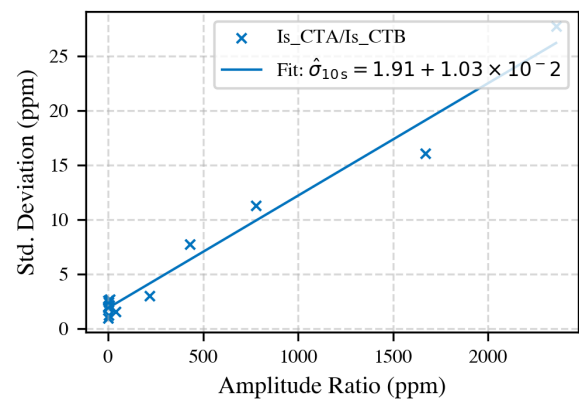
Figure 7.6: Sample standard deviation ($\sigma_{10\,s}$ trace) versus CT-to-CT ratio amplitude. The solid line is the least-squares fit as per Eq. (7.4).

8

Component Configuration Characterization

Accurate characterization of current transformer performance depends not only on the transformers themselves but also on the configuration of measurement system components. This chapter examines how variations in secondary-side cabling, grounding practices, shunt resistor selection, compensation electronics, primary conductor positioning, and CT mutual proximity influence the accuracy and stability of ratio and phase measurements in broadband CT calibration.

Practical calibration setups in industry and laboratory environments are subject to variations in cable routing, component selection, and physical arrangement. Quantifying the sensitivity of the measurement system to these factors ensures that calibration results are robust and repeatable under different conditions.

The sections that follow present experimental studies of each configuration parameter. For each case, the underlying theory is outlined, relevant electrical parameters are measured across the frequency range of interest, and the impact on CT ratio and phase measurements is quantified. The goal is to provide guidance and insight into the construction of such a CT ratio measurement set-up, enabling accurate calibration while minimizing unnecessary setup complexity.

8.1. Cable Characterization

This section evaluates the electrical characteristics of cables connecting the secondary side of the current transformer to the ammeter. Cable selection impacts measurement accuracy due to its inherent series impedance, comprising series resistance (R), series inductive reactance (X_L), and potentially parallel parasitic capacitance depending on cable type. Figure 8.1 shows a simplified equivalent circuit of the measurement system.
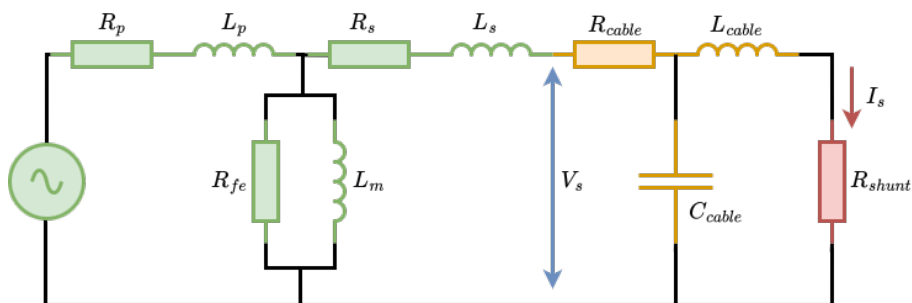

Figure 8.1: Equivalent circuit of the cable measurement setup. The CT secondary winding (green) connects via the test cable (orange) to the internal shunt resistor internal to the ammeter (red). Voltage across the ammeter shunt is used for secondary current (I_s) measurement. Cable parameters are determined by measuring the voltage (V_s, blue) at the CT output terminals.

Cable impedance (Z_{cable}) was experimentally measured by simultaneously capturing the amplitude and phase of voltage V_s and current I_s. Measurements were performed across a frequency range from 50 Hz to 150 kHz. Using phasor representation, impedance components were calculated as follows:

$$Z_{cable} = \frac{V}{I} \implies R = Re(Z_{cable}), \quad X_L = Im(Z_{cable}) \tag{8.1}$$

At high frequencies, current transformers are particularly sensitive to excessive secondary impedances. The CT generates the necessary secondary current to achieve its desired current ratio. From Figure 8.1 it can observed that, the secondary impedance influences drives the CTs to generate a voltage across the magnetizing inductance (L_m) and core losses (R_{fe}), causing increased leakage current through these parallel paths.

8.1.1. Twisted-Pair Cable Performance
Twisted-pair cables are a possible contender for their magnetic interference resistant properties, achieved through twisting and close conductor spacing, effectively cancelling external electromagnetic interference. However, these cables do still exhibit inductance.

Measurements of inductive reactance (X_L) at 150 kHz were performed for twisted-pair cable lengths of 50 cm, 100 cm, and 190 cm (Table 8.1). To isolate cable inductance from other circuit components, a linear regression was applied, resulting in a slope of 0.74 Ω/m, an intercept of 0.1430 Ω, and R^2 = 0.99. These were converted into inductance values (L) by applying the relationship $X_L = 2\pi fL$. These parameters indicate an inductance of approximately 0.78 µH/m for the cable, with an additional inductance of 0.15 µH attributed to circuit components other than the cable.

Table 8.1: Measured inductive reactance of twisted-pair cables at 150 kHz

Cable Length (cm)	Reactance X_L (Ω)
50	0.52
100	0.88
190	1.56
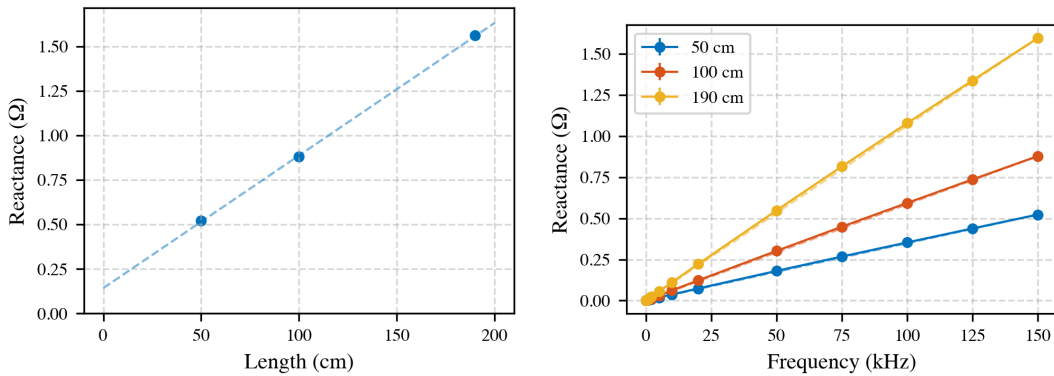
Figure 8.2: Left: Linear relationship between cable length and reactance at 150 kHz, indicating a cable inductance of 0.78 µH/m. Right: Reactance (X_L) versus frequency for various cable lengths. Due to $X_L = 2\pi fL$, with a linear increase in frequency there is a linear increase in reactance. This shows there is nearly ideal inductive behaviour, with inductance proportional to cable length

Resistance measurements of the cables at 50 Hz were similarly obtained by subtracting the internal ammeter shunt resistance of (0.110 Ω) from total measured resistance. Linear regression yielded a slope of 0.04 Ω/m, an intercept of 0.1179 Ω, and R^2 = 0.99. The intercept is essential the resistance that can not be attributed to the cables, and it closely matches the known internal shunt resistance.

Table 8.2: Measured resistance of twisted-pair cables at 150 kHz, corrected for internal shunt (0.110 Ω)

Cable Length (cm)	Measured R_{total} (Ω)	R_{cable}(Ω)
50	0.14	0.03
100	0.16	0.05
190	0.20	0.09
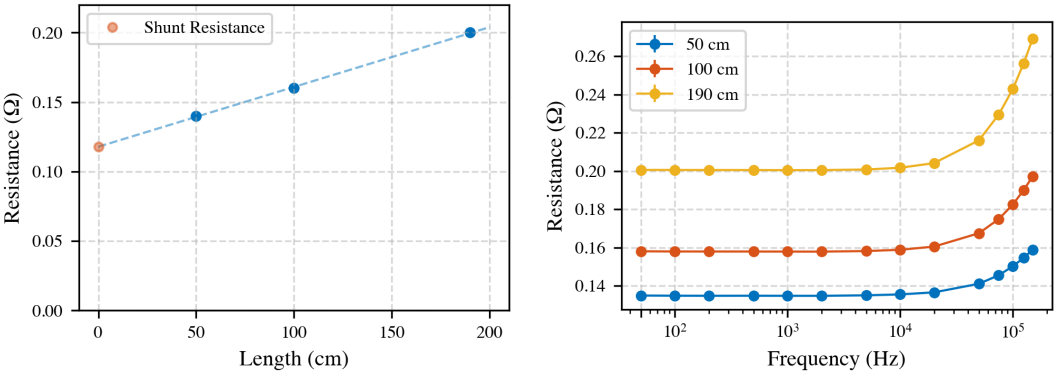
Figure 8.3: Left: Linear correlation between cable length and resistance at 50 Hz, indicating a resistance of 0.04 Ω/m and validating the other resistance is from the internal shunt of 0.11 Ω. Right: Frequency-dependent resistance highlighting increased resistance proportional to cable length. Note that high-frequency effects (skin and proximity) can increase the observed R compared to the 50 Hz value.

8.1.2. Coaxial Cable Performance

Coaxial cables are an alternative, and are frequently employed in applications requiring shielding, precise impedance control, and reduced noise susceptibility. In comparison to twisted-pair cables, coaxial cables exhibit slightly lower inductance (0.68 µH m^{-1} versus approximately 1.05 µH m^{-1}), yet have higher resistive losses, in this scenario more than twice those observed in twisted-pair cables for equivalent lengths.
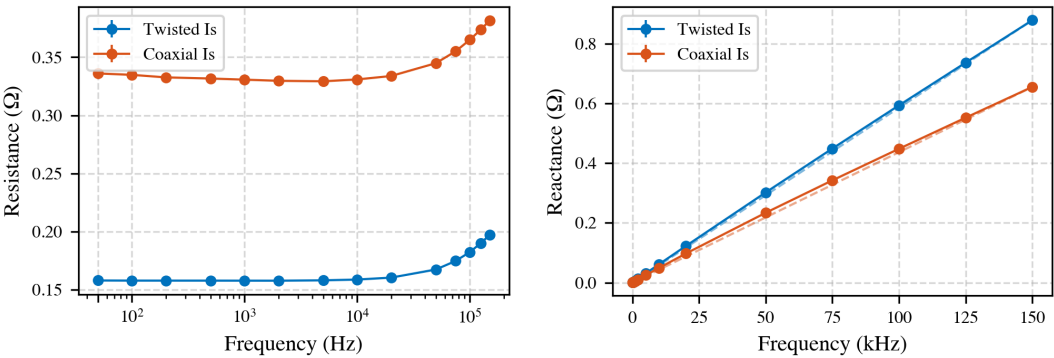
Figure 8.4: Left: Resistance of a 100 cm coaxial cable compared to a 100 cm twisted-pair cable. The coaxial cable can be observed to have a significantly higher resistance. Right: Measured inductive reactance (X_L). Frequency is plotted on a linear scale, demonstrating the linear behaviour characteristic of purely inductive components. The coaxial cable exhibits slightly lower inductance compared to the twisted-pair cable.

Additionally, coaxial cables inherently include higher parallel capacitance (typically tens to hundreds of pF m^{-1}), which was not explicitly measured in this investigation. This capacitance, however, poses a notable risk: at higher frequencies, capacitive coupling allows current to bypass the ammeter's shunt resistor, thus decreasing the accuracy of the current measurement.

In applications prioritizing minimal inductance, coaxial cable may offer slight advantages over twisted-pair. However, increased resistance and parasitic capacitance add to the uncertainty. These factors

must be carefully evaluated, especially considering many CT's limited capability to generate secondary voltages without sacrificing measurement accuracy.

8.2. Grounding and Earth-Loop Effects

Although both the sampling ammeter (power analyser) and the current transformers are designed for floating operation, with optical isolation between ammeter measurement shunt and digitizer, and the rest of the power analyser, and galvanic isolation between CT secondary and primary windings, small but finite parasitic capacitances exist between internal circuits and instrument chassis. When protective earth (PE) connections tie CT casings and the ammeter enclosure together, these capacitances (C_{stray}) create closed-loop paths, possibly enabling unintended earth-loop currents (I_E) to flow. In addition, leakage currents from CT compensation electronics referenced to PE may also contribute. Figure 8.5 summarizes the two main earth-loop current paths identified:

1. Capacitive coupling between internal circuit nodes and grounded enclosures.

2. Leakage currents from compensation electronics referenced to PE.
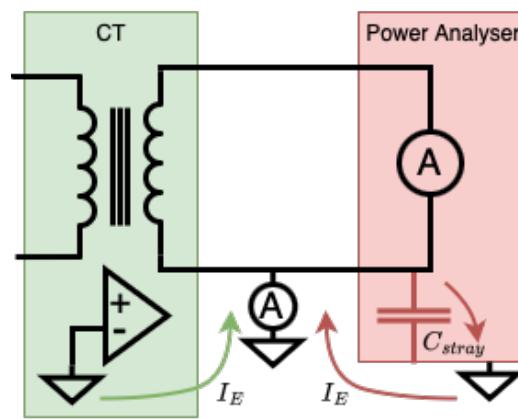
Figure 8.5: Equivalent diagram of potential earth-loop paths in the measurement setup. While CT secondary conductors (green) and the ammeter shunt (red) are ideally isolated, stray capacitances C_{stray} and leakage through compensation electronics may create unintended current paths to protective earth (PE). These currents can superimpose on measured secondary currents and bias CT ratio measurements.

8.2.1. Measured Earth-Loop Currents

By placing a 110 mΩ shunt in series with the ground connection of the secondary side, it is possible to directly measure the earth current. This reveals two distinct categories of earth-loop currents in the system. The first category consists of broad-spectrum currents centred near 52 kHz, appearing in both time and frequency domains even when the excitation frequency is much lower (e.g., at 50 Hz). As depicted in Figure 8.6, the RMS value of this broadband earth-loop current is approximately 680 µA, with spectral components appearing and disappearing during the 10 s measurement window.

(a) Time-domain waveform of earth-loop current at 50 Hz.

(b) FFT of the same record; note broadband components near 52 kHz.
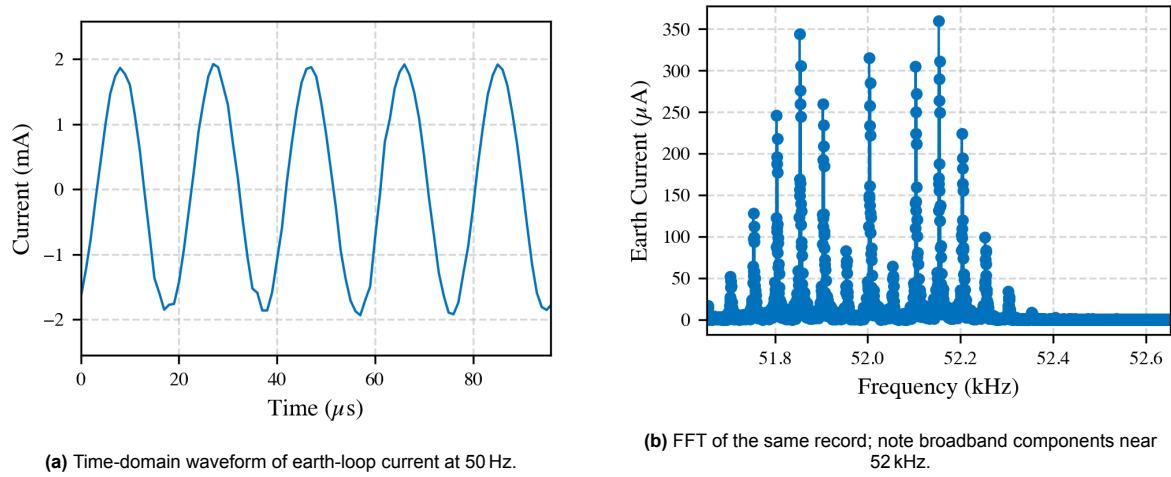
Figure 8.6: Earth-loop current (I_E) during a 50 Hz excitation. The broadband spectral content complicates high-frequency measurements when PE is connected.

At higher excitation frequencies (e.g., 150 kHz), the RMS magnitude of the earth-loop current remains comparable (680 µA$_{rms}$).

A second, distinct group of earth-loop currents is observed at the primary excitation frequency itself, only observed at 50 Hz and 100 Hz. Unlike the broad-spectrum earth-loop currents that dominate at higher frequencies, these low-frequency currents exhibit a much smaller amplitude, on the order of 0.4 µA at 50 Hz and 0.7 µA at 100 Hz. Figure 8.7 presents the frequency-domain measurements of these earth-loop currents for both excitation frequencies.
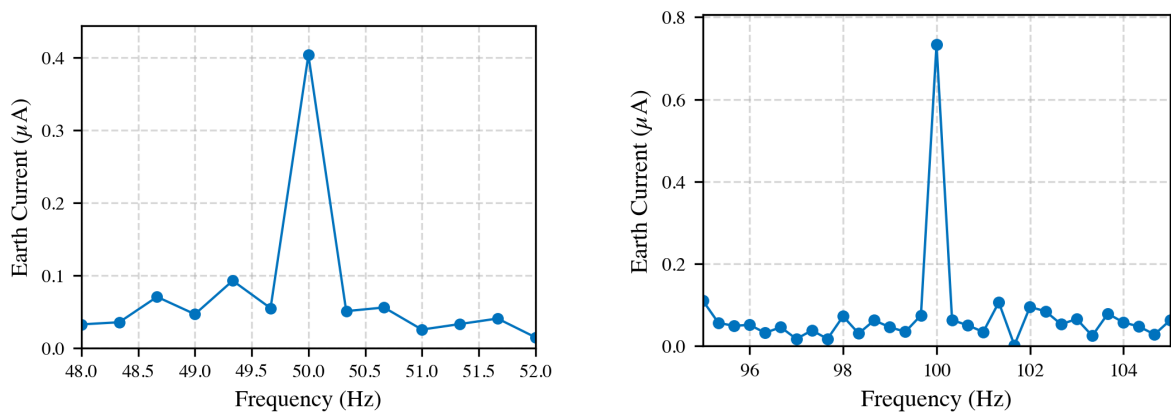
Figure 8.7: Frequency-domain analysis of earth-loop currents at primary excitation frequencies. Left: 50 Hz (0.4 µA). Right: 100 Hz (0.7 µA). These measurements reveal the presence of earth-loop current directly at the excitation frequency, while such currents are not detectable at higher frequencies.

These low-frequency earth-loop currents are of particular concern for several reasons. First, even though their absolute magnitudes are small relative to the secondary current (for example, 0.4 µA compared to a typical secondary current of 100 mA), their direct appearance at the fundamental measurement frequency means that they can bypass the intended shunt resistance of the ammeter. This can lead to a systematic bias in the calculated CT ratio, on the order of a few ppm at 50 Hz, which is a significant portion of the total uncertainty of 10 ppm at these frequencies.

It is important to note that these excitation-frequency earth-loop currents were reliably detected only up to 100 Hz. At higher primary frequencies, the amplitude of these currents falls below the detection threshold of the measurement setup. It is important to note that for the uncertainty budget, a con-

servative estimate has to be made. Except for 50 Hz and 100 Hz, the noise floor of the earth current measurement at each frequency is chosen as the uncertainty contribution.

8.2.2. Impact on Ratio Measurements

To directly assess the influence of grounding on measurement accuracy, CTA is ungrounded, and CTB is grounded, then the current ratio measurements were compared for both grounded and ungrounded secondary-side configurations. Figure 8.8 summarizes these results.

At most frequencies, the effect of grounding on both the primary-to-secondary ratio (left) and the secondary-to-secondary ratio (right) remains within the expanded measurement uncertainty. However, at 50 Hz and 100 Hz, a small but statistically significant shift of about 4 ppm was observed in the primary-to-secondary ratio, matching the magnitude of the measured earth-loop current (0.4 µA relative to a 100 mA secondary current). This bias demonstrates that at low frequencies, earth-loop effects can reach a level that is non-negligible for high-accuracy calibration.

(a) Primary-to-secondary current ratio of CTA in grounded and ungrounded configurations.

(b) CTA to CTB secondary current ratio, showing negligible difference.

Figure 8.8: Ratio measurements comparing the impact of grounding the CT secondary side. Differences remain within measurement uncertainty, except for a small but measurable impact at 50 Hz and 100 Hz.

8.2.3. Mitigation Strategy

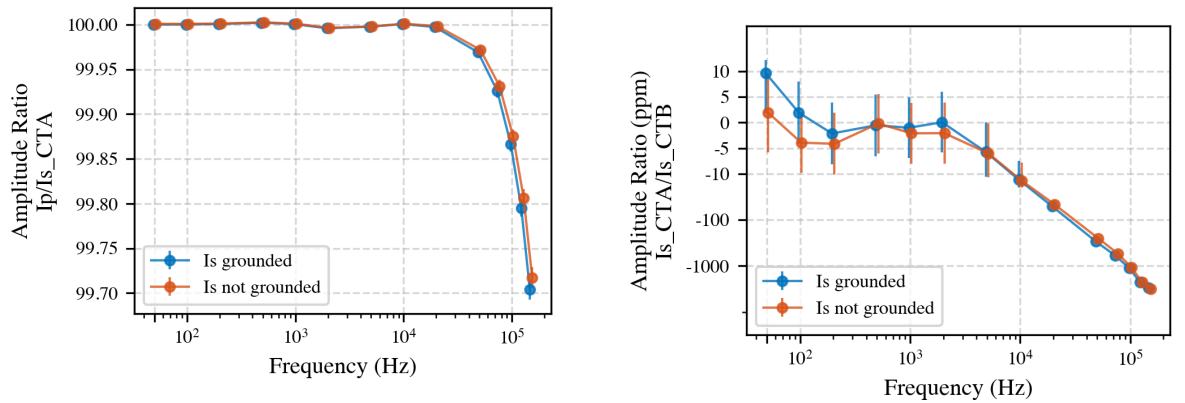While disconnecting all earth connections would eliminate earth-loop currents, this approach compromises both operational safety and measurement repeatability—particularly for field or different laboratory calibrations. Therefore, a single-point grounding configuration was implemented, in which all CT secondary circuits, the ammeter enclosure, and all shielding are bonded at a single star point, located at the ammeter (see Figure 4.2).

This approach confines earth-loop currents to predictable paths. The dominant earth-loop current component (52 kHz) remains spectrally separated from the measurement frequencies of interest. The observed impact on high-frequency ratio measurements is below the stated expanded measurement uncertainty, as detailed in Section C.2.

However, at 50 Hz, it may be advisable to temporarily disconnect the secondary ground to achieve the highest possible accuracy; provided this can be done safely and without magnetic pick-up from nearby components.

8.3. Selection of Ammeter Internal Shunts

To measure the primary and secondary currents, a power analyser is used with built in ammeter modules. The ammeter offers three factory-installed shunt resistors:

Module	R_{sh} (mΩ)	Nominal Range	Coverage in this work
30 A module	6.5	0–30 A	Primary current (10 A)
5 A module	110	0–5 A	Secondary current (up to 4.6 A)
0.5 A module	500	0–0.5 A	Not Used

A lower resistance shunt minimizes burden on the CT but increases the signal to noise ratio; conversely, a higher shunt increases signal magnitude yet loads the CT. Figure 8.9 compares (a) the primary-to-secondary ratio of CT A for each shunt and (b) the inter-CT ratio $I_{s\,B}/I_{s\,A}$ [1].

(a) CTA ratio error vs. frequency for all three shunts.

(b) Secondary-to-secondary current ratio (B/A) on symlog scale; 6.5 mΩ shunt shows two orders of magnitude higher standard deviation.
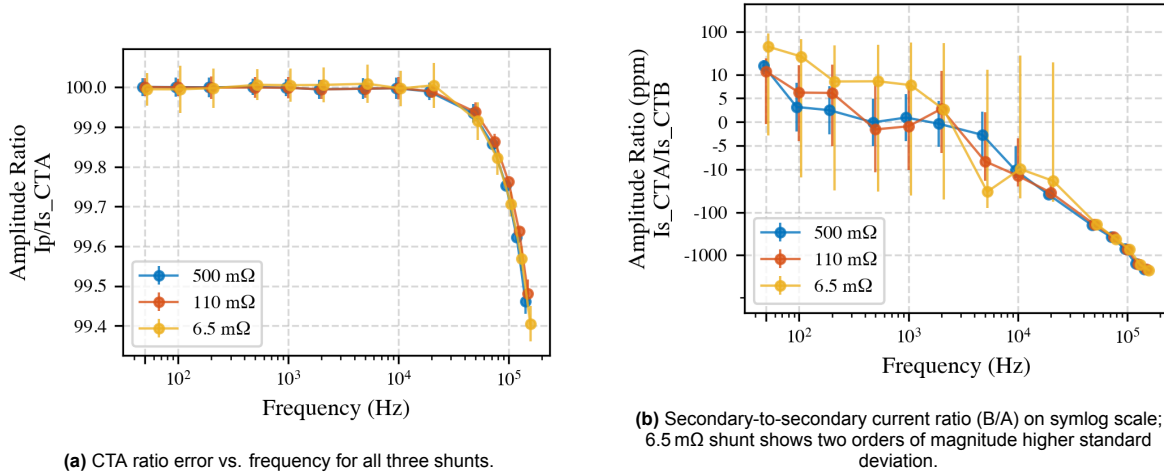
Figure 8.9: Influence of shunt selection on CT-ratio measurements. The 110 mΩ shunt provides the best compromise: it loads the CT secondary by only ∼0.5 V at 5 A, yet keeps the signal well above the ammeter's noise floor.

The 6.5 mΩ element increases the noise related standard deviation by 2 orders of magnitude at low secondary currents (< 200 mA), while the 500 mΩ loads the CTs more than standard testing protocol, and especially for non-compensated CTs leads to too high of a secondary voltage of 2.5 V. Hence the 110 mΩ shunt is adopted for all subsequent secondary-current measurements.

Quantization Noise

Quantization noise arises from the inherent resolution limitations of the analogue-to-digital converter used in the sampling ammeter. For an N-bit analogue-to-digital converter operating over a current measurement range I_R, the smallest increment in measurable current, the least significant bit, is given by:

$$q_I = \frac{I_R}{2^N} \tag{8.2}$$

where I_R is the selected full-scale range. The ammeter employed in this study uses an 18-bit delta-sigma analogue-to-digital converter (N = 18) on all current channels.

For the secondary current measurement channel, the measurement range is I_R = 500 mA, resulting in a quantization step size:

$$q_I = \frac{500 \text{ mA}}{2^{18}} \approx 1.9 \ \mu A \tag{8.3}$$

Since the maximum quantization error is half the least significant bit, the effective uncertainty is:

$$u_q = \frac{1.9 \ \mu A}{2} = 0.95 \ \mu A \tag{8.4}$$

For a typical secondary current of 100 mA, this yields a relative quantization uncertainty of:

$$\frac{0.95 \ \mu A}{100 \text{ mA}} = 9.5 \text{ ppm} \tag{8.5}$$

---

[1]This experiment was performed early in the research, and thus the low frequency behaviour of this set-up was not optimal. The figures serve as an indication rather than an absolute estimate of measurement impact when a different shunt is used.

For the primary current measurement channel, with a full-scale range of I_R = 20 A, resulting in a relative quantization uncertainty of approximately 3.8 ppm for a 10 A primary current.

These quantization errors are incorporated in the overall uncertainty budget as a rectangular distribution.

8.4. Effect of CT Compensation Electronics

Both CTs employ electronically compensated feedback that injects a correcting current to cancel core magnetization. At higher frequencies the amplifier bandwidth limits this compensation, potentially introducing ratio error. The effect was examined by repeating the primary-to-secondary measurement with the compensation circuitry disabled via the rear-panel switch.

(a) Ratio error (ppm) with compensation *disabled*.

(b) Ratio error (ppm) with compensation *enabled*.
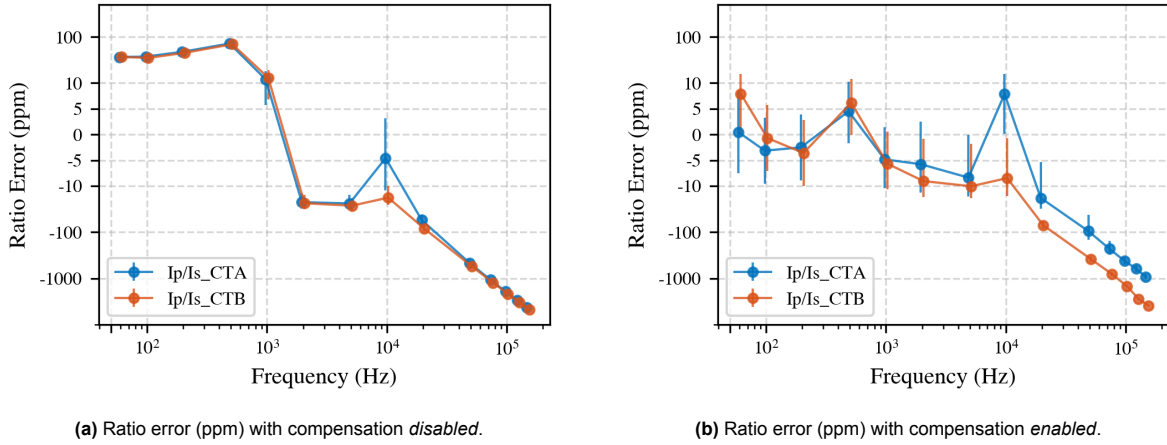
Figure 8.10: Primary-to-secondary ratio error of CTA and CTB, compensation off (left) vs. on (right). With compensation disabled, both CTs exhibit a systematic $\approx$50 ppm ratio difference below 1 kHz. Enabling compensation restores the low-frequency ratio to within measurement uncertainty, but diverging amplifier bandwidths possibly cause the two CTs to deviate beyond 20 kHz.

Disabling compensation increased low-frequency ratio error by roughly 50 ppm for both CTs, confirming the efficacy of the feedback network at 50 Hz. Above 20 kHz, however, CTA benefits from a wider-band amplifier, whereas CTB shows negligible improvement. When the electronics are disabled, the CTs behave almost identically. Future designs could explore specially designed high-bandwidth compensation to further flatten the CT response into the supraharmonic range.

8.5. Primary-Conductor Positioning

NMIs and calibration laboratories spend effort centring the primary conductor within a CT. The working theory is that, if the conductor is significantly off-axis, the magnetic field lines inside the core become non-uniform, potentially driving one sector of the core closer to saturation while another remains less magnetized.

8.5.1. Theoretical Considerations

A primary current I_p produces a magneto-motive force:

$$F_p = N_p I_p$$

Where N_p is the primary turns ratio, in our case N_p = 1. The idealised core field strength is:

$$H_p = F_p/\ell_m$$

Where ℓ_m is the mean magnetic path length. In a CT, the induced secondary current:

$$I_s \approx -(N_p/N_s)I_p$$

(neglecting magnetising current), forcing the net **B** toward zero everywhere in the core, even for a slightly eccentric conductor. In practice, however, any residual voltage on the secondary winding causes a finite magnetising current, and the local $B-H$ trajectory will follow the non-linear curve of Figure 8.11. When a portion of the core intercepts a higher flux density due to conductor eccentricity, that sector may enter the knee region earlier, distorting the ratio at large currents or with elevated secondary burdens.
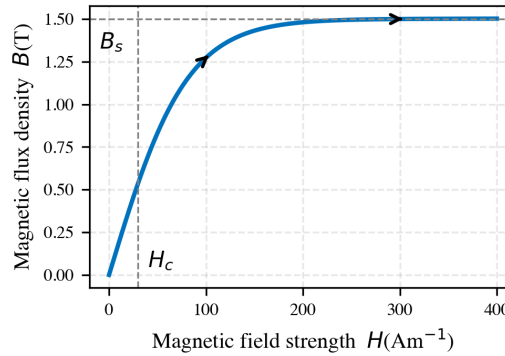
Figure 8.11: Typical **B**–**H** curve for grain-oriented silicon steel. Below the coercive field H_c the relationship is quasi-linear; near the knee the incremental permeability falls sharply, and beyond B_s the core saturates.

At high frequencies potentially an additional mechanism appears: the eccentric primary conductor forms an asymmetric capacitance to the secondary winding. The resulting displacement current introduces an internal common-mode voltage that is not fully cancelled by the CT feedback network—an effect sometimes termed electrostatic coupling imbalance. Certain high accuracy CTs therefore bond the secondary terminals with a short, equipotential strap to equalize this capacitance.

8.5.2. Experimental Evaluation

A piece of magnetically and electrically neutral plastic is used as a centring fixture (Figure 8.12) inserted between the bus-bar and the CT aperture. Two configurations were compared:

1. **Centred**: bus-bar concentric;
2. **Eccentric**: bus-bar placed at the bottom of the CT aperture.
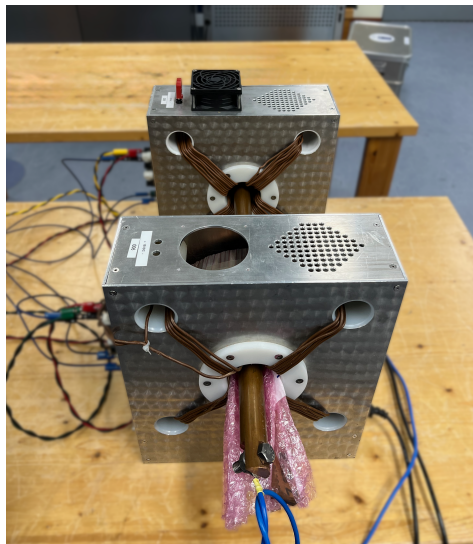
Figure 8.12: Laboratory arrangement for the positioning study. The non-magnetic fixture holds the bus-bar in the middle of the CT core (centred configuration). For the eccentric test the spacer is removed from CTA and the conductor is placed against the bottom of the aperture wall.

To assess the influence of primary conductor positioning on CT performance, the secondary-to-secondary current ratio between CT A and CT B was measured for both centred and eccentric bus-bar placements. As shown in Figure 8.13, no statistically significant difference was observed between the two configurations over the entire frequency range up to 150 kHz. All measured deviations remained within the stated measurement uncertainty, even at the highest investigated frequency.
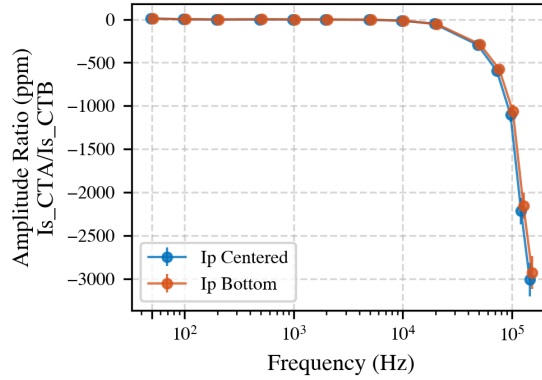
Figure 8.13: Secondary-to-secondary current ratio error between CTA and CTB for centred (bus-bar concentric) and eccentric (bus-bar against the aperture wall) scenarios. Results demonstrate no statistically significant influence of conductor centring within the measurement uncertainty up to 150 kHz.

These findings indicate that, for the current levels (<10 A) and burden values (110 mΩ) employed in this study—where secondary voltages remained well below 0.5 V—the mechanical centring of the primary conductor does not measurably affect the accuracy of secondary-to-secondary CT ratio measurements. In other words, sub-millimetre alignment of the bus-bar within the CT aperture is not required to achieve part-per-million (ppm) accuracy under typical medium-voltage CT calibration conditions.

In addition to the mechanical positioning effects, capacitive coupling between the primary conductor and the secondary windings can also introduce errors, particularly at high frequencies. As described in [68], the voltage-induced leakage current in a shielded high-voltage cable can be modelled as $I_{leak} = \omega C V$, where C is the capacitance, V the voltage between conductor and shield, and ω the angular frequency. This mechanism results in a voltage-dependent complex ratio error in the current transformer, given by:

$$\varepsilon(V) = \omega C \frac{V}{I_p} \sin \varphi \qquad (8.6)$$

where φ is the phase angle between the current and the leakage path.

Although the present experiments maintain low secondary voltages, it is important to note that at higher frequencies, even small capacitances can couple displacement currents. This effect may introduce additional ratio errors via capacitive coupling between the primary conductor and the CT secondary winding. However, under the measurement conditions used in this study, with low applied voltages and moderate current levels, no measurable impact was detected. Nonetheless, this phenomenon should be carefully considered in high-voltage or high-frequency calibration environments, where elevated voltages and higher capacitances could result in non-negligible ratio errors.

Implications for Calibration Practice

For practical calibration work, these results greatly simplify the mechanical requirements of industrial and laboratory set-ups. Standard mechanical fixtures that position the primary conductor within a few millimetres of the aperture centre are sufficient to ensure high-accuracy calibration, provided that secondary voltage remains low and no large voltage gradients are present. This reduces complexity and setup time while maintaining traceable accuracy for CTs in medium-voltage applications.

8.6. Mutual Proximity of Two CTs

When two CTs share the same primary conductor during comparison, mutual inductance and stray capacitive coupling between their cores and compensation circuits could, in principle, affect the measured ratio. The transformers used in this study incorporate a grounded metal shield, which should suppress external flux linkage; nonetheless, an experimental check was performed. However, this effect cannot be isolated to a single CT. As a result, it is necessary to assess the impact using a primary-to-secondary ratio measurement, which is inherently less sensitive to investigate effects than the secondary-to-secondary method.

Figure 8.14 compares the primary-to-secondary ratio of CTA for both geometries. The maximum deviation is just within uncertainty across the full 50 Hz–150 kHz band.
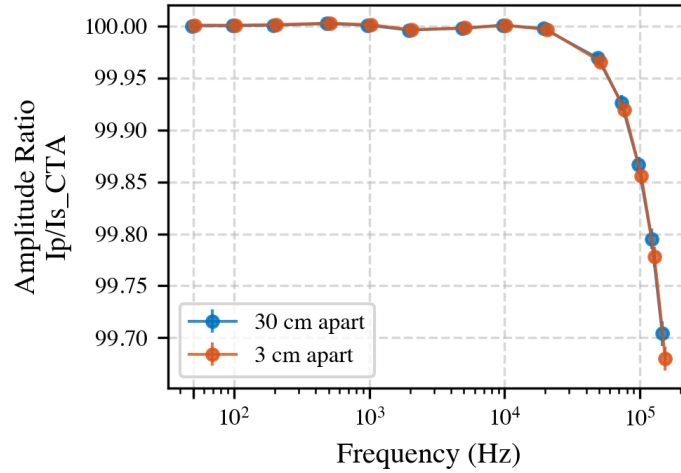
Figure 8.14: Influence of CT proximity on ratio error for CT A. In the baseline scenario the CTs are spaced 30 cm apart, in the alternative scenario the CTs are spaced 3 cm apart. At higher frequencies there appears to be some coupling between the CTs, which affects the ratio between them. At lower frequencies, no systematic trend with spacing is observed, confirming the efficacy of the grounded shield in suppressing mutual coupling.

In conclusion, the observed effects of mutual proximity between current transformers are strongly dependent on the specific CT design. The CTs employed in this study feature an engineered grounded shield, which to some extent suppresses external coupling and minimizes proximity effects. However, many commercial or customer-supplied DUT CTs may lack such shielding, making them more susceptible to errors from mutual inductance and stray capacitance when placed in close proximity during calibration. This consideration is particularly important when evaluating or calibrating client CTs, as unshielded designs could exhibit more pronounced proximity-induced errors. However, spacing them apart further, increases the possibility of capacitive leakage currents from the primary conductor to ground, which makes the measured currents between the CTs not identical. A balance should thus be reached between spacing the CTs far apart, possibly having them not measuring the same primary current, and placing them next to each other, likely introducing capacitive coupling between the CTs.

For all measurements in this work, a spacing of 30 cm between CTs was maintained, which proved adequate for the shielded models tested. Nevertheless, for CTs without dedicated shielding, or in cases where even higher accuracy is required, greater separation is recommended. Future work should further investigate the influence of proximity effects on these and other CTs, or investigate introducing an equipotential plate between the CTs.

Part IV
Interpretation and Conclusions

9
Uncertainty

A comprehensive uncertainty budget was constructed following the principles and practices outlined in the Guide to the Expression of Uncertainty in Measurement (GUM) [51]. The objective is to quantify the total measurement uncertainty associated with CT ratio error evaluation using both the secondary-to-secondary and the primary-to-secondary methods. These budgets in essence summarize the results of previous analysis sections, providing an overview of all relevant uncertainty contributions across the frequency range of interest.

Table 9.1 summarizes the expanded uncertainty (k = 2) contributions for the *secondary-to-secondary* current comparison approach, in which the device under test CT is directly compared to a reference CT. It should be emphasized that the uncertainty figures reported here do *not* include the uncertainty of the reference CT's own calibration, as the creation and traceable characterization of a broadband reference CT remains ongoing work. This method leads to a lower uncertainty compared to the primary-to-secondary measurement, as many of the sources of uncertainty drop out when comparing two secondary currents, especially when using the interchanging technique.

Table 9.1: Uncertainty budget for the *secondary-to-secondary* current CT-ratio measurement system. All entries are expanded uncertainties (k = 2) in ppm.

Source of uncertainty	50 Hz	10 kHz	150 kHz
Shunt temperature drift (Subsec 7.1)	0.5	0.5	1.0
Measurement noise (Subsec 7.2)	3.0	3.3	10.8
Intra-day repeatability (Subsec 7.3)	3.1	3.4	96
Grounding/interference (Subsec 8.2)	4.0	≈5	≈10
Instrument quantization (Subsubsec 8.3)[1]	3.8	3.8	3.8
Combined expanded uncertainty U; (k = 2)	7.0	7.9	97

Table 9.2 details the uncertainty budget for the *primary-to-secondary* current comparison method, which can be adapted for the absolute calibration of a reference CT. Here, the secondary current is compared to a direct measurement of the primary current using the ammeter's internal shunt. This method inherently introduces additional sources of uncertainty, such as shunt gain calibration and quantization.

Table 9.2: Uncertainty budget for the *primary-to-secondary* CT-ratio measurement system. All entries are expanded uncertainties (k = 2) in ppm.

Source of uncertainty	50 Hz	10 kHz	150 kHz
Combined expanded uncertainty (secondary-to-secondary method)	7.0	7.9	97
Instrument quantization (Subsubsec 8.3)	1.9	1.9	1.9
Different shunt temperature drift	2.0	2.0	10.0
Instrument calibration (gain)	5.0	5.0	50.0
Combined expanded uncertainty U; (k = 2)	9.0	9.7	110

47

At low frequencies (50 Hz), the secondary-to-secondary method achieves a combined expanded uncertainty of 7.0 ppm. The same method maintains sub-10 ppm uncertainty up to 10 kHz. At the upper frequency limit (150 kHz), uncertainty increases, to 97 ppm, which in part can be attributed to the larger intra-day repeatability, which is presumed to be related to the ratio difference between the CTs [2].

For the primary-to-secondary method, which becomes necessary for reference CT calibration or when no suitable reference CT exists, the combined expanded uncertainty increases: from 7.5 ppm at 50 Hz to approximately 110 ppm at 150 kHz. The larger uncertainty at high frequencies is mainly driven by shunt mismatches and instrument calibration.

It is important to emphasize that in both cases, the expanded uncertainty remains below the observed CT ratio error deviations (e.g., up to 3000 ppm at 150 kHz for the DUT CT), providing ample sensitivity to detect and quantify high-frequency CT performance limitations. The uncertainty analysis presented here validates the suitability of the measurement setup for both high-accuracy relative measurements (secondary-to-secondary) and possibly primary-to-secondary calibrations.

---

[2] The source of why intra-day repeatability gets worse with increasing frequency has not been investigated. However it is known that at higher frequencies, temperature, capacitances, cable positioning and more, play a bigger role, leading to increased uncertainty in the measurement.

10

Discussion and Conclusion

This thesis has presented the development and evaluation of a streamlined calibration methodology for current transformers suitable for applications up to 150 kHz. The approach replaces the more traditional, complex calibration setups with a system based primarily on a high-accuracy digital sampling ammeter (power analyser) for direct ratio measurement of CT secondary currents. This simplification not only reduces system complexity and setup time but also enables a wider measurement bandwidth than previously attainable with established methods.

The implemented calibration system achieved an expanded measurement uncertainty (k = 2) of approximately 10 ppm for frequencies up to 10 kHz. This represents an improvement over the 50 ppm uncertainty previously reported with the same equipment. For frequencies above 10 kHz and extending to 150 kHz, the measurement uncertainty remained below 120 ppm.

Throughout the course of this research, several key operational parameters and configuration choices were investigated for their impact on both accuracy and repeatability. Notably, it was determined that the digital sampling ammeter requires a warm-up period of at least 30 minutes to ensure thermal stability. This step is essential to limit temperature-induced gain drift, with measurements indicating that such drift can be contained to within 1 ppm following warm-up. Additionally, the chosen measurement protocol, a data acquisition duration of 10 seconds per frequency point, was found to keep the contribution of random sampling uncertainty below 5 ppm up to 20 kHz. To further ensure stability and reproducibility, a daily reference measurement is advised, enabling correction for any slow drift or temporal changes in laboratory conditions. While this daily reference approach is not strictly necessary for every application, it provides a practical safeguard in environments where high accuracy is required.

The effect of grounding arrangements was also systematically examined. Establishing a single-point ground at the power analyser, and grounding the CT secondary circuits, was found to produce a measurable change of approximately 4 ppm at frequencies up to 100 Hz. No significant differences were observed at higher frequencies, suggesting that earth-loop effects are primarily a concern at power frequency. Nevertheless, proper grounding was adopted as a standard procedure for all subsequent experiments to maximize repeatability and minimize susceptibility to common-mode noise. Future research could focus on further dissecting the causes of observed earth-loop currents. For example, by measuring earth currents at various secondary current levels or temporarily disconnecting internal compensation amplifiers to isolate their influence.

The selection of the shunt resistor value for measuring secondary current is another consideration. In this study, a value of approximately 110 mΩ was employed. While this resistance is relatively high for CT calibration (as it increases the CT's voltage burden and associated magnetization losses), it was chosen as a compromise between minimizing power loss and achieving manageable averaging times for uncertainty. Considering that the impedance of typical secondary-side cabling can approach 1 Ω at 150 kHz for just a meter of twisted pair, the selected value remains practical. Although the electronically compensated CTs evaluated here demonstrated negligible sensitivity to cable type, it should be recognized that other CT designs, particularly conventional iron-core types, may exhibit

greater sensitivity to cable geometry, length, and material. Future work could investigate alternative cabling solutions, such as short lengths of Litz wire, to further reduce high-frequency impedance and maintain calibration integrity.

The physical arrangement of the measurement setup, including the positioning of the primary conductor, was also evaluated. Within the range of configurations tested, no significant influence on measurement results was detected. However, capacitive coupling between the primary and secondary circuits, especially at elevated voltages and frequencies, remains a potentially important effect that warrants further investigation in future studies, particularly as CTs are generally connected to a voltage bearing primary.

The influence of mutual proximity between current transformers was also examined, with respect to the shielding and potential coupling effects. The CTs used in this study were engineered with dedicated grounded shields, which, according to the experimental results, were probably effective in suppressing mutual capacitive coupling. It is however difficult to quantify this effectively, as the secondary-to-secondary measurement technique does not work in these circumstances. When the CTs were spaced as closely as 3 cm, deviations within the measurement uncertainty were observed, primarily at the highest frequencies tested. For all measurements, a spacing of 30 cm was maintained.

However, it is important to note that these findings are highly dependent on the CT design. Many commercial or customer-supplied CTs may lack such external shielding, making them more sensitive to proximity-induced errors. In unshielded CTs, close placement could lead to measurement bias due to coupling. Conversely, spacing CTs too far apart increases the risk of capacitive leakage currents from the primary conductor to ground, which can introduce errors due to the CTs no longer sensing identical primary currents. Therefore, a balance must be struck between reducing mutual coupling and maintaining accurate primary currents between CTs. Additionally, the use of equipotential plates or further shielding could be explored in future work to reduce proximity effects. These considerations should be addressed when calibrating or evaluating DUT CTs, as the effect could be beyond the levels observed using the CTs used in this work.

A methodological contribution of this thesis lies in the development and implementation of an improved signal parameter estimation algorithm. In this work, an interpolated DFT technique, was adopted and compared to common alternative approaches. This algorithm, as presented in Chapter 5, allows for improved accuracy estimation of frequency, amplitude, and phase even when the test signal frequency does not coincide with a discrete FFT bin, as compared to 'just' selecting the highest bin in the frequency spectrum. All algorithmic steps and processing windows were benchmarked and validated for this application, including comparison with conventional FFT methods, and the computationally intensive, resampling algorithms. A comparison was conducted, both in simulation and with experimental data, to evaluate the performance of various signal analysis approaches. The application of this algorithm to broadband CT calibrations represents a contribution, offering an alternative, practical method to further simplify and validate existing measurement methods.

In summary, the results of this thesis demonstrate that modern digitally assisted techniques, combined with thoughtful consideration of practical implementation details, can enable high-accuracy CT calibration at frequencies up to 150 kHz. This work provides a foundation for future expansion of traceable CT calibration services, and highlights several avenues for further research, including detailed studies on grounding, cabling, and high-frequency effects in both measurement and real-world application contexts.

References

[1] European Commission, *Renewable energy targets*. [Online]. Available: `https://energy.ec.europa.eu/topics/renewable-energy/renewable-energy-directive-targets-and-rules/renewable-energy-targets_en#`.

[2] European Commission, *Share of energy consumption from renewable sources in Europe*. [Online]. Available: `https://www.eea.europa.eu/en/analysis/indicators/share-of-energy-consumption-from`.

[3] Eurostat, *Share of Energy from Renewable Sources Statistics*, 2024. [Online]. Available: `https://ec.europa.eu/eurostat/databrowser/view/nrg_ind_ren/default/table?lang=en`.

[4] S. Rönnberg and M. Bollen, "Power quality issues in the electric power system of the future," *Electricity Journal*, vol. 29, no. 10, pp. 49–61, Dec. 2016, ISSN: 10406190. DOI: `10.1016/j.tej.2016.11.006`.

[5] S. Bhattacharyya and S. Cobbe, "Consequences of Poor Power Quality – An Overview," in *Power Quality*, InTech, Apr. 2011. DOI: `10.5772/13787`.

[6] *Electricity balance sheet; supply and consumption*, 2024.

[7] "Power from solar panels increased slightly in 2023," CBS, Tech. Rep., 2024. [Online]. Available: `https://www.cbs.nl/en-gb/news/2024/25/power-from-solar-panels-increased-slightly-in-2023`.

[8] Rijksdienst voor Ondernemend Nederland, "Elektrisch vervoer - Personenauto's," 2024. [Online]. Available: `https://duurzamemobiliteit.databank.nl/mosaic/nl-nl/elektrisch-vervoer/personenauto-s`.

[9] Algemene Nederlandsche Wielrijders Bond, *Hier staan de laadpalen Overzicht van alle oplaadpunten voor EV's in Nederland en de rest van Europa*, 2024. [Online]. Available: `https://www.anwb.nl/auto/elektrisch-rijden/opladen/laadpaal-zoeken`.

[10] Rijksdienst voor Ondernemend Nederland, *Stand van zaken elektrisch vervoer en laadpunten*, 2025. [Online]. Available: `https://www.rvo.nl/onderwerpen/elektrisch-vervoer/stand-van-zaken`.

[11] SMPS, *SINE WAVE INVERTERS*. [Online]. Available: `https://solar.smps.us/sinewave-inverters.html`.

[12] A. Novitskiy, S. Schlegel, and D. Westermann, "Measurements and analysis of supraharmonic influences in a mv/lv network containing renewable energy sources," in *2019 Electric Power Quality and Supply Reliability Conference (PQ) & 2019 Symposium on Electrical Engineering and Mechatronics (SEEM)*, 2019, pp. 1–6. DOI: `10.1109/PQ.2019.8818260`.

[13] M. Klerx, J. Morren, and J. G. Slootweg, "Advanced replacement strategies for low voltage distribution grids," *IET Generation, Transmission & Distribution*, vol. 15, no. 17, pp. 2460–2472, 2021. DOI: `10.1049/gtd2.12190`. [Online]. Available: `https://doi.org/10.1049/gtd2.12190`.

[14] A. van Deursen, P. Wouters, and F. Steennis, "Corrosion in low-voltage distribution networks and perspectives for online condition monitoring," *IEEE Transactions on Power Delivery*, vol. 34, no. 4, pp. 1423–1431, 2019. DOI: `10.1109/TPWRD.2019.2903730`. [Online]. Available: `https://doi.org/10.1109/TPWRD.2019.2903730`.

[15] TenneT TSO B.V., *Living near high-voltage installations*, Corporate brochure, 2012. [Online]. Available: `https://netztransparenz.tennet.eu/fileadmin/user_upload/Company/Publications/Corporate_Brochures/Living_near_High-Voltage_Installations.pdf` (visited on 06/16/2025).

[16] S. Sudha Letha, A. E. Delgado, S. K. Rönnberg, and M. H. J. Bollen, "Evaluation of medium voltage network for propagation of supraharmonics resonance," *Energies*, vol. 14, no. 4, 2021, ISSN: 1996-1073. DOI: `10.3390/en14041093`. [Online]. Available: `https://www.mdpi.com/1996-1073/14/4/1093`.

[17] A. Novitskiy and D. Westermann, "Time series data analysis of measurements of supraharmonic distortion in lv and mv networks," in *2017 52nd International Universities Power Engineering Conference (UPEC)*, 2017, pp. 1–6. DOI: `10.1109/UPEC.2017.8231921`.

[18] J. Yaghoobi, F. Zare, T. Rehman, and H. Rathnayake, "Analysis of high frequency harmonics in distribution networks: 9 – 150 khz," in *2019 IEEE International Conference on Industrial Technology (ICIT)*, 2019, pp. 1229–1234. DOI: `10.1109/ICIT.2019.8755071`.

[19] M. Ghassemi, "Accelerated insulation aging due to fast, repetitive voltages: A review identifying challenges and future research needs," *IEEE Transactions on Dielectrics and Electrical Insulation*, vol. 26, no. 5, pp. 1558–1568, 2019. DOI: `10.1109/TDEI.2019.008176`.

[20] A. Mariscotti and A. Mingotti, "The effects of supraharmonic distortion in mv and lv ac grids," *Sensors*, vol. 24, no. 8, p. 2465, 2024. DOI: `10.3390/s24082465`.

[21] Á. Espin-Delgado, S. Ronnberg, S. S. Letha, and M. Bollen, "Diagnosis of supraharmonics-related problems based on the effects on electrical equipment," *Electric Power Systems Research*, vol. 195, p. 107 179, 2021, Article 107179. DOI: `10.1016/j.epsr.2021.107179`.

[22] J. Yaghoobi, A. Alduraibi, D. Martin, F. Zare, D. Eghbal, and R. Memisevic, "Impact of high-frequency harmonics (0–9 khz) generated by grid-connected inverters on distribution transformers," *International Journal of Electrical Power & Energy Systems*, vol. 122, p. 106 177, 2020, Article 106177. DOI: `10.1016/j.ijepes.2020.106177`.

[23] T. Streubel, C. Kattmann, A. Eisenmann, and K. Rudion, "Characterization of supraharmonic emission from three different electric vehicle charging infrastructures in time and frequency domain," *Energies*, vol. 15, no. 2, p. 394, 2022. DOI: `10.3390/en15020394`.

[24] *IT4PQ - About Project*. [Online]. Available: `https://www.it4pq.eu/about-project/`.

[25] *ADMIT Project Website*. [Online]. Available: `https://www.admit-project.eu`.

[26] "IEEE 519-2022 Standard for Harmonic Control in Electric Power Systems," *IEEE*,

[27] *Iec 61000-4-30: Electromagnetic compatibility (emc)-part 4–30: Testing and measurement techniques-power quality measurement methods*, IEC Standard, Geneva, Switzerland: International Electrotechnical Commission, 2015.

[28] "International Conference on Renewable Energies and Power Quality," European Association for the Development of Renewable Energy, Environment and Power Quality, Tech. Rep., 2025. [Online]. Available: `https://www.icrepq.com/`.

[29] *2020 Conference on Precision Electromagnetic Measurements (CPEM)*. IEEE, 2020, ISBN: 9781728158983.

[30] Y. Chen, E. Mohns, A. Mingotti, *et al.*, "Reference measurement systems for the calibration of instrument transformers under power quality phenomena and their uncertainties," in *2023 IEEE 13th International Workshop on Applied Measurements for Power Systems (AMPS)*, 2023, pp. 01–06. DOI: `10.1109/AMPS59207.2023.10297162`.

[31] H. E. van den Brom, G. Rietveld, and E. So, "Sampling current ratio measurement system for calibration of current transducers up to 10 ka with $5 \cdot 10^{-6}$ uncertainty," *IEEE Transactions on Instrumentation and Measurement*, vol. 64, no. 6, pp. 1685–1691, 2015. DOI: `10.1109/TIM.2015.2395571`.

[32] F. Munoz, S. Madhar, H. Van Den Brom, E. Houtzager, and G. Rietveld, "Calibration of Wideband Current Transformers using a Precision Power Analyzer as Comparator," in *CPEM Digest (Conference on Precision Electromagnetic Measurements)*, Institute of Electrical and Electronics Engineers Inc., 2024, ISBN: 9798350361049. DOI: `10.1109/CPEM61406.2024.10646121`.

[33] *Iec 61869-2:2012 instrument transformers – part 2: Additional requirements for current transformers*, IEC Standard, Geneva, Switzerland: International Electrotechnical Commission, 2012.

[34] M. H. Bollen, *What is power quality?* Jul. 2003. DOI: `10.1016/S0378-7796(03)00067-1`.

[35] "Std1159: Recommended Practice for Monitoring Electric Power Quality," IEEE, Tech. Rep., 2019.

[36] A. Mariscotti and A. Mingotti, "The Effects of Supraharmonic Distortion in MV and LV AC Grids," *Sensors*, vol. 24, Apr. 2024, ISSN: 14248220. DOI: 10.3390/s24082465.

[37] A. E. Emanuel, *Power Definitions and the Physical Mechanism of Power Flow*. Wiley, Aug. 2010, ISBN: 9780470660744. DOI: 10.1002/9780470667149.

[38] M. Agazar, G. D'Avanzo, G. Frigo, *et al.*, *Power Grids and Instrument Transformers up to 150 kHz: A Review of Literature and Standards*, Jul. 2024. DOI: 10.3390/s24134148.

[39] T. Thomas and P. A. Michael, "A review of high frequency emission in 2-150 kHz range," *International Journal of Advances in Applied Sciences*, vol. 9, no. 2, pp. 132–141, Jun. 2020, ISSN: 27222594. DOI: 10.11591/ijaas.v9.i2.pp132-141.

[40] M. Klatt, F. Kaiser, C. Lakenbrink, C. Gassner, J. Meyer, and P. Schegner, "Measurement and simulation of superharmonics resonances in public low voltage networks," Tech. Rep., 2019, pp. 3–6.

[41] S. Rönnberg, M. Bollen, H. Amaris, *et al.*, "On waveform distortion in the frequency range of 2 khz–150 khz—review and research challenges," *Electric Power Systems Research*, vol. 150, pp. 1–10, Sep. 2017. DOI: 10.1016/j.epsr.2017.04.032.

[42] International Electrotechnical Commission, "IEC 61869-1: Instrument transformers - Part 1: General requirements.," IEC, Tech. Rep., 2023.

[43] International Electrotechnical Commission, "IEC 61869-2: Instrument transformers - Part 2: Additional requirements for current transformers," IEC, Tech. Rep., 2012.

[44] International Electrotechnical Commission, "IEC 61869-3: Instrument transformers - Part 3: Additional requirements for inductive voltage transformers.," Tech. Rep., 2011.

[45] Elg commonswiki, *110 kV Current Transformer*. [Online]. Available: https://commons.wikimedia.org/w/index.php?curid=129695.

[46] R. Minkner and J. Schmid, "The Technology of Instrument Transformers Current and Voltage Measurement and Insulation Systems," Tech. Rep.

[47] R. W. Erickson and D. Maksimović, *Transformer and Inductor Design Handbook*, R. W. Erickson and D. Maksimović, Eds. New York: Marcel Dekker, Inc., 2004, ch. 16, Chapter 16: Current Transformer Design, includes simplified equivalent circuit with magnetizing branch and leakage reactance.

[48] G. Crotti, D. Giordano, G. D'Avanzo, P. S. Letizia, and M. Luiso, "A New Industry-Oriented Technique for the Wideband Characterization of Voltage Transformers," *Measurement: Journal of the International Measurement Confederation*, vol. 182, Sep. 2021, ISSN: 02632241. DOI: 10.1016/j.measurement.2021.109674.

[49] "Grant Agreement number 19NRM05 Project short name IT4PQ Project full title Measurement methods and test procedures for assessing accuracy of Instrument Transformers for Power Quality Measurements," Tech. Rep. [Online]. Available: www.IT4PQ.eu.

[50] CIPM MRA, "Reconnaissance mutuelle des étalons nationaux de mesure et des certificats d'étalonnage et de mesurage émis par les laboratoires nationaux de métrologie Mutual recognition of national measurement standards and of calibration and measurement certificates issued by national metrology institutes Comité international des poids et mesures Bureau Organisation international intergouvernementale des poids de la Convention et mesures du Mètre," Tech. Rep., 1999. [Online]. Available: http://www.bipm.org.

[51] BIPM, IEC, IFCC, *et al.*, *Evaluation of measurement data — An introduction to the "Guide to the expression of uncertainty in measurement" and related documents*, Joint Committee for Guides in Metrology, JCGM 104:2009. [Online]. Available: https://www.bipm.org/documents/20126/2071204/JCGM%5C_104%5C_2009.pdf/19e0a96c-6cf3-a056-4634-4465c576e513.

[52] A. Staff, *Traceability in Metrology: Ensuring Accuracy and Consistency*.

[53] H. Brom, G. Rietveld, and E. So, "Sampling current ratio measurement system for calibration of current transducers up to 10 ka with 510^{-6} uncertainty," *IEEE Transactions on Instrumentation and Measurement*, vol. 64, pp. 1–1, Jun. 2015. DOI: 10.1109/TIM.2015.2395571.

[54] J. D. Ramboz and O. Petersons, "A calibration service for current transformers," National Institute of Standards and Technology, Tech. Rep. Special Publication 250-36, 1991.

[55] G. Crotti, A. Delle Femine, D. Gallo, *et al.*, "Calibration of current transformers in distorted conditions," in *Journal of Physics: Conference Series*, vol. 1065, 2018, p. 052 033. DOI: 10.1088/1742-6596/1065/5/052033.

[56] V. Tarasso, V. N. Zachovalová, M. Garcocz, *et al.*, "A survey of current shunts for ac power measurements," in *CPEM 2010*, 2010, pp. 231–232. DOI: 10.1109/CPEM.2010.5545092.

[57] M. Ouameur, F. Ziade, and Y. Le Bihan, "Novel broadband calibration method of current shunts based on vna," *IEEE Transactions on Instrumentation and Measurement*, vol. PP, pp. 1–10, Jul. 2018. DOI: 10.1109/TIM.2018.2855499.

[58] G. Heine, M. Garcocz, and W. Waldmann, "International comparison of ac /dc current transfer standards. *EURAMET.EM-K12* — final report. appendix 2: "euramet.em-k12: Reports of the institutes"," Federal Office of Metrology and Surveying (BEV), Austria, Technical Report EURAMET.EM-K12, Appendix 2, Jun. 2017, Part of the EURAMET key comparison of AC–DC current transfer standards.

[59] W. F. Praeg, "Precision coaxial manganin shunts.," *IEEE Trans. Nucl. Sci.*, vol. 18, L. C. Teng, Ed., pp. 375–376, 1971. DOI: 10.1109/TNS.1971.4326064.

[60] G. Bosco, M. Garcocz, K. Lind, *et al.*, "Phase comparison of high-current shunts up to 100 khz," *Instrumentation and Measurement, IEEE Transactions on*, vol. 60, pp. 2359–2365, Aug. 2011. DOI: 10.1109/TIM.2011.2108553.

[61] H. E. Van den Brom *et al.*, "Digital–sampling based instrument-transformer comparator for power-quality applications," *IEEE Transactions on Instrumentation and Measurement*, 2023, early access. DOI: 10.1109/TIM.2023.3275401.

[62] M. Agazar, G. Crotti, H. E. Van den Brom, *et al.*, "Towards a traceable calibration of medium voltage transformers up to 150 khz," in *EPJ Web of Conferences*, vol. 323, 2025, p. 12 007. DOI: 10.1051/epjconf/202532312007.

[63] A. Collin, A. Delle Femine, D. Gallo, R. Langella, and M. Luiso, "Compensation of current transformers' nonlinearities by tensor linearization," *IEEE Trans. Instrum. Meas.*, vol. 68, pp. 3841–3849, 2019.

[64] E. So and D. Bennett, "Compact wideband high-current (≫ 1000 a) multistage current transformers for precise measurements of current harmonics," *Instrumentation and Measurement, IEEE Transactions on*, vol. 56, pp. 584–587, May 2007. DOI: 10.1109/TIM.2007.890802.

[65] Danisense, *Flux-Gate*. [Online]. Available: https://danisense.com/flux-gate/.

[66] K. Duda, *Interpolation Algorithms of DFT for Parameters Estimation of Sinusoidal and Damped Sinusoidal Signals*. [Online]. Available: www.intechopen.com.

[67] R. Lapuh, *Sampling with 3458A*. 2018. [Online]. Available: www.leftright.eu.

[68] H. E. van den Brom, R. van Leeuwen, G. Rietveld, and E. Houtzager, "Voltage dependence of the reference system in medium- and high-voltage current transformer calibrations," *IEEE Transactions on Instrumentation and Measurement*, vol. 70, pp. 1–8, 2021. DOI: 10.1109/TIM.2021.3066167.

[69] W. G. Kürten Ihlenfeld and M. Seckelmann, "SIMPLE ALGORITHM FOR SAMPLING SYNCHRONIZATION OF ADCs," Tech. Rep.

[70] M. J. Lighthill, *An Introduction to Fourier Analysis and Generalised Functions*. Cambridge University Press, Jan. 1958. DOI: 10.1017/cbo9781139171427.

Part V
Appendices

<div style="text-align: right; font-size: 3em;">A</div>

Power Analyser Characterization

A.1. Introduction

In this chapter, the YOKOGAWA WT5000 is characterized in terms of its amplitude and phase accuracy across its measurement channels over a range of frequencies. The YOKOGAWA WT5000 serves as the primary power analyser (PA) in this research and is equipped with seven measurement slots, each containing an interchangeable power measurement module. Two versions of these modules are used:

- Model 760902, rated for 5 A.
- Model 760901, rated for 30 A.

A.1.1. Power Measurement Cassettes

Each measurement slot in the WT5000 can accept one of these two types of interchangeable cassettes. These cassettes include the necessary conditioning circuits, shunt resistors, and anti-aliasing filters (optional) that feed into the internal Analogue to Digital Converter (ADC) of the WT5000. When installed in the analyser, each cassette communicates the measured voltage and current signals to the main system. This modularity allows the PA to handle a wide range of input currents (from milliamperes to tens of amperes, depending on the cassette specification) and voltages (up to several hundred volts).

This chapter focuses on the relative accuracy of these modules when measuring amplitude and phase. Although each slot and cassette is designed to meet the high-accuracy specification, slight deviations exist, particularly at higher frequencies or due to small mechanical and component tolerances. The following sections describe the experiments performed to quantify these deviations and discuss their implications for precise power and phase-angle measurements.

A.2. Methodology

To characterize the current transformers (CTs) used in the setup, the amplitude ratio between two channels is measured, along with the relative phase shift. For instance, if a CTs input registers 2 V and its output registers 1 V, the CT can be said to have a transformation ratio of 2:1. Because it is hard to accurately control the input, definitely for our final goal of

$$\geq 1\,\text{kA}$$

, It is therefore for our experiment most important that the ratio measurements remain consistent across the measurement channels. If they are consistent, a known calibrated reference can be used, to characterize the object under test.

Additionally, the phase shift introduced by each CT is of interest. To evaluate both amplitude and phase characteristics, a function generator provides a sinusoidal signal at a specified frequency to *all* measurement slots of the power analyser. Under ideal conditions, every slot would measure identical amplitude and phase. However, small deviations (ideally 0) typically arise:

- **Magnitude ratio error**, expressed in parts per million (ppm).
- **Phase difference**, expressed in microradians (μrad).

Rather than relying on a simple time-domain ratio (which can be influenced by noise and harmonics), the signals are analysed in the frequency domain. A 0.4 s tumbling window computes the complex representation of the measured signal at each channel. From this complex vector, both the magnitude and phase are extracted. The ratio between the magnitudes and the difference between the phases of different channels can then be computed to quantify the deviations introduced by the measurement system.

A.3. Experimental Characterization of Relative Phase Accuracy
A.4. Channel-to-Channel Effect

When a single-frequency sinusoidal signal of 50 Hz (3 V peak-to-peak) is fed into each channel, the power analyser exhibits slight variations in both amplitude ratio and phase among the channels. Table A.1 summarizes the mean and standard deviation of the ratio and phase difference for three channels (U2, U3, and U4), using U1 as the reference. Each statistic is calculated over 25 samples, and a 95% confidence interval (assuming normal distribution) is provided.

Table A.1: Comparison of Ratio and Phase Measurements at 50 Hz. U1 Used as Reference for Channels U2, U3, and U4

Channel	Parameter	Mean	Std	95% CI (k=2)
U2/U1	Ratio (ppm)	58	5	[56.0, 60.0]
	Phase (µrad)	-2	7	[–4.8, 0.8]
U3/U1	Ratio (ppm)	40	6	[37.6, 42.4]
	Phase (µrad)	5	6	[2.6, 7.4]
U4/U1	Ratio (ppm)	-157	7	[–159.8, –154.2]
	Phase (µrad)	-1	5	[–3.0, 1.0]

Figure A.1 illustrates the amplitude ratios and phase differences over time. In Fig. A.1a, the ratios are close to unity (expressed as near 0 ppm deviation), but small deviations are evident. Meanwhile, Fig. A.1b shows that phase differences are also small but non-zero.

(a) Amplitude Ratio over Time

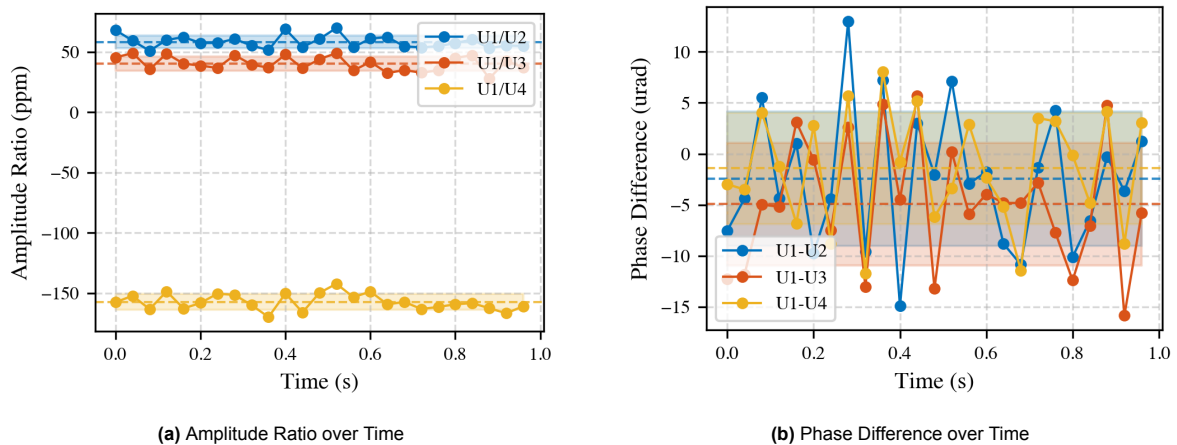**(b)** Phase Difference over Time

Figure A.1: Amplitude Ratio and Phase Difference in Time for a Single-Tone Signal at 50 Hz. U1 is used as the reference channel.

A.5. Frequency Effect

The next step is to characterize how these measurement deviations (i.e., ratio and phase errors) vary with frequency. The experiment was repeated at selected harmonics and multiples of the nominal 50 Hz

fundamental frequency:

50, 100, 200, 500, 1 kHz, 2 kHz, 5 kHz, 10 kHz, 20 kHz, 50 kHz, 75 kHz, 100 kHz, and 150 kHz.

At each frequency, the average ratio and phase difference for each channel were recorded. These measurements allow us to observe how the channel-to-channel imperfections evolve with frequency. Figure A.2 shows the results of these tests.
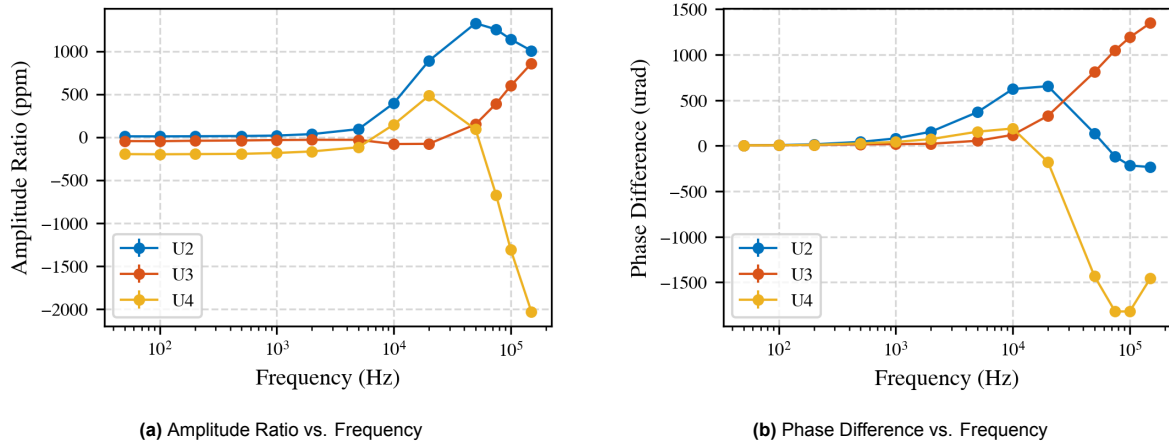

(a) Amplitude Ratio vs. Frequency

(b) Phase Difference vs. Frequency

Figure A.2: Amplitude Ratio and Phase Difference as a Function of Frequency, for Harmonics of 50 Hz. U1 Serves as the Reference Channel. From this it can be Observed that Amplitude Ratio and Phase Difference Error Increase with Frequency.

Phase Differences as Time Delays

Another way to interpret phase difference is by converting it from radians into an equivalent time delay. For a signal of frequency f, a phase difference $\Delta\phi$ (in radians) corresponds to a time shift Δt given by

$$\Delta t = \frac{\Delta\phi}{2\pi f}. \tag{A.1}$$

Figure A.3 shows an example of phase errors translated into time delays. It can be observed that the phase difference in seconds, does not increase at the same rate as the frequency increase.
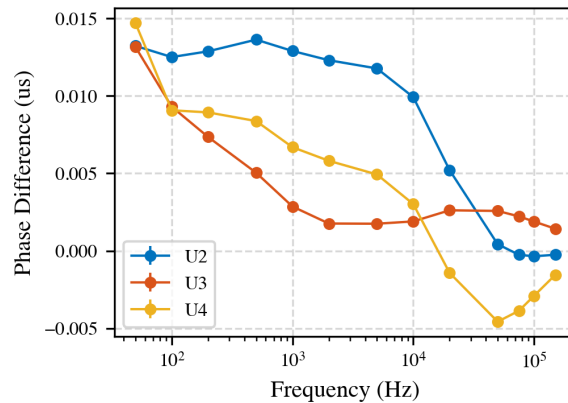
Figure A.3: Phase Differences Expressed as Time Delays (μs) Versus Frequency for Harmonics of 50 Hz. U1 is the reference channel. Higher frequencies reduce the equivalent time delay for the same angular offset.

A.6. Grid Harmonic Effect

The laboratory environment in which the measurements are taken includes typical power grid cables crossing the room. These cables can emit magnetic and electric fields at (or near) the 50 Hz fundamen-

tal of the grid supply, which may introduce small induced voltages or currents in the equipment under test, thereby affecting the measurement accuracy.

To mitigate these effects, the power analyser (and other equipment) are powered from a 56.9 Hz supply. This has the practical benefit of shifting any stray fields inside and around the equipment away from 50 Hz. Since we are often interested in equipment behaviour at 50 Hz, this isolation improves measurement quality.

A.7. Estimating Energy at Nearby Frequencies

To verify that the influence of stray grid frequencies is negligible, an experiment was performed by injecting a 70 Hz signal from the source while examining the energy at 50 Hz, 53 Hz, and 56.9 Hz. A 60 s aperture was used, and resampling was performed to properly capture the energy distribution. Table A.2 summarizes the measured energy components at these frequencies, relative to the total energy.

Table A.2: Measured Energy at Various Frequencies During a 70 Hz Input Signal (60 s Aperture)

Frequency (Hz)	Energy	% of Total Energy
50	2000	83 ppm
53	2500	104 ppm
56.9	3500	145 ppm
70	2.4×10^7	99.95 %

From Table A.2, one can see that the unwanted frequency components (50 Hz, 53 Hz, and 56.9 Hz) are negligible, each being on the order of parts per million. Even with a long 60 s acquisition window, their levels remain close to the noise floor. The largest extraneous component is at 56.9 Hz (the power analyser's own supply frequency), but it is still small relative to the 70 Hz fundamental injection.
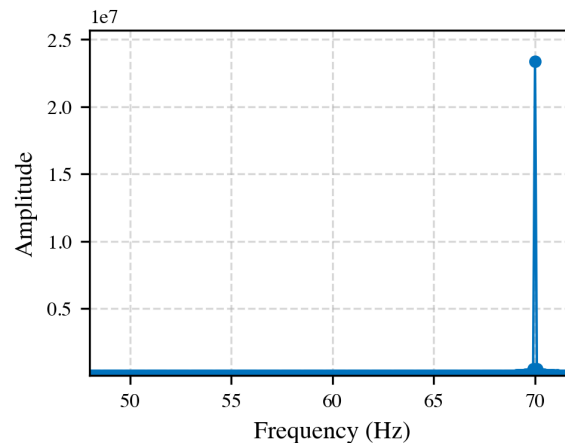

Figure A.4: Frequency Spectrum of a 70 Hz Signal Over a 60 s Acquisition Window. Very Little Energy is Present at 50 Hz, 53 Hz, or 56.9 Hz.

A.7.1. Repeating the Frequency Sweep at 53 Hz

To further confirm whether grid pollution affects the measurement accuracy, the experiment in Section A.7 was repeated using 53 Hz instead of 50 Hz. In deciding which harmonics to test at 53 Hz, two potential approaches were considered:

1. *Same harmonic orders as the 50 Hz case:* For example, the 100th harmonic at 50 Hz is 50 kHz, whereas the 100th at 53 Hz is 53 kHz. However, this yields a frequency gap of 3 kHz between the two tests, potentially complicating direct comparisons.

2. *Match the actual test frequencies as closely as possible:* For example, choose h at 53 Hz so that h $\times$ 53 Hz is as close as possible to h$'$ $\times$ 50 Hz from the original test. This reduces the gap between the two measurement sets.

The second approach was selected to minimize frequency discrepancies. Table A.3 shows the chosen harmonic orders for 53 Hz.

Table A.3: Choice of 53 Hz Harmonics to Closely Matching 50 Hz Test Frequencies

50 Hz Harmonic	50 Hz Frequency	Closest 53 Hz Harmonic	53 Hz Frequency
1	50 Hz	h = 1	53 Hz
2	100 Hz	h = 2	106 Hz
4	200 Hz	h = 4	212 Hz
10	500 Hz	h = 9	477 Hz
20	1 kHz	h = 19	1007 Hz
40	2 kHz	h = 38	2014 Hz
100	5 kHz	h = 94	4982 Hz
200	10 kHz	h = 189	10017 Hz
400	20 kHz	h = 377	19981 Hz
1000	50 kHz	h = 943	49979 Hz
1500	75 kHz	h = 1415	74995 Hz
2000	100 kHz	h = 1887	100011 Hz
3000	150 kHz	h = 2830	149990 Hz

Figure A.5 shows an example comparison of amplitude ratio measurements at selected 50 Hz and 53 Hz test frequencies. The small observed differences are within the overall uncertainty range and do not indicate significant additional error due to grid pollution at these frequencies.
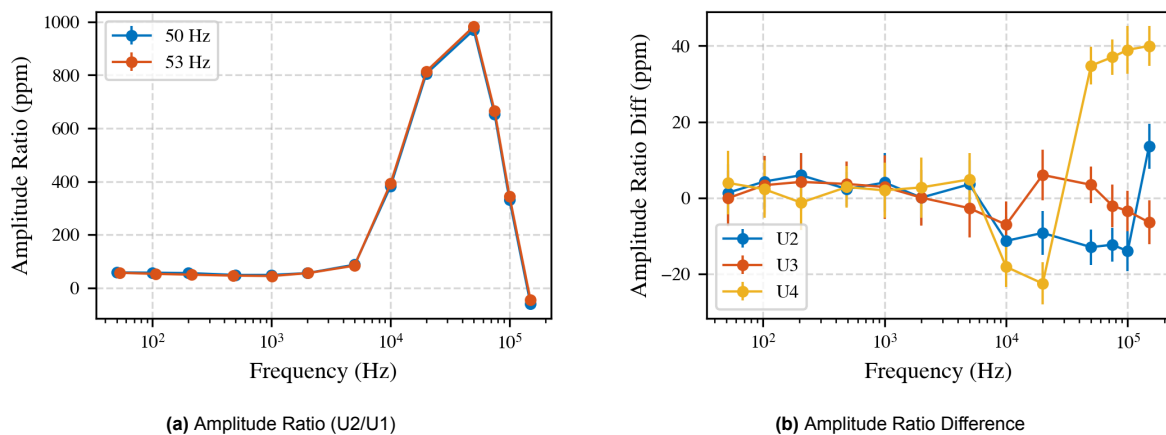

(a) Amplitude Ratio (U2/U1)

(b) Amplitude Ratio Difference

Figure A.5: Comparison of Measured Amplitude Ratio for Harmonics of 50 Hz and 53 Hz. The difference between the two sweeps is small and within random uncertainty, indicating minimal impact from stray grid frequencies.

A.8. Anti-Aliasing Filter Effect

The YOKOGAWA WT5000 includes an optional analogue anti-aliasing-filter (AA-filter), specified at approximately 1 MHz, before the Analogue to Digital Converter (ADC). This filter can be enabled or disabled depending on the measurement requirements. To assess its impact, the same harmonic sweep was performed with the AA-filter either enabled or disabled.
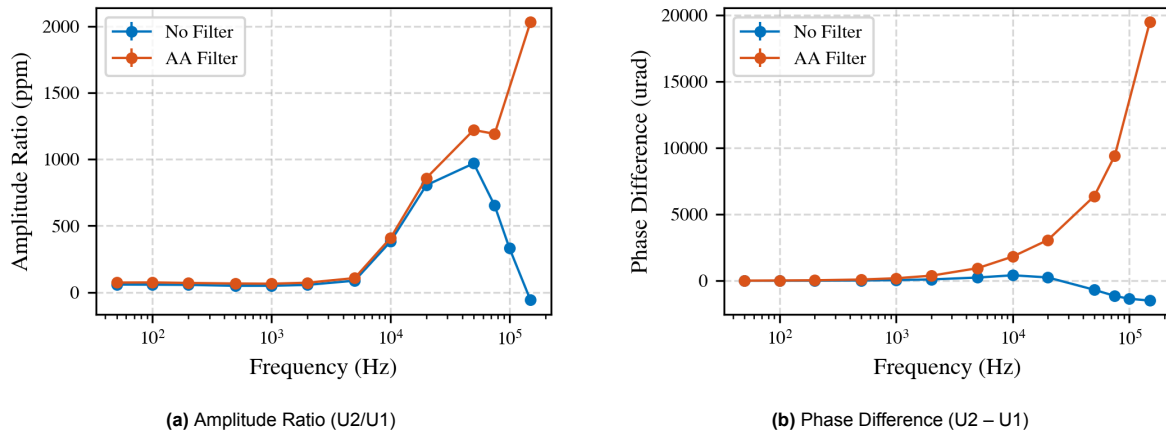
(a) Amplitude Ratio (U2/U1)

(b) Phase Difference (U2 – U1)

Figure A.6: Amplitude Ratio and Phase Difference with and without the 1 MHz Anti-Aliasing Filter Enabled. Measurements are at harmonics of 50 Hz.

Figure A.6 suggests that the AA-filter introduces slight additional deviations in amplitude ratio and phase compared to the no-filter case, particularly at higher frequencies. The analogue components within the filter (resistors, capacitors, etc.) each have manufacturing tolerances, which lead to channel-to-channel differences. Although the anti-aliasing filter may help mitigate high-frequency noise or frequency folding, disabling it might be preferable in the case where the highest possible amplitude and phase ratio consistency between channels is desired.

A.9. Time Stability Effect

Finally, the possibility of drift in the power analyser over time is investigated. If the analyser's internal components or references shift with temperature or operational time, the channel-to-channel amplitude or phase accuracy may degrade. To test this, a measurement at multiple frequencies (the same 50 Hz harmonics from Section A.5) was taken at 0 min, 30 min, and 60 min after powering on the instrument.

Figure A.7 shows the amplitude ratio (U2/U1) at these three time intervals. No significant long-term drift is observed.
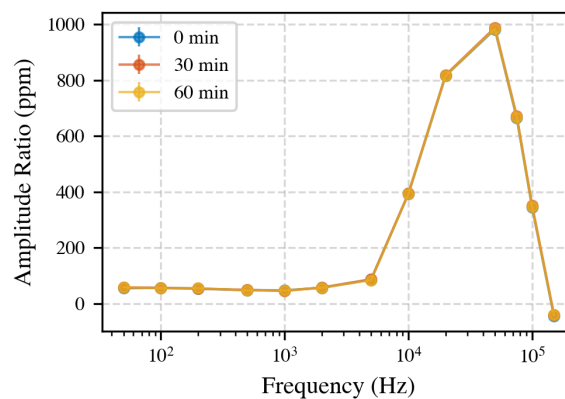
Figure A.7: Amplitude Ratio (U2/U1) as a Function of Frequency at 0 min, 30 min, and 60 min After Instrument Power-Up. Harmonics of 50 Hz are Tested.

To quantify the stability, the difference between the amplitude ratio at 0 min and at 60 min was calculated. If no drift occurred, this difference would be zero for all frequencies. Figure A.8 plots the differences in both amplitude ratio and phase difference. The largest deviations, which occur around 150 kHz, are around 13 ppm, and remain within the expanded uncertainty bounds (k = 2) of the PA.

(a) Amplitude Ratio Differences (0 min vs. 60 min)

(b) Phase Differences (0 min vs. 60 min)
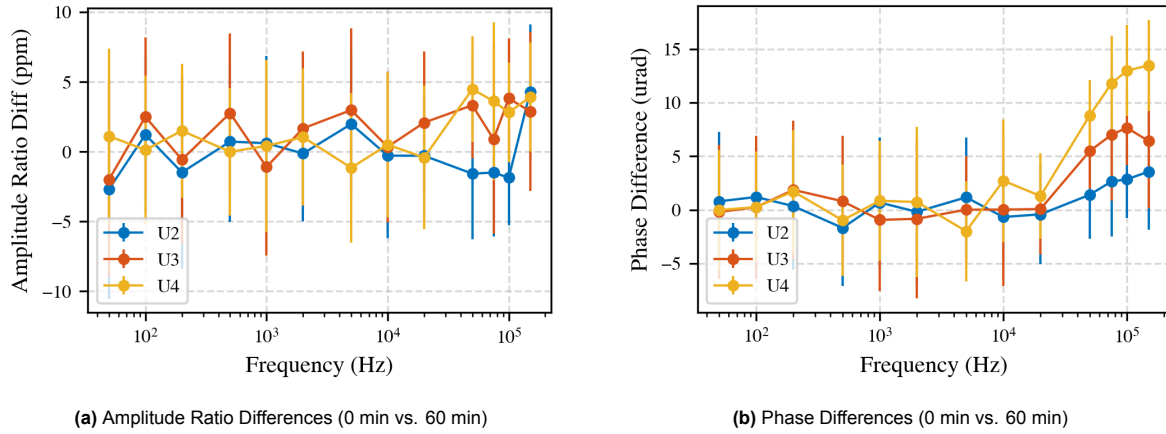
Figure A.8: Differences in Amplitude Ratio and Phase at 0 min and 60 min After Power-Up. Measurements Are at Harmonics of 50 Hz with U1 as the Reference Channel. All Differences Remain Within the Standard Deviation.

A.10. Voltage-channel calibration

A.10.1. Experimental procedure

1. A nominal 1 V_{rms} sine wave was synthesised at the 14 discrete frequencies of interest.
2. Each point consists of 10 consecutive 1 s integrations of the power analyser channel 1, averaged to obtain $U_{PA,i}$.
3. Simultaneously the same voltage was measured with a calibrated reference meter yielding $U_{ref,i}$.

For every frequency f_i

$$\Delta_i = U_{PA,i} - U_{ref,i}, \qquad \varepsilon_i = \frac{\Delta_i}{U_{ref,i}} \text{ (ppm)}, \qquad k_i = \frac{U_{ref,i}}{U_{PA,i}},$$

where k_i is the gain-correction factor to be applied to future measurements of the PA at that frequency.
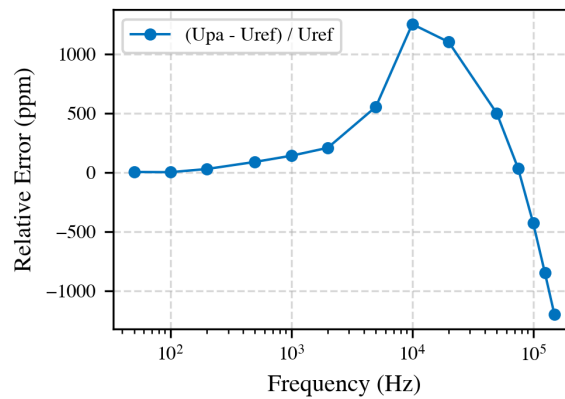
A.10.2. Results

Figure A.9: Relative gain error in ppm of the PA Channel 1 voltage module compared to a know reference at different fundamental frequencies. The peak gain

f (Hz)	U_{ref} (V)	U_{PA} (V)	ε (ppm)	k
50	1.000006	1.000010	+4	0.999996
100	1.000008	1.000010	+2	0.999998
500	1.000011	1.000100	+89	0.999911
1 000	1.000009	1.000150	+141	0.999859
5 000	1.000016	1.000570	+554	0.999446
10 000	1.000017	1.001270	+1253	0.998728
50 000	1.000190	1.000690	+500	0.999501
75 000	1.000414	1.000450	+36	0.999964
100 000	1.000717	1.000290	−427	1.000427
150 000	1.001503	1.000300	−1202	1.001203

The error curve (see Figure A.9) peaks at 1250 ppm near 10 kHz. Applying k(f) reduces the residual flatness error to $\lesssim$ 50 ppm over the entire band.

A.11. Conclusion

The results presented in this chapter indicate that the YOKOGAWA WT5000 generally maintains very low amplitude ratio and phase difference errors across a wide range of frequencies. Channel-to-channel variations are on the order of a few parts per million in amplitude and a few micro-radians in phase. Additionally, the effect of grid pollution at 50 Hz is mitigated by powering the analyser at 56.9 Hz, ensuring minimal coupling.

Enabling the anti-aliasing filter does introduce slightly larger deviations, presumably because of minor tolerances in the analogue filter components. Finally, the analyser demonstrates good time stability: after a 60-minute warm-up, any drift is within the measurement uncertainty. These characterizations provide confidence that the PA can be used in precision measurement scenarios requiring high accuracy in amplitude and phase ratios, which is important for the rest of this research.

Algorithm Implementations

B.1. Synchronization of ADC

The algorithm presented by Kurten-Ihlenfeld [69] provides a systematic approach for synchronizing an ADC to the fundamental frequency of an unknown continuous periodic signal. It relies on detecting Discrete Fourier Transform (DFT) leakage and iteratively tuning the sampling frequency. This section offers a step-by-step guide to implementing the algorithm in a practical digital signal processing setup. Experimental results are included to demonstrate its performance in both simulation and our testing environments.

B.1.1. System Setup and Requirements

Before implementing the algorithm, ensure you know the input signal characteristics:

- The bandwidth BW of the signal is known.
- The number of samples n in each analysis window is predetermined.

B.1.2. Initial Conditions for the First Sampling

1. **Set the Initial Sampling Frequency**

   - Choose f_s = 2BW (to satisfy the Nyquist condition).
   - Initiate ADC sampling at this frequency and collect n samples.

2. **Compute the DFT**

   - Perform a FFT on the n sampled points to obtain the frequency spectrum.
   - Identify the fundamental frequency f_1 as the spectral component with the highest amplitude A_1.

3. **Detect Side-Band Leakage**

   - Measure the amplitudes of the side-bands at $f_1 - \frac{f_s}{n}$ and $f_1 + \frac{f_s}{n}$, denoted as A_{1-} and A_{1+}.
   - Store the values (A_{1-}, A_1, A_{1+}) in a record vector R_1.

B.1.3. Iterative Frequency Adjustment

4. **Adjust the Sampling Frequency f_s Based on Side-Band Energy**

   - If $A_{1+} > A_{1-}$, **increase** f_s by a small step Δf_s.
   - If $A_{1+} < A_{1-}$, **decrease** f_s by Δf_s.
   - Update $f_s \leftarrow f_s + \Delta f_s$.

5. **Resample the Signal and Recompute FFT**

   - Collect or resample a new set of n samples at the updated f_s.

- Recalculate f_1, A_{1-}, A_1, and A_{1+}, and store them in a record vector R_2.

6. **Check Convergence**

- Compute the difference:

$$\Delta f_1 = f_i - f_1. \tag{B.1}$$

- If

$$\left| \Delta f_1 \right| \geq 0.5 \, \frac{f_s}{n},$$

reduce the step size (e.g., $\Delta f_s \leftarrow \Delta f_s/2$), resample, and repeat step 4.

- If

$$\left| \Delta f_1 \right| < 0.5 \, \frac{f_s}{n},$$

proceed to phase-based fine-tuning.

B.1.4. Phase-Based Fine-Tuning

7. **Split the Data Record into Two Subsets**

- Divide the n samples into two subsets of equal length:
  - **Set 1**: n_1 samples
  - **Set 2**: n_2 samples

8. **Compute the Phase Difference**

- Perform FFT on both subsets and measure the phase of the fundamental in each. Then compute:

$$\Delta \phi_1 = \phi_{n2} - \phi_{n1}. \tag{B.2}$$

9. **Compute Frequency Correction**

$$\Delta f_s = \frac{\Delta \phi_1}{2\pi} \times \frac{n_1 n_2}{n} \, f_s. \tag{B.3}$$

10. **Loop Until Convergence**

$$\frac{\Delta f_s}{f_s} < \xi, \tag{B.4}$$

where ξ is a precision threshold (in our case, 10^{-9}).

B.1.5. Handling Special Cases

A. Dealing with Interharmonics

- Increase n to improve FFT resolution.
- Introduce randomized variations in f_s and re-run the algorithm.

B. Handling Noise and Unstable Signals

- Apply digital filtering before performing the FFT.
- Employ adaptive filtering techniques for more robust frequency detection.
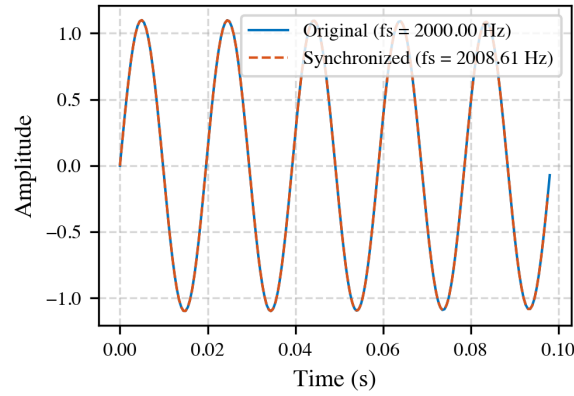
B.1.6. Experimental Validation

Figure B.1: Time domain comparison of the original and synchronized sine.

(a) Frequency Domain Comparison
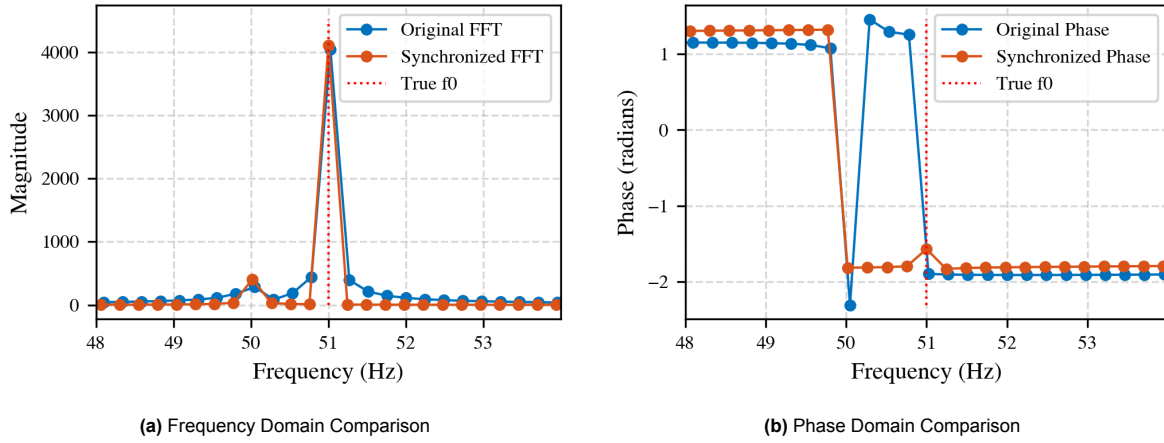
(b) Phase Domain Comparison

Figure B.2: Comparison of the original and synchronized sine signals, showing reduced spectral leakage after applying the algorithm.

The algorithm was tested using both simulation and real-world experiments:

- A 500 Hz bandwidth signal with an unknown 51 Hz fundamental was successfully synchronized.
- In the presence of 50 Hz power-line interference, the algorithm estimated the frequency with an error of $\sim 2 \times 10^{-8}$ in relative terms.
- The phase deviation caused by interference was found to be about -10.6 μrad.

These results indicate that the algorithm achieves sub-ppm accuracy, making it suitable for applications requiring precise ADC synchronization.

B.1.7. Applicability of the Synchronization Algorithm

The algorithm redistributes the signal's energy in the frequency domain, thereby minimizing side-lobes and focusing energy at the fundamental frequency. In practical scenarios, this could reduce sampling artifacts and yield more repeatable measurements. For instance, by aligning frequency bins using a 0.2 s window, the signal amplitude becomes more stable. Figure B.3 shows that, after synchronization, the signal's energy is more tightly concentrated around the fundamental peak.
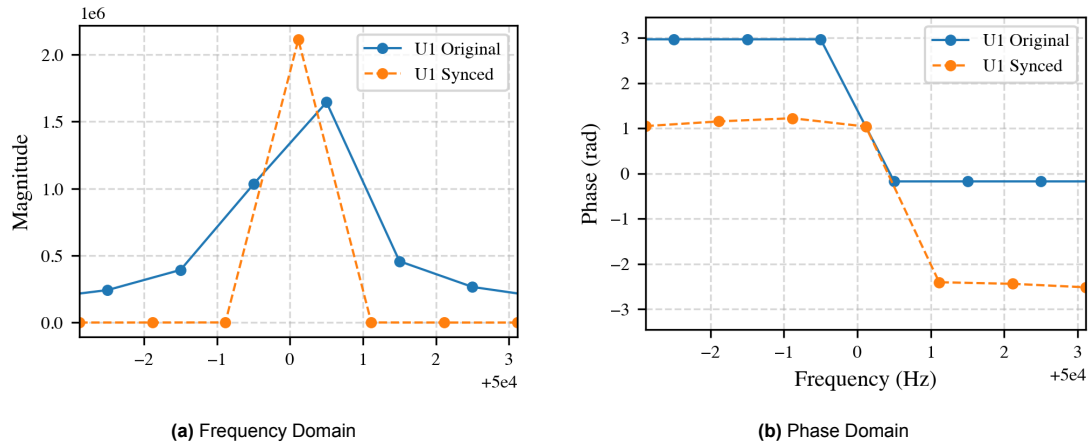
(a) Frequency Domain   (b) Phase Domain

Figure B.3: Frequency magnitude (top) and phase (bottom) domain comparison before and after resampling.

Resampling to include an integer number of cycles (see Figure B.4) reduces discontinuities at window boundaries, mitigating leakage in the FFT analysis.
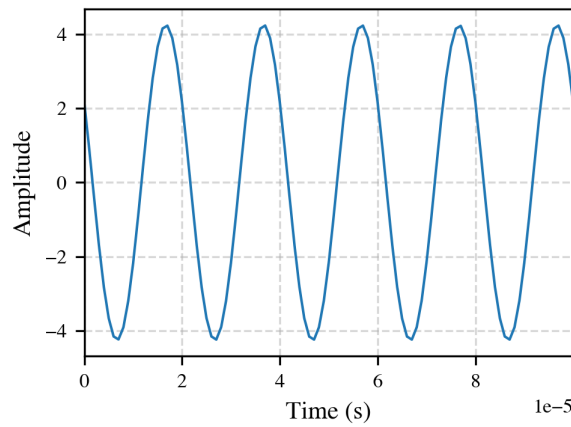

Figure B.4: Time-domain resampled signal at 50 000 Hz.

When a rolling 0.2 s window is employed to compute the ratio between two channels, the standard deviation of that ratio decreases following synchronization. Figures B.5a and B.5b show the amplitude ratio before and after resampling, and Figures B.6a and B.6b compare phase differences under the same conditions.
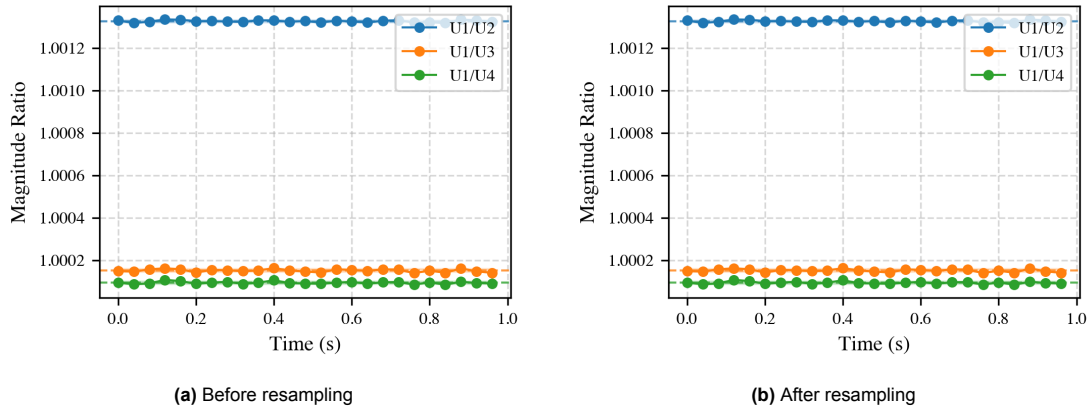
(a) Before resampling   **(b)** After resampling

Figure B.5: Comparison of the magnitude ratio between two channels at 53 Hz.

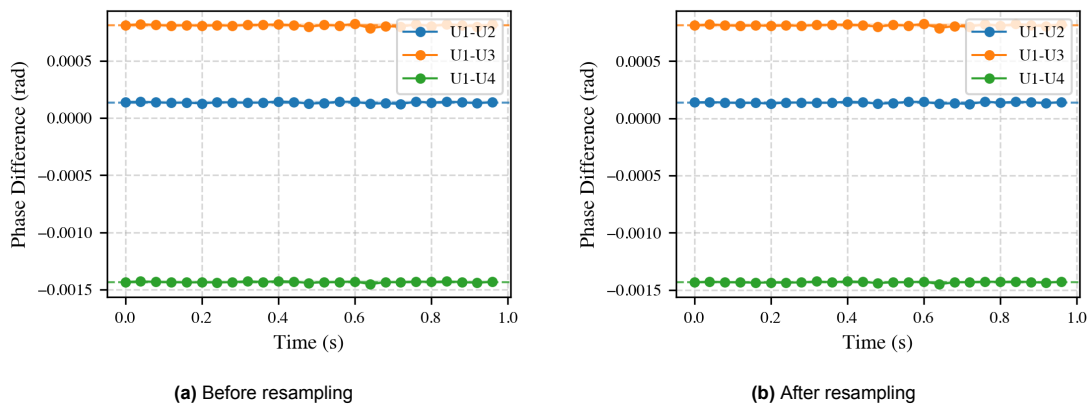**(a)** Before resampling   **(b)** After resampling

Figure B.6: Comparison of the phase difference between two channels at 53 Hz.

Table B.1: Comparison of magnitude (ratio) and phase difference between original and resampled data sets.

Parameter	Original Data	Resampled Data
Reference frequency	50 000.500 Hz	50 000.114 Hz
Mean phase difference (μrad)	136	138
Phase difference std. (μrad)	7	6
Mean ratio	1.001327	1.001327
Ratio std.	0.000005	0.000005

Across Frequencies

To assess whether resampling meaningfully improves channel-to-channel consistency over a wide range of input frequencies, we applied the same sinusoidal signal (at varying frequencies) to all four ADC inputs (U1–U4). Figures B.7a and B.7b show the measured amplitude ratios and phase differences, respectively, as functions of frequency when U1 serves as a reference channel. The amplitude ratios lie very close to unity (within 10^{-3} of one another) for all tested frequencies from about 50 Hz to 150 kHz. Meanwhile, the measured phase differences remain below a milliradian in magnitude.
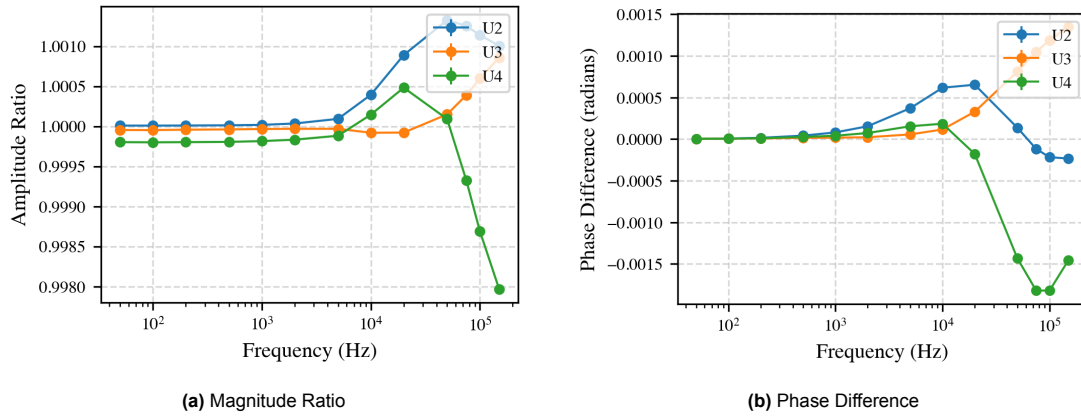
(a) Magnitude Ratio   (b) Phase Difference

Figure B.7: Frequency sweep (U1 as reference) results after resampling.

To isolate the effect of resampling, we additionally plotted the difference between the original and re-sampled data in Figures B.8a and B.8b. These "difference" plots confirm that the resampling procedure shifts the amplitude ratios and phase differences by only a few parts in 10^{-5} or less. Even at higher frequencies, where small numerical or interpolation effects might be more pronounced, the deviation introduced by resampling remains negligible. This implies that, for signals spanning 100 Hz to 100 kHz, resampling has little impact on the final amplitude or phase measurements.
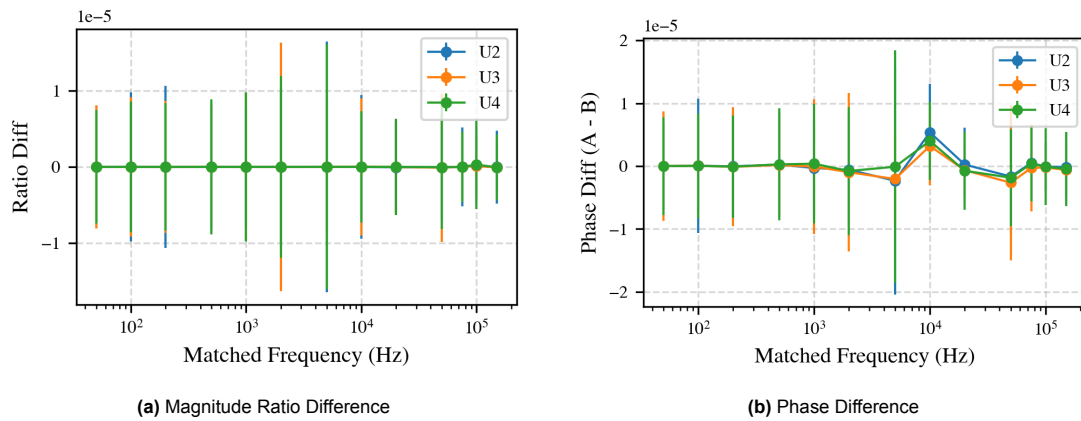

(a) Magnitude Ratio Difference   (b) Phase Difference

Figure B.8: Comparison of original vs. resampled data (difference plots) across different frequencies.

Linear vs. Cubic Interpolation

To explore interpolation effects, a 50 000 Hz sine wave of length 1 s was sampled at 1 MHz. This data set was then resampled via linear and cubic (spline) interpolation for four channels, each routine repeated ten times. The average execution times and standard deviations are as follows:

- **Linear Interpolation:**
  - Mean run time: 71.11 s
  - Standard deviation: 0.38 s
- **Cubic (Spline) Interpolation:**
  - Mean run time: 64.98 s
  - Standard deviation: 0.34 s

Although cubic interpolation is inherently more computationally intensive per loop, it converges in fewer steps (two) than linear interpolation (three), resulting in a slightly shorter overall runtime. Figures B.9a and B.9b compare the execution-time distributions for both methods.
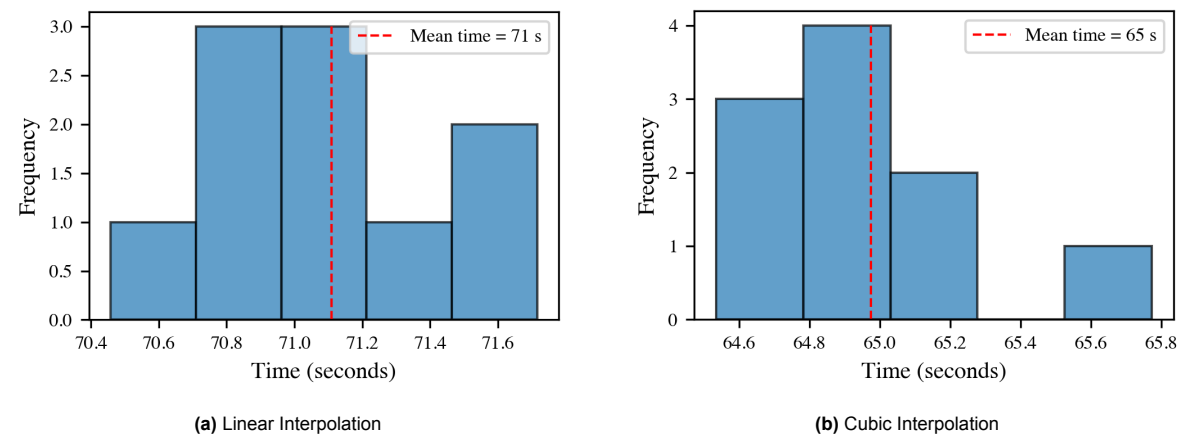
(a) Linear Interpolation

(b) Cubic Interpolation

Figure B.9: Execution times (10 runs) for linear vs. cubic interpolation.

Accuracy comparisons show negligible differences between the two interpolation techniques in both ratio and phase estimates. The mean phase difference remains at about 0.000138 rad, with a standard deviation of 0.000006 rad. Figures B.10 and B.11 confirm that both methods yield virtually identical frequency and phase responses.
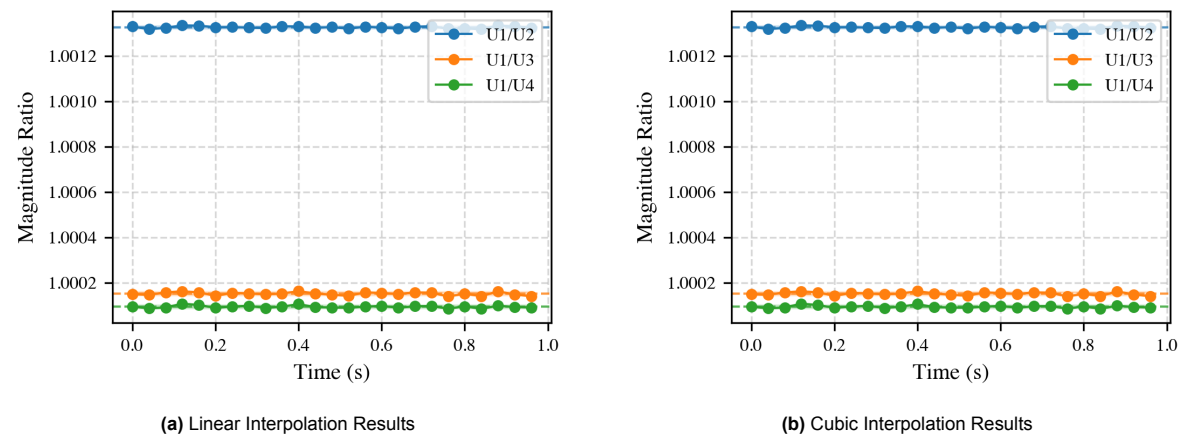

(a) Linear Interpolation Results

(b) Cubic Interpolation Results

Figure B.10: Magnitude ratio for linear vs. cubic interpolation.

(a) Frequency Domain of Linear Interpolation

(b) Frequency Domain of Cubic Interpolation

(c) Phase Domain of Linear Interpolation

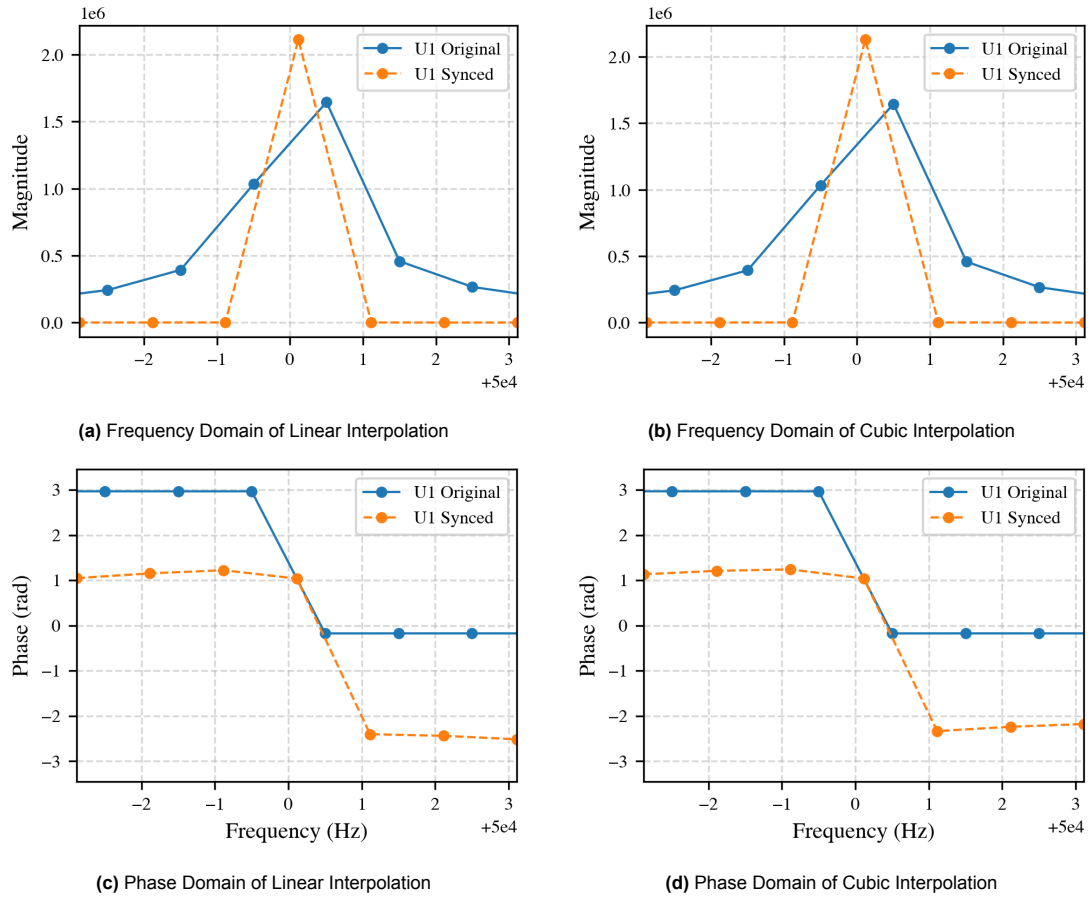(d) Phase Domain of Cubic Interpolation

Figure B.11: Frequency and phase domain comparison, showing identical outcomes between linear and cubic interpolation outcomes.

B.1.8. Conclusion

In this work, the synchronization algorithm effectively reduces side-lobe leakage and concentrates the signal's energy at the fundamental frequency. Under our test conditions (low noise, minimal high‐energy harmonics, and identical signals on all channels), resampling offered limited benefit. Because each channel saw the same frequency distribution, using channel-to-channel ratios as the main metric did not reveal significant improvements from resampling.

However, if the signals differ across channels (having different spectral distributions) resampling can shift each channel's energy more precisely into the desired frequency band. This would lead to more accurate ratio measurements. Consequently, we will continue comparing original and resampled signals in future measurements, particularly when the channel inputs are not identical.

C
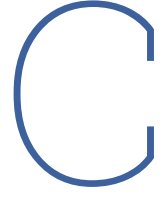
Frequency Sweep

This appendix presents the limitations of using a frequency sweep, for characterizing the behavior of a current transformers and other filters over a broad frequency range in a single experiment. The idea is to use a continuously varying sinusoidal signal (sweep) that spans the frequencies of interest, in this case from 50 Hz to 150 kHz, and then sample this signal with a sufficiently high sampling rate (e.g., 1 MHz) using a power analyzer.

C.1. Definition of a Logarithmic Frequency Sweep

A logarithmic sweep is defined by a time-dependent frequency $f(t)$ that evolves from a starting frequency f_{start} to a stopping frequency f_{stop} over a specified sweep duration T. The mathematical form of this instantaneous frequency is:

$$f(t) = f_{start} \left(\frac{f_{stop}}{f_{start}} \right)^{\frac{t}{T}} = f_{start}\, e^{at}, \quad \text{where} \quad a = \frac{\ln\left(\frac{f_{stop}}{f_{start}}\right)}{T}. \tag{C.1}$$

The instantaneous phase $\phi(t)$ is the integral of the angular frequency $2\pi f(t)$. Thus:

$$\phi(t) = 2\pi \int_0^t f(\tau)\, d\tau = 2\pi f_{start} \int_0^t e^{a\tau}\, d\tau, \tag{C.2}$$

$$= \begin{cases} 2\pi f_{start}\, \dfrac{e^{at} - 1}{a}, & \text{if } a \neq 0, \\ 2\pi f_{start}\, t, & \text{if } a = 0 \text{ (i.e., } f_{start} = f_{stop}). \end{cases} \tag{C.3}$$

The resulting logarithmically sweeping sinusoidal signal is then given by:

$$x(t) = \sin\left(\phi(t)\right). \tag{C.4}$$

Figure C.1 illustrates an example of such an ideal logarithmic sweep from 1 Hz to 100 Hz over 1 s.
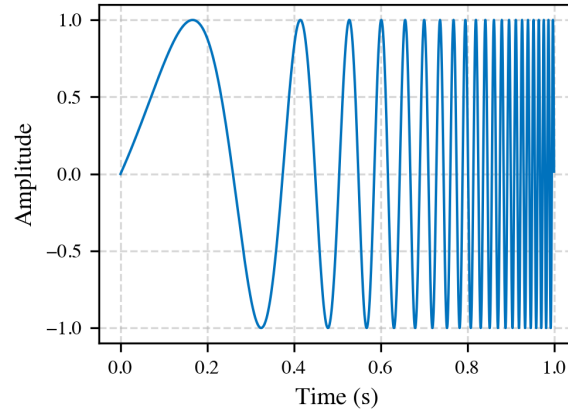
Figure C.1: Ideal waveform: Logarithmic sweep from 1 Hz to 100 Hz over 1 s.

C.2. Effect of Sampling

While a logarithmic sweep ideally provides a continuous frequency transition from f_{start} to f_{stop}, sampling can introduce distortions if the sampling frequency is not significantly larger than the highest frequency component of the signal. This effect can be analyzed following an approach similar to that presented in [70].

C.2.1. Sampling in the Time Domain

Consider the continuous-time sweep signal:

$$x(t) = \sin\big(\phi(t)\big), \quad \phi(t) = 2\pi f_{start} \cdot \frac{e^{at} - 1}{a}, \quad a = \frac{\ln\big(\frac{f_{stop}}{f_{start}}\big)}{T}.$$

When sampled with a sampling period $T_s = \frac{1}{f_s}$, the resulting discrete-time sequence is:

$$x[n] = x(nT_s) = \sin\big(\phi(nT_s)\big), \quad n \in \mathbb{Z}.$$

This can be interpreted as multiplying $x(t)$ by a Dirac comb $\triangle_{T_s}(t)$, yielding:

$$x_s(t) = x(t)\,\triangle_{T_s}(t) = x(t) \sum_{n=-\infty}^{\infty} \delta(t - nT_s).$$

C.2.2. Practical Observations and Examples

To illustrate these sampling effects, consider a simple logarithmic sweep from 1 Hz to 100 Hz over 1 s, sampled at 100 Hz (i.e., only one sample per cycle at 100 Hz near the sweep's upper limit). Figure C.2 shows the resulting time-domain and frequency-domain plots. Pronounced distortion arises because the sampling frequency is not sufficiently high relative to the maximum swept frequency.
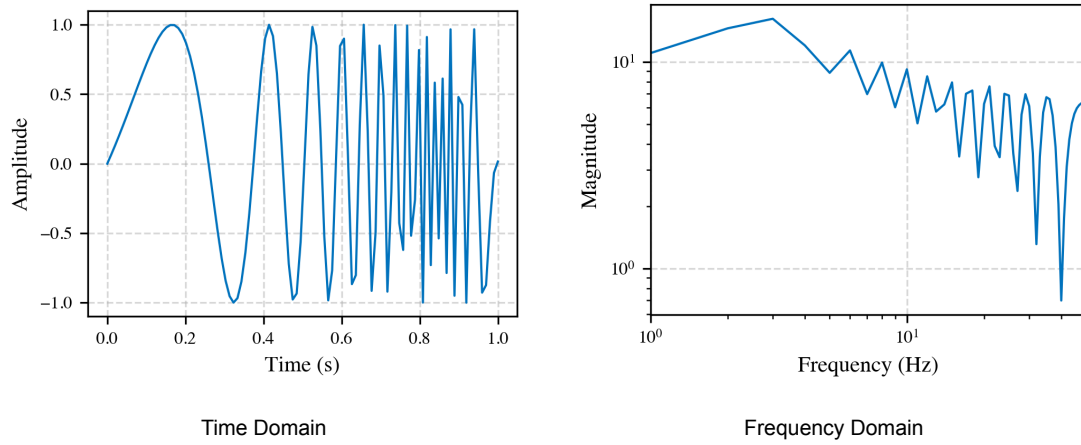
Time Domain   Frequency Domain

Figure C.2: Time-domain (left) and frequency-domain (right) representations of a logarithmic sweep from 1 Hz to 100 Hz over 1 s, sampled at 100 Hz.

Next, increasing the sweep duration (from 1 s to 10 s) while holding the sampling rate fixed at 100 Hz changes how the frequency evolves over time. Figure C.3 compares the frequency-domain representations for these two sweep durations. The 10 s sweep distributes the same frequency range over a longer time, slightly reducing the severity of sampling-induced distortion, yet it does not eliminate it entirely.

Over 1 s   Over 10 s
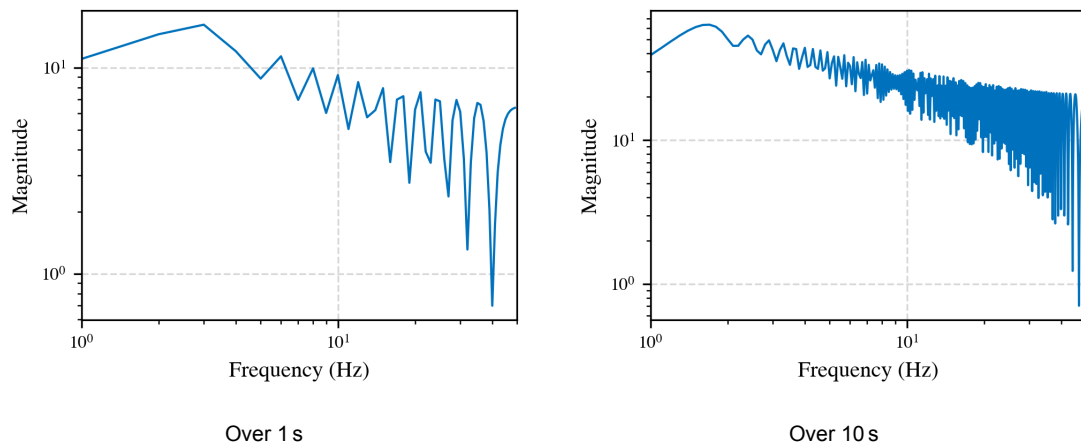
Figure C.3: Comparison of logarithmic sweeps in the frequency domain for 1 s (left) and 10 s (right) durations, each sampled at 100 Hz over a 1 Hz to 100 Hz range.

C.3. Implications for this Experiment

In the experiment of primary interest, the sweep extends from 50 Hz to 150 kHz over a 60 s period, sampled at 1 MHz. Although the higher sampling rate and longer sweep duration substantially reduce distortion compared to the earlier examples, some residual distortion remains. This becomes evident when comparing early and late portions of the sweep (Figure C.4).

First 0.1 s   Last 3 μs

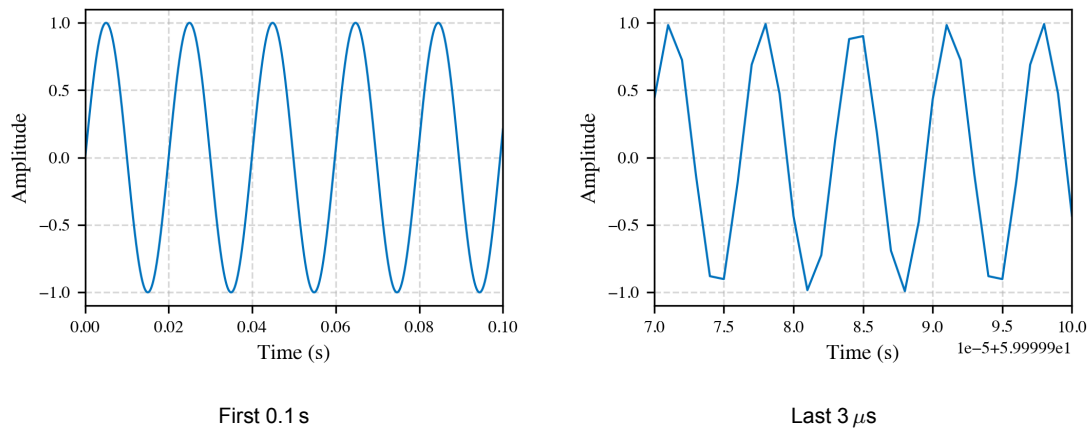**Figure C.4:** Time-domain representations of a 60 s logarithmic sweep from 50 Hz to 150 kHz, sampled at 1 MHz. Although overall distortion is low, artifacts appear.

Figure C.5 shows the corresponding frequency-domain plots. The left panel highlights the primary frequency range of interest (50 Hz to 150 kHz), while the right panel illustrates the full bandwidth up to the Nyquist frequency (500 kHz). Within the 50 Hz to 150 kHz band, the sweep amplitude is non-uniform.
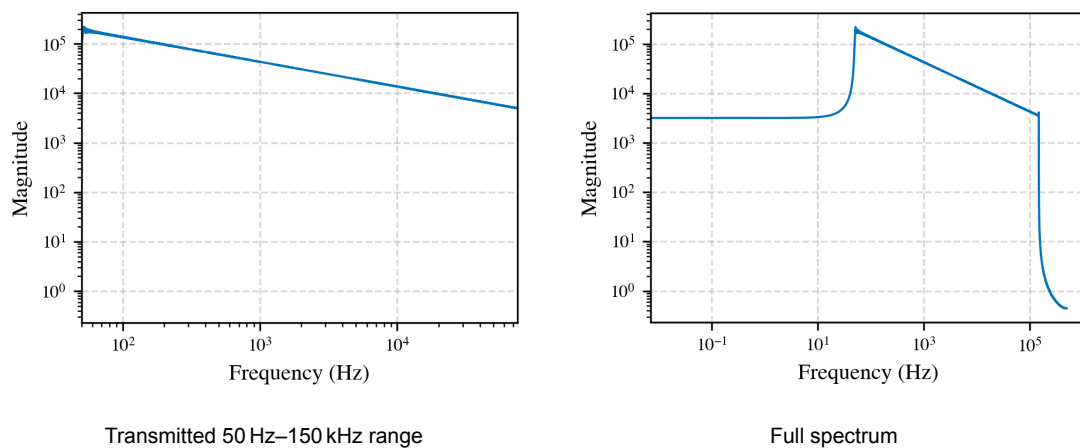

Transmitted 50 Hz–150 kHz range   Full spectrum

Figure C.5: Frequency-domain representations of the 60 s logarithmic sweep from 50 Hz to 150 kHz, sampled at 1 MHz. The left panel shows the transmitted band of interest; the right panel shows the entire spectrum up to 500 kHz. Non-constant amplitude in the transmitted band indicates residual distortion.

C.4. Conclusion

Logarithmic sweeps provide a practical way to cover a broad frequency range in a single experiment. However, the choice of sampling frequency and sweep duration significantly affects the fidelity of the measured signal. When the sweep frequency approaches a sizeable fraction of the sampling frequency, aliasing and other sampling artifacts can distort the waveform.

Therefore, it was decided to do our experiments at a discrete frequency; this would eliminate most of the sampling distortion, provide a constant phase, and allow us to average over the one recording of the same frequency.

D

Manufacturer Stated Accuracies

Table D.1: Voltage Accuracy Specifications (6-month values; 1-year = 1.5× the reading component)

Frequency Range	Accuracy Specification
DC	$\pm\left(0.02\% \text{ of reading} + 0.05\% \text{ of range}\right)$
$0.1\,\text{Hz} \leq f < 10\,\text{Hz}$	$\pm\left(0.03\% \text{ of reading} + 0.05\% \text{ of range}\right)$
$10\,\text{Hz} \leq f < 45\,\text{Hz}$	$\pm\left(0.03\% \text{ of reading} + 0.05\% \text{ of range}\right)$
$45\,\text{Hz} \leq f \leq 66\,\text{Hz}$	$\pm\left(0.01\% \text{ of reading} + 0.02\% \text{ of range}\right)$
$66\,\text{Hz} < f \leq 1\,\text{kHz}$	$\pm\left(0.03\% \text{ of reading} + 0.04\% \text{ of range}\right)$
$1\,\text{kHz} < f \leq 10\,\text{kHz}$	$\pm\left(0.1\% \text{ of reading} + 0.05\% \text{ of range}\right) + 0.015 \times f\% \text{ of reading (if 10 V range or less)}$
$10\,\text{kHz} < f \leq 50\,\text{kHz}$	$\pm\left(0.3\% \text{ of reading} + 0.1\% \text{ of range}\right)$
$50\,\text{kHz} < f \leq 100\,\text{kHz}$	$\pm\left(0.6\% \text{ of reading} + 0.2\% \text{ of range}\right)$
$100\,\text{kHz} < f \leq 500\,\text{kHz}$	$\pm\left((0.006 \times f)\% \text{ of reading} + 0.5\% \text{ of range}\right)$
$500\,\text{kHz} < f \leq 1\,\text{MHz}$	$\pm\left((0.022 \times f - 8)\% \text{ of reading} + 1\% \text{ of range}\right)$

Table D.2: Current Accuracy Specifications (6-month values; 1-year = 1.5× the reading component)

Frequency Range	Accuracy Specification
DC	$\pm\left(\text{0.02\% of reading + 0.05\% of range}\right)$
$0.1\,\text{Hz} \leq f < 10\,\text{Hz}$	$\pm\left(\text{0.03\% of reading + 0.05\% of range}\right)$
$10\,\text{Hz} \leq f < 45\,\text{Hz}$	$\pm\left(\text{0.03\% of reading + 0.05\% of range}\right)$
$45\,\text{Hz} \leq f \leq 66\,\text{Hz}$	$\pm\left(\text{0.01\% of reading + 0.02\% of range}\right)$
$66\,\text{Hz} < f \leq 1\,\text{kHz}$	$\pm\left(\text{0.03\% of reading + 0.04\% of range}\right)$
$1\,\text{kHz} < f \leq 10\,\text{kHz}$	$\pm\left(\text{0.1\% of reading + 0.05\% of range}\right)$
$10\,\text{kHz} < f \leq 50\,\text{kHz}$	$\pm\left(\text{0.3\% of reading + 0.1\% of range}\right)$
$50\,\text{kHz} < f \leq 100\,\text{kHz}$	$\pm\left(\text{0.6\% of reading + 0.2\% of range}\right)$
$100\,\text{kHz} < f \leq 200\,\text{kHz}$	$\pm\left((0.00725 \times f - 0.125)\%\text{ of reading + 0.5\% of range}\right)$
$200\,\text{kHz} < f \leq 500\,\text{kHz}$	$\pm\left((0.00725 \times f - 0.125)\%\text{ of reading + 0.5\% of range}\right)$
$500\,\text{kHz} < f \leq 1\,\text{MHz}$	$\pm\left((0.022 \times f - 8)\%\text{ of reading + 1\% of range}\right)$

Table D.3: Active Power Accuracy Specifications (Power factor 1; 6-month values; 1-year = 1.5× the reading component)

Frequency Range	Accuracy Specification
DC	$\pm\left(\text{0.02\% of reading + 0.05\% of range}\right)$
$0.1\,\text{Hz} \leq f < 10\,\text{Hz}$	$\pm\left(\text{0.08\% of reading + 0.1\% of range}\right)$
$10\,\text{Hz} \leq f < 30\,\text{Hz}$	$\pm\left(\text{0.08\% of reading + 0.1\% of range}\right)$
$30\,\text{Hz} \leq f < 45\,\text{Hz}$	$\pm\left(\text{0.05\% of reading + 0.05\% of range}\right)$
$45\,\text{Hz} \leq f \leq 66\,\text{Hz}$	$\pm\left(\text{0.01\% of reading + 0.02\% of range}\right)$
$66\,\text{Hz} < f \leq 1\,\text{kHz}$	$\pm\left(\text{0.05\% of reading + 0.05\% of range}\right)$
$1\,\text{kHz} < f \leq 10\,\text{kHz}$	$\pm\left(\text{0.15\% of reading + 0.1\% of range}\right) + 0.01 \times f\%\text{ of reading (if 10 V range or less)}$
$10\,\text{kHz} < f \leq 50\,\text{kHz}$	$\pm\left(\text{0.3\% of reading + 0.2\% of range}\right)$
$50\,\text{kHz} < f \leq 100\,\text{kHz}$	$\pm\left(\text{0.7\% of reading + 0.3\% of range}\right)$
$100\,\text{kHz} < f \leq 200\,\text{kHz}$	$\pm\left((0.008 \times f)\%\text{ of reading + 1\% of range}\right)$
$200\,\text{kHz} < f \leq 500\,\text{kHz}$	$\pm\left((0.008 \times f)\%\text{ of reading + 1\% of range}\right)$
$500\,\text{kHz} < f \leq 1\,\text{MHz}$	$\pm\left((0.048 \times f - 20)\%\text{ of reading + 1\% of range}\right)$

D.1. Corrections in Measurement Accuracy

The overall measurement accuracy is affected by several correction terms. Here we describe three such corrections:

D.1.1. Influence of Self-Generated Heat (Current Input)

Self-generated heat from the current input can cause additional measurement error. The correction terms are defined as follows:

- **For AC Input Signals:**

$$\Delta_{\text{heat, AC}} = 0.00002 \cdot I^2 \quad (\%\text{ of reading})$$

- **For DC Input Signals:**
    - *Current Correction:*

$$\Delta_{\text{heat, DC, current}} = 0.00002 \cdot I^2 \quad (\% \text{ of reading}) \ + \ 3 \cdot I^2 \quad (\mu A)$$

    - *Power Correction:*

$$\Delta_{\text{heat, DC, power}} = 0.00002 \cdot I^2 \quad (\% \text{ of reading}) \ + \ 3 \cdot I^2 \quad (\mu A) \times U$$

Here, I is the current reading in amperes and U is the voltage reading in volts. These additional error components are added to the base current or power accuracy.

D.1.2. Accuracy of Power Factor λ

The accuracy with which the power factor (denoted by λ) is measured is affected by both a scaling term and a correction based on the phase error. The relevant correction formula is:

$$\delta_\lambda = \pm \left[\left(\lambda - \frac{\lambda}{1.0002} \right) + \left| \cos\phi - \cos\left(\phi + \sin^{-1}\left(\frac{\epsilon_0}{100} \right) \right) \right| \right]$$

where

- ϕ is the phase difference between the voltage and current,
- ϵ_0 represents the influence from the power factor when $\lambda = 0$ (expressed in percent).

This formula indicates that the error in λ comprises both a fractional deviation term and a trigonometric component reflecting phase-dependent effects. The final value is specified to an accuracy of ± 1 digit.

D.1.3. Accuracy of Phase Difference ϕ

Similarly, the phase difference measurement accuracy is corrected using a combination of the previously explained terms. The representative formula is:

$$\delta_\phi = \pm \left[\left| \phi - \cos^{-1}\left(\frac{\lambda}{1.0002} \right) \right| + \sin^{-1}\left(\frac{\epsilon_0}{100} \right) \right]$$

where the same symbols apply as in the power factor correction. This expression quantifies the deviation in the measured phase difference (in degrees), again rounded to ± 1 digit.

Abstract

The increasing integration of renewable energy sources and power electronic devices is changing the electricity grid, leading to widespread harmonic and supraharmonic distortions. Accurate measurement and calibration of current transformers (CTs) up to the 150 kHz range are essential for reliable power quality assessment and grid monitoring. However, traditional calibration approaches are limited in both bandwidth and practicality, particularly for high-current and high-frequency conditions. This thesis develops and validates a broadband calibration methodology for CTs, enabling ratio and phase error characterization from 50 Hz to 150 kHz using a high-precision digital sampling ammeter (from a power analyser) as the core measurement instrument. The proposed system eliminates the need for auxiliary equipment and thus reduces component count, ultimately allowing for simplified broadband calibrations. An uncertainty budget is established with combined expanded uncertainties (k = 2) for the measurement system of less than 10 ppm up to 10 kHz, and less than 100 ppm at 150 kHz for the secondary-to-secondary comparison method. This is an improvement over the previous state of the art for this setup, which had an uncertainty of 50 ppm and a maximum frequency of 10 kHz. For primary-to-secondary calibration, uncertainties remain below 110 ppm at the highest frequency, allowing for the further development of a reference current transformer.

The thesis systematically examines the influence of critical experimental factors, such as grounding configuration, shunt selection, conductor positioning, cabling, and measurement duration, on overall calibration accuracy and repeatability. Key findings include the importance of instrument warm-up, the impact of earth-loop currents, and practical considerations for shunt and cable selection for high-frequency application. The demonstrated approach provides a metrological foundation for future implementation of wideband CT accuracy classes and supports ongoing international efforts to establish traceable measurement infrastructure for power quality applications. This work, carried out at the Dutch national metrology institute (VSL), aims to contribute to the goals of the European ADMIT project.